AN ANALYSIS OF THE DOUBLE TORSION TEST

A THESIS

Presented to

The Faculty of the Division of Graduate Studies

By

Ampere A. Tseng

In Partial Fulfillment

of the Requirements for the Degree
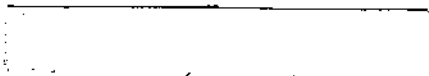
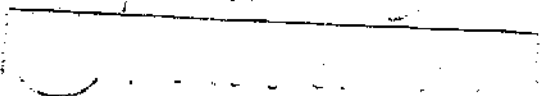Doctor of Philosophy in the School

of Mechanical Engineering

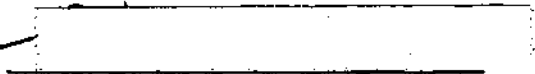Georgia Institute of Technology

September 1978

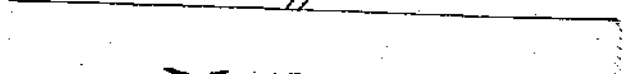# AN ANALYSIS OF THE DOUBLE TORSION TEST

Approved:

J. T. Berry, Chairman

J. M. Anderson

S. Atluri

M. Corley

C. H. Jacobs

D. Kalish

Dated approved by Chairman _1st August 1975_

This Dissertation

is dedicated to my parents

Dr. and Mrs. Chi-Kung Tseng

ACKNOWLEDGMENTS

The author wishes to express his sincere appreciation to the chairman of his thesis committee, Dr. John T. Berry, for his suggestion of the topic and for supervision throughout the entire period of this study.

Acknowledgment is also expressed to Drs. Melvin R. Corley, Jerry M. Anderson, Satyanadham N. Atluri, David Kalish and Carl H. Jacobs, for their helpful suggestions and discussions regarding this work. The author would also like to extend special thanks to Dr. S. Peter Kezios, Director of the School of Mechanical Engineering at the Georgia Institute of Technology and to Mr. Alfred Lohmeier, Project Manager of the Breeder Reactor Component Project of Westinghouse Electric Corporation, for their encouragement and financial support during the conduct of this work.

Finally the author would like to especially commend his wife, Shih-ying, for her patience and encouragement.

TABLE OF CONTENTS

LIST OF TABLES

LIST OF ILLUSTRATIONS

SUMMARY

An extensive finite element analysis has been undertaken to
verify the integrity of a many-sided fracture toughness test,
namely the double torsion test. Previous experimental work with
this test has shown that the use of relatively thin sectioned
specimens can be permitted. The section thickness is considerably
less than that associated with conventional techniques, while
the test examined also simplifies the determination of the fracture
toughness (K_{IC}). K_{IC} values, which are independent of the crack
length, have been obtained for glasses, ceramics, polymers, and
a variety of metals and alloys. The finite element analysis
involved shows that excellent correlation between the numerical
and experimental results can be obtained. The maximum stress
intensity factor is shown to be almost independent of crack length
over a considerable range. A generalized calibration equation is
provided for this test.

Since the double torsion test specimen usually contains a
curved precrack and a non-planar loading condition, an extensive
three-dimensional elastic analysis has been performed to investi-
gate the dependence of the stress intensity factors upon specimen
geometry and loading condition as well as crack size and shape.
The complicated stress distribution, side-groove effect and free
surface effect have also been included in the analysis. In order

to assure a high degree of accuracy of the results, a special wedge element embedded in the elastic crack front singularity has been developed for this elastic analysis.

To satisfy the small-scale yielding fracture criterion, the crack front plasticity was investigated through a two-dimensional equivalent model and through a J-integral evaluation. Results show that the crack size requirement of ASTM standard tests can be held for the double torsion test. However, for this test, the crack size requirement is seen to be an extremely conservative requirement as compared with the ASTM standard fracture toughness tests. In addition, the role of fracture toughness criteria and of the specimen thickness requirement, as well as of the fracture growth surface appearance have also been discussed at some length.

LIST OF SYMBOLS*

A   — Crack surface or modification factor defined in Eq. (7·3)

A_i, a_i — Constants

a, b, c, c_e — Dimensions of crack defined in Fig. 5 or Fig. 7

$\{B\}$ — Body force vector

C, C_t — Compliances

$[D]$ — Matrix relating joint displacement to strain field

$\{d\}$ — Nodal displacement vector

E   — Young's modulus

$[E]$ — Matrix of elastic constants

$\{f\}$ — Displacement vector

G   — Elastic energy release rate

H'   — The slope of stress-strain curve beyond yielding point

h   — Characteristic length of special element defined in Fig. 14

I_p — Polar moment of inertia of one half of the double torsion specimen

J   — J-integral defined in Eq. (2·11) and Appendix D

$[J]$ — Jacobian matrix

K   — Stress intensity factor

K_c — Critical stress intensity factor

---

*The symbols which are not found here are explained whevever they first appear.

K_{cal} — Stress intensity factor calculated from Eq. (3·14)

K_I, K_{II}, K_{III} — Stress intensity factors for modes I, II, and III, respectively

K_{IC} — Fracture toughness

$[K]$ — Global stiffness matrix

$[k]$ — Element stiffness matrix

L — Length of the double torsion specimen

ℓ_x, ℓ_y — Direction cosines

M — Number of element

M_t — Torque

N_i — Shape functions

$[\tilde{N}], \underline{N}$ — Matrix of shape functions

P — Load

P_c — Critical load

$\{P\}$ — Surface nodal load vector

$\{R\}$ — Global nodal load vector

r, θ, z — local cylindric coordinates

$\{r\}$ — Total equivalent nodal load vector

$\{r_b\}, \{r_p\}, \{r_t\}, \{r_\epsilon\}$ — Equivalent nodal load vectors (subscripts denote specific type)

S, S' — Surfaces

S_{ij} — Deviatoric stress components

$[SD]$ — Matrix of strain-displacement relation

$\{T\}, T_x, T_y$ — Surface traction vector and components

t, t_c — Thicknesses defined in Fig. 4 or Fig. 7

$\{U\}$ — Global nodal displacement vector

u,v,w	–	Displacement components
V,V_m	–	Volumes
W,W_o,W_m	–	Widths defined in Fig. 4 or Fig. 7
$W_b,W_c,W_e,W_p,$ W_s,W_t	–	Energy or work (subscripts denote specific type)
w_s	–	Strain energy density or element strain energy
x,y,z	–	Cartesian coordinates
α	–	the constraint factor to measure the transition from plane strain to plane stress
β	–	Numerical factor used in Eq. (6·1)
Γ	–	Any contour surrounding the crack tip
ε	–	Distance between applied loads defined in Fig. 4
ε_e	–	Effective strain
$\{\varepsilon\},\varepsilon_{ij}$	–	Strain vector and components
ξ,η,ζ	–	Isoparametric coordinates
ξ_i,η_i,ζ_i	–	Coordinates of node i in isoparametric coordinate system
μ	–	Shear modulus
ν	–	Poisson's ratio
π_p	–	Total potential energy
σ_e	–	Effective stress
$\{\sigma\},\sigma_{ij}$	–	Stress vector and components
τ	–	shear stress
Φ	–	Elliptical integral
ϕ	–	Elliptical angle defined in Fig. 17
ψ	–	Groove angle defined in Fig. 4

Subscripts

m   -   Element 'm'

max   -   Maximum value

Superscripts

e   -   Elastic portion

p   -   Plastic portion

T   -   Transpose of a matrix

*   -   Normalized or modified value

GLOSSARY OF ABBREVIATIONS

ASTM   — American Society for Testing and Materials

COD   — Crack Opening Displacement

DCB   — Double Cantilever Beam

DT   — Double Torsion

LEFM   — Linear Elastic Fracture Mechanics

SIF   — Stress Intensity Factor

2-D, 2D — Two-Dimensional

3-D, 3D — Three-Dimensional

CHAPTER I

INTRODUCTION

The double torsion test technique was originally developed by Outwater and Gerry [1]* at the University of Vermont to determine the fracture toughness of glass. The test has been successfully applied to other materials, such as ceramic materials [2,3] polymers [4,5], composite materials [5,6], zinc based die casting alloys [7], cast and wrought aluminum base alloys [8,9,10], steel, titanium [11,12], certain cast irons [13,14,15], and tool materials such as tungsten carbides [16,17]. As a whole, the results obtained have correlated well with those provided by standard ASTM methods.

The double torsion (DT) specimen is essentially an elastic plate containing a crack with a curved profile. Based on the principal of conservation of energy, Outwater and Gerry [1,10] derived a fracture toughness (K_{IC}) calibration equation for the DT test. The basic calibration equation which will be discussed in Chapter III, implies that the stress intensity factor (SIF) is <u>independent of the crack length.</u> This feature could have some valuable assets, for example, simplifying the measurement of K_{IC} when compared with current standard ASTM tests. Additionally, several K_{IC} values may be obtained

*Numbers in brackets designate references at the end of the dissertation.

from a single specimen. This in turn leads to the exciting possibility of mapping K_{IC} values along a particular orientation, for example, along or across the rolling or forging direction in a wrought part. It will also be seen that a further advantage of the test arises from the fact that it permits the measurement of K_{IC} after or before a subcritical crack growth test [18,19]. The DT test has thus become increasingly popular especially with investigators working in ceramics [20,21,22] and indeed has been recognized in several texts in the area of brittle fracture mechanics as a widely accepted technique, see for example Lawn and Wilshaw [23].

The somewhat complex nature of the crack front configuration, the loading conditions and various other factors, such as the side grooving and the plastic zone size, render the interpretation of the stress state, and the nature of both crack formation and extension difficult. The main objective of the present investigation is to verify the integrity of this versatile fracture toughness test as well as to provide a fuller understanding of the factors mentioned above. An extensive finite element analysis has been performed to meet this objective. In order to assure a high degree of accuracy of the results, a special wedge element has been developed to represent the elastic crack-tip singularity. The double torsion finite element model assembled is composed of these special wedge elements around the usually curved crack front and regular isoparametric solid elements elsewhere. The stress intensity factor, K, is calculated from the displacements in the special elements. The new special collapsed

fifteen-node elements used in the present analysis were modified from a former special collapsed six-node element which has been developed by D. M. Tracey [24].

Chapter I will serve as an overview of the DT test. Chapter II deals with the basic concepts of linear fracture mechanics and a brief survey of different finite element techniques that have been already developed for the fracture analysis.

For a valid K_{IC} test, the testing procedures and specimens need to be appropriately specified. Some important features are presented in Chapter III ranging from the testing calibration to the K_{IC} criterion. Some other fracture toughness tests are also included for comparison. In view of the stage of development of fracture toughness testing, a certain degree of speculation could not be avoided. This is due to difficulties in understanding the observed phenomena. Where appropriate, speculative discussions presented in Chapter III are limited to the explanation of size effects and using the K_{IC} criterion for the mixed mode application. It should be noted that in testing tough materials of moderate yield strength, the required dimensions of the ASTM specimens generally are a major limitation in determination of K_{IC}.

Chapter IV contains a complete description of the formulation of the three-dimensional finite element model as well as the special wedge element. In Chapter V, the solutions obtained using this new approach are compared with Tracey's six-node element solutions and other published numerical solutions. In addition to using this

special element, in a few cases, the stress intensity factors for the specimens considered are also calculated by a method of using distorted collapsed quadratic elements [25] and also by using distorted natural quadratic elements [26]. The distorted quadratic elements, which are shown to embody the inverse square root singularity characteristic, are similar to those developed by Henshell and Shaw [27] and Barsoum [25, 28]. The DT model with a quarter-elliptical or a straight crack front is analyzed by the finite element technique developed in Chapter IV. The results and discussions are presented in Chapters VI and VII. The groove effect is discussed in Chapter VIII. The subject of the crack tip plastic zone size, presented in Chapter IX, is examined by a two-dimensional (2-D) elastic-plastic analysis. This elastic-plastic analysis was aided by a general purpose finite element computer code developed by the Westinghouse Electric Corporation [29]. With a minor modification, this computer code is capable of handling a 2-D elastic-plastic fracture problem. Conclusions are presented in Chapter X.

After the completion of the work presented here, the paper of Trantina [30] became available. In this paper Trantina used the regular constant strain finite element model to analyze the DT test. His DT model, in many aspects, is similar to the model with a straight crack front. Therefore, his results will be discussed in Chapter VII which deals with the analysis of the DT model with a straight crack front. It should be mentioned that to describe the stress or dis-

placement distributions near the crack front, the finite element model with embedded singularity is more reliable than the finite element model with regular elements only.

CHAPTER II

COMPUTATIONAL METHODS FOR
LINEAR FRACTURE MECHANICS

The concept of applying linear elastic fracture mechanics
(LEFM) to the prediction of strength and life of cracked structures
has become a widely adopted engineering practice. The basic assump-
tion made in LEFM is that all engineering materials possess flaws or
mechanical defects no matter how carefully they are fabricated. The
concept is to focus attention in a small region around the front edge
of a particular crack where fracture is most likely to take place
and to ensure that the surrounding material has adequate toughness.
LEFM provides a means for investigating flaw sensitivity and resis-
tance of materials to flaw growth.

The theory of linear elastic fracture mechanics is based on
the idea of Griffith's energy criterion [31,32] which states that
the increase in potential energy due to the surface energy require-
ments of crack extension must be balanced by a decrease in the strain
energy and the potential of the applied forces. This energy balance
concept is utilized to determine whether the crack will grow or not
for a particular geometry of the structure, loading condition and
material properties. It was shown by Irwin [33] that Griffith's
energy criterion of the cracked structure can be characterized by a
singular stress distribution around the crack tip. In other words,

the presence of a crack in a structure is essentially a problem of mathematical singularity of stresses at the crack tip. Irwin also showed that the stress distribution in the neighborhood of the crack tip is proportional to the inverse square root of the distance from the crack tip and is also characterized by a set of parameters called stress intensity factors, which represent the strength of the singularity.

The Stress Distribution at the Crack Front

A crack in a solid can be propagated in three different modes as illustrated in Fig. 1. Normal stresses give rise to the "opening mode" denoted as mode I. In-plane shear results in mode II or "sliding mode". The "tearing mode" or mode III is caused by out-of-plane shear. The superposition of the three modes describes the general case of cracking.

The near crack-edge and displacement fields associated with each mode were derived by Irwin [33] based on the method of Westergaard [34]. Modes I and II can be analyzed as two-dimensional plane extensional problems which are subdivided as symmetric and skew-symmetric, respectively, with respect to the crack plane. Referring to Fig. 2 for notation, the near field stress components σ_{xx}, σ_{yy}, and σ_{xy} which are same for all plane strain, plane stress, and generalized plane stress are given below:

Symmetric Case (Mode I)

$$\sigma_{xx} = \frac{K_I}{(2\pi r)^{1/2}} \cos \frac{\theta}{2} \left\{ 1 - \sin \frac{\theta}{2} \sin \frac{3\theta}{2} \right\} + 0(1)$$

$$\sigma_{yy} = \frac{K_I}{(2\pi r)^{1/2}} \cos \frac{\theta}{2} \left\{ 1 + \sin \frac{\theta}{2} \sin \frac{3\theta}{2} \right\} + 0(1) \qquad (2\cdot1)$$

$$\sigma_{xy} = \frac{K_I}{(2\pi r)^{1/2}} \sin \frac{\theta}{2} \cos \frac{\theta}{2} \cos \frac{3\theta}{2} + 0(1)$$

Skew-Symmetric Case (Mode II)

$$\sigma_{xx} = - \frac{K_{II}}{(2\pi r)^{1/2}} \sin \frac{\theta}{2} \left\{ 2 + \cos \frac{\theta}{2} \cos \frac{3\theta}{2} \right\} + 0(1)$$

$$\sigma_{yy} = \frac{K_{II}}{(2\pi r)^{1/2}} \sin \frac{\theta}{2} \cos \frac{\theta}{2} \cos \frac{3\theta}{2} + 0(1) \qquad (2\cdot2)$$

$$\sigma_{xy} = \frac{K_{II}}{(2\pi r)^{1/2}} \cos \frac{\theta}{2} \left\{ 1 - \sin \frac{\theta}{2} \sin \frac{3\theta}{2} \right\} + 0(1)$$

where K_I and K_{II} are the stress intensity factors corresponding to the opening and sliding modes of fracture and the term $0(1)$ indicates the order of magnitude 1.

As discussed in Appendix A, it may be found that in the absence of body forces, the stress intensity factors K_I and K_{II} in isotropic elasticity are independent of the elastic constants if the loads are self-equilibrating (the resultant force vanishes on each

boundary). Also, K_I and K_{II} are the same for plane strain and plane stress cases.* Additional discussion may be found in references [35, 36].

It should be remembered that the z-component stress and general state of displacement for plane strain and plane stress are different. In plane strain, $\sigma_{zz} \neq 0$ and $w=0$ while, in plane stress, $\sigma_{zz}=0$ and $w \neq 0$ where w is the displacement in z direction.

Mode III also can be regarded as the 2-D anti-plane shear (or torsion) problem. The elastic stress field near the crack border is

$$\sigma_{xz} = - \frac{K_{III}}{(2\pi r)^{1/2}} \sin \frac{\theta}{2} + 0(1)$$

$$\sigma_{yz} = \frac{K_{III}}{(2\pi r)^{1/2}} \cos \frac{\theta}{2} + 0(1)$$

(2·3)

where K_{III} is known as the stress intensity factor for the tearing mode fracture. The K-factors (K_I, K_{II}, K_{III}) govern the intensity or magnitude of the local stresses. Alternatively, they may be mathematically viewed as the strength of the $1/\sqrt{r}$ stress singularities at the crack edge and then can be defined as

$$K_I = \lim_{r \to 0} \sigma_{yy} (2\pi r)^{1/2} \Big|_{\theta=0}$$

---

*The term "plane stress" is used, whereas "generalized plane stress" is implied. A discussion distinguishing "plane stress" from which "generalized plane stress" can be found in Appendix A.

$$K_{II} = \lim_{r \to 0} \sigma_{xy} (2\pi r)^{1/2} \Big|_{\theta=0}$$

$$(2 \cdot 4)$$

$$K_{III} = \lim_{r \to 0} \sigma_{yz} (2\pi r)^{1/2} \Big|_{\theta=0}$$

For a general three-dimensional (3-D) crack with an arbitrary smooth crack front, the stress state near the crack border was first carried out by Kassir and Sih [37]. Referring to a triple orthogonal system x, y, z with origin at 0 and x-axis normal to the crack front as shown in Fig. 3, the 3-D stress distribution around the crack front is given below.

$$\sigma_{xx} = \frac{K_I}{(2\pi r)^{1/2}} \cos \frac{\theta}{2} (1 - \sin \frac{\theta}{2} \sin \frac{3\theta}{2})$$

$$- \frac{K_{II}}{(2\pi r)^{1/2}} \sin \frac{\theta}{2} (2 + \cos \frac{\theta}{2} \cos \frac{3\theta}{2}) + 0(1)$$

$$\sigma_{yy} = \frac{K_I}{2(\pi r)^{1/2}} \cos \frac{\theta}{2} (1 + \sin \frac{\theta}{2} \sin \frac{3\theta}{2})$$

$$+ \frac{K_{II}}{(2\pi r)^{1/2}} \sin \frac{\theta}{2} \cos \frac{\theta}{2} \cos \frac{3\theta}{2} + 0(1)$$

$$\sigma_{zz} = \frac{K_I}{(2\pi r)^{1/2}} 2\nu \cos \frac{\theta}{2} - \frac{K_2}{(2\pi r)^{1/2}} 2\nu \sin \frac{\theta}{2} + 0(1)$$

$$\sigma_{xy} = \frac{K_I}{(2\pi r)^{1/2}} \sin \frac{\theta}{2} \cos \frac{\theta}{2} \cos \frac{3\theta}{2}$$

$$+ \frac{K_{II}}{(2\pi r)^{1/2}} \cos \frac{\theta}{2} (1 - \sin \frac{\theta}{2} \sin \frac{3\theta}{2}) + 0 \ (1)$$

$$\sigma_{yz} = \frac{K_{III}}{(2\pi r)^{1/2}} \cos \frac{\theta}{2} + 0(1) \tag{2.5}$$

$$\sigma_{zx} = - \frac{K_{III}}{(2\pi r)^{1/2}} \sin \frac{\theta}{2} + 0(1)$$

where r and θ are defined in xy plane as shown in Fig. 3, and ν is Poisson's ratio. Comparison of the stresses in Eq. (2·5) with those given by Eqs. (2·1), (2·2), and (2·3) shows that for any small region surrounding the outer boundary of a plane of discontinuity, the stresses correspond locally to a state of antiplane shear super-imposed on a state of plane strain. Note that the stresses σ_{xx}, σ_{yy}, and σ_{zz} in Eq. (2·5) satisfy the 2-D plane strain relationship, i.e.

$$\sigma_{zz} = \nu(\sigma_{xx} + \sigma_{yy}) \tag{2.6}$$

In three-dimensional problems, however, the stress intensity factors also depend on the curvature of the crack front. At sharp edges such as corners on the crack border, stress singularities of orders other

than $r^{-1/2}$ may exist, hence Eq. (2·5) is no longer valid.

The corresponding local displacement may be found as

$$u = \frac{K_I}{\mu} \sqrt{\frac{r}{2\pi}} \cos \frac{\theta}{2} [1 - 2\nu + \sin^2 \frac{\theta}{2}]$$

$$+ \frac{K_{II}}{\mu} \sqrt{\frac{r}{2\pi}} \sin \frac{\theta}{2} [2 - 2\nu + \cos^2 \frac{\theta}{2}] + 0(r)$$

$$(2·7)$$

$$v = \frac{K_I}{\mu} \sqrt{\frac{r}{2\pi}} \sin \frac{\theta}{2} [2 - 2\nu - \cos^2 \frac{\theta}{r}]$$

$$- \frac{K_{II}}{\mu} \sqrt{\frac{r}{2\pi}} \cos \frac{\theta}{2} [k - 2\nu - \sin^2 \frac{\theta}{2}] + 0(r)$$

$$w = \frac{K_{III}}{\mu} \sqrt{\frac{2r}{\pi}} \sin \frac{\theta}{2} + 0(r)$$

where displacement components u, v, w are referred to the local coordinate system x, y, z as shown in Fig. 3, μ is the shear modulus and $0(r)$ denotes the order of magnitude r.

The Need for the Finite Element Method

A variety of methods have been developed to determine the stress intensity factor. In cases of a simple idealized geometry use can be made of closed form analytical methods. But for a relatively complicated geometry or boundary condition, even in the 2-D case, the closed form solution becomes extremely difficult if not impossible.

Several numerical techniques have been developed to determine the stress intensity factors of the crack problem in fracture mechanics with acceptable accuracy. They include boundary collocation [38, 39], approximate conformal mapping [40, 41], boundary integral equation [42, 43] and finite element method. On account of mathematical difficulties, boundary collocation and conformal mapping methods are limited in application to two-dimensional problems. The boundary integral equation method is not a general purpose solution tool with different element capabilities, such as the finite element method and has some other limitations [43]. Because of the complication of the 3-D specimen geometry, crack configuration and loading condition of the DT test, the finite element approach is probably the most suitable method presently available to interpret the DT results. The method has great versatility: it permits treatment of 3-D problems, it allows the analysis of complicated geometries, arbitrary boundary conditions, and rather general material properties, it alos permits the use of elastic-plastic elements to include crack tip plasticity.

The application of the finite element method to determine the stress intensity factors has seen rapid progress. Excellent reviews of this method, as well as other analytical or numerical methods were given by Sih [35] and Rice and Tracey [44]. Comprehensive surveys for the finite element method were compiled by Gallagher [45], Hilton and Sih [46], and Pian [47]. The most recent discussion on 3-D finite element fracture problems has been contributed by

Kathiresan [48]. A brief discussion of the various finite element procedures to derive stress intensity factors will now be presented.

Finite Element Methods in Fracture Mechanics

Based on choosing the unknown parameters, the finite element method can be classified into three different approaches, namely the displacement approach, the force approach, and the hybrid approach. The displacement approach is the most common technique used to determine the stress intensity factors for cracked structures. Most techniques discussed in this section are based on the displacement approach.

In order to insure convergence to the correct solution, it is necessary that the elements which immediately surround the crack edge are capable of representing the corresponding singularity. The early finite element calculations for stress intensity factors, involving the use of relatively small standard elements in the vicinity of the crack edge, have been found to be unreliable and are not mentioned here. A number of special crack tip elements, which admit the crack tip stress singularity, have been developed and used to yield accurate solutions for fracture problems.

1. Circular Crack Tip Element

This element, in the shape of small circular disk centered at the crack tip, was developed by Wilson [49] for elastic problem, and

extended to elastic-plastic problems by Hilton and Hutchinson [50].
The stiffness of the element is formed by integrating the strain-
energy density of the dominant $r^{-1/2}$ singularity over the circular
cross section of the element. Regular elements cover the remainder
of the model. The undetermined parameters in the formulation are K
and the displacements of nodes not lying on the circular crack-tip
element boundary. An improved version of the special crack tip ele-
ment has been developed by Wilson [51] who includes higher order
terms of the asympototic elastic expansion. A polygonal crack tip
element which is also based on the asymptotic solution has been pre-
sented by Byskov [52].

2. Pie-Shaped Element

Tracey [53] has proposed the use of pie-shaped elements to
surround the crack tip. Each of these isoparametric elements con-
tains an interpolation function which varies as the square root of
the distance from the crack tip. Tracey [24] has improved the
pie-shaped element for 3-D geometries. Raju and Newman [54] also
used Tracey's 3-D element to analyze some fracture specimens.
Recently, Blackburn and Hellen [55] have developed a 3-D wedge
element similar, in many respects, to Tracey's elements.

3. Hybrid Element

A hybrid finite element procedure was developed and applied to
crack problems by Pian et al. [56]. They used an assumed stress-

hybrid model to develop a special element at the crack tip. The assumed variables in this model are the interior stresses and the boundary displacements. Atluri et al. [57, 58] developed a displacement hybrid finite element for treatment of plane crack problems. Singular behavior of tractions and displacements is taken into account in the hybrid elements. Recently, Atluri and his associates have extended the displacement hybrid element to study the elastic-plastic stress states around cracks [58], the stress intensity factors in plate structure [59], and as mentioned before, 3-D cracked structures [48, 60].

4. Distorted Quadratic Element

Distorted quadratic elements, which are shown to embody the inverse square root singularity characteristic, have been developed by Henshell and Shaw [27] and Barsoum [25]. The singularity of the distorted element is obtained by distorting the regular quadratic isoparametric element by moving the midside nodes near the crack edge to the quarter points. It has been shown that this distortion approach is effective for both collapsed and natural isoparametric elements [26]. The distorted collapsed element is formed by collapsing one side of a distorted quadrilateral element to a triangular element (2-D elements) or by collapsing one face of a distorted solid element to a wedge element (3-D elements). The distorted natural element originally has triangular or wedge shape and is formulated in terms of triangular coordinates.

K-Estimates from the Finite Element Method

Once the numerical solution has been obtained for a particular finite element representation, crack-tip stress intensity factors can be estimated by the use of established crack tip relations. The methods of estimation are based on the fact that displacement, stress, strain energy, and other parameters are directly related to the stress intensity factors. These methods were originally developed for coupling with the results obtained from the conventional finite element model. Clearly, if the finite element model with embedded singularity is used, a more accurate K-estimation can be obtained.

(1) Displacement Method

The displacement method involves a correlation of the finite element nodal point displacements in the vicinity of the crack tip with the well-known crack tip displacement equations. The procedure here is to plot the product of $r^{1/2}$ with some displacement component (say v), as a function of distance along a ray emanating from the tip, and to extrapolate this as a smooth curve to the tip, so as to estimate K. Kobayashi et al. [61] and Chan et al [62] found that displacements at a number of nodes on the crack surface give a good estimate of stress intensity factor. The same approach with the elements with an embedded singularity were carried out by Tracey [24, 54], Blackburn and Hellen [55], and Kathiresan [48]. If singular elements are used, only one or two nodal displacements near the tip are required to estimate the stress intensity factor with ex-

cellent accuracy.

(2) Stress Method

The stress method for determining stress intensity factors is similar to the displacement method. The nodal point stresses are correlated with well-known crack tip stress equations. Chan et al. [62] found that good results could be obtained from the σ_{yy} stress component on the $\theta=0$ plane.

(3) Energy Method

As shown by Irwin [33], the crack tip stress intensity factor can be related to the elastic energy rate, G, by the following relation in a 2-D problem

$$G = \frac{(1+\nu)}{E} \left[\kappa \left(K_I^2 + K_{II}^2 \right) + K_{III}^2 \right] \qquad (2 \cdot 8)$$

where E is Young's modulus,

$$\kappa = (1-\nu) \qquad \text{for plane strain, and}$$
$$\kappa = \frac{1}{1+\nu} \qquad \text{for plane stress.} \qquad (2 \cdot 9)$$

The elastic energy release rate can be related to the rate of change of compliance C, the inverse spring constant, with crack extension by the equation

$$G = \frac{P^2}{2} \frac{\partial C}{\partial A} \qquad\qquad (2 \cdot 10)$$

where P is applied load and A is the crack area. Dixon and Pook [63] calculated the compliance of a cracked structure for a number of different crack lengths by the finite element technique and then by means of equation (2·10) calculated the energy release rate.

This method is strictly applicable to pure mode I, mode II, or mode III case in which the crack is assumed to propagate along the original crack plane. The disadvantage of this method is that it demands at least two separate finite element solutions of the structure. Parks [64], keeping this disadvantage in mind, suggested the novel concept that the rate of change of total potential energy with respect to crack length can be expressed in terms of the rate of change of the global stiffness matrix. Thus by considering the change of very few element stiffness matrices at the crack tip, the strain energy release rate can be estimated. Hellen [65] also used the same approach terming it the method of virtual crack extension. He also pointed out that this method can be used to determine the direction of maximum energy release rate in the case of mixed mode problems.

(4) J-Integral Method

The energy line integral, J, as formulated by Rice is defined for 2-D problems as [66]

$$J = \int_{\Gamma} \left\{ \left(w_s - \sigma_{xx} \frac{\partial u}{\partial x} - \sigma_{xy} \frac{\partial v}{\partial x} \; dy \right) \right.$$

$$\left. + \left(\sigma_{yx} \frac{\partial u}{\partial x} + \sigma_{yy} \frac{\partial v}{\partial x} \right) dx \right\}$$

(2·11)

where w_s is the elastic strain energy density, and Γ is an arbitrary contour surrounding the crack tip. The integral has a value which is independent of the particular path chosen; there is no restriction that the material be linearly elastic, but instead only that its stress-strain relations be consistent with the existence of a strain-energy function. The physical interpretation of J is as that of the elastic energy release rate, G. In the case of a linear elastic material [66], one has

$$J = G = \frac{(1+\nu)}{E} \left[\kappa \; (K_I^2 + K_{II}^2) + K_{III}^2 \right]$$

(2·12)

where κ is defined in Eq. (2·9). By numerically evaluating the J-integral for the finite element solution over a path surrounding the crack tip, an estimate of the crack tip stress intensity factor can be made by use of equation (2·12). This method was employed by Chan et al. [62]. Since the general 3-D relationship between K and G (or J) is still not available, the J-integral and energy method are restricted to 2-D problems. However, the displacement and stress methods are in principle applicable to any 2-D or 3-D crack problems provided that the near field character of the displacement or stress is known.

CHAPTER III

AN APPRAISAL OF THE DOUBLE TORSION
TEST AND RELATED TOPICS

The advantages of the DT test procedures have been mentioned
in Chapter I. However, the major effort of this research is the
theoretical study of the validity of the DT test. The validity of
results may depend on many factors, especially, the testing criterion,
calibration procedure, and specimen dimensions. This chapter
appraises the basic concepts of these factors. For the most, the
apprasials are based on the results obtained from other fracture
toughness tests, such as the ASTM standard tests and the double
cantilever beam (DCB) test. Consequently, the comments of the
appraisal are applicable to these tests or to the fracture mechanics
in general.

The Calibration Equation of the Double Torsion Test

The Griffith energy criterion for fracture [32] indicates that
a crack will grow if the energy required to form an additional crack
surface dA can just be delivered by the system. Consequently, the
equilibrium condition is defined as that for which the change in
energy for the system is zero, i.e.,

$$\frac{d}{dA_c} (W_s - W_e + W_c) = 0 \tag{3·1}$$

where W_s is the strain energy contained in the system, W_e is the work performed by the external loads and W_c is the energy for crack extension. Usually $\frac{dW_c}{dA}$ is replaced by G_c and then Eq. (3·1) becomes

$$G_c = \frac{d}{dA_c} (W_e - W_s) \tag{3·2}$$

where G is called the elastic energy release rate (also referred to as the crack driving force), and the subscript c represents the critical value.

The double torsion specimen is essentially a thick plate containing a crack with a curved profile. Each half of the specimen can be regarded as a prism with rectangular cross-section rigidly held at one end and subjected to a torque, M_t, at the other end (see Figure 4). Under the action of the torque, the load-application end undergoes a relative angle θ. When the crack increases in size by an amount dA, the angle will increase by an amount $d\theta$. Each half of the specimen is loaded by a torque, M_t, therefore the total work done is $2M_t d\theta$. It follows that:

$$G_c = 2M_t \frac{d\theta}{dA_c} - \frac{dW_s}{dA_c} \tag{3·3}$$

If deformations are elastic, the strain energy contained in the specimen is then

$$W_s = \frac{1}{2} (2M_t)\theta \qquad (3\cdot4)$$

Using a torsional compliance, C_t, the angle θ can be replaced by

$$\theta = C_t M_t \qquad (3\cdot5)$$

Substituting Eqs. (3·4) and (3·5) into Eq. (3·3) yields

$$G_c = 2M \frac{d(C_t M_t)}{dA_c} - \frac{d(C_t M_t^2)}{dA_c}$$

$$= 2M_t^2 \frac{\partial C_t}{\partial A_c} + 2 C_t M_t \frac{\partial M_t}{\partial A_c} - M_t^2 \frac{\partial C_t}{\partial A_c} - 2C_t M_t \frac{\partial M_t}{\partial A_c} \qquad (3\cdot6)$$

The terms containing $\dfrac{\partial M_t}{\partial A_c}$ cancel. This means that G_c is independent of whether or not the load is constant:

$$G_c = M_t^2 \frac{dC_t}{dA_c} \qquad (3\cdot7)$$

Experimentally, it is found that the DT cracks propagate, with the crack front taking up a curved form. Some investigations [8, 9, 10, 16, 17] have observed that initial fatigue cracks do not penetrate the upper surface. However, other results [30] have been reported

that the crack can penetrate the upper surface. Figs. 5·a and 5·b illustrate crack fronts for the penetrated and unpenetrated DT specimens, respectively. It has also been observed that the shape of the crack front is independent of crack length, i.e. it remains unaltered during crack propagation [67]. Then the critical crack propagation area, dA_c, can be expressed as

$$dA_c = t_c \, dc, \qquad\qquad (3\cdot8)$$

for the penetrated specimen, and

$$dA_c = b \, dc, \qquad\qquad (3\cdot9)$$

for the unpenetrated specimen, where t_c, b, and c are defined in Figure 4 or 5. Almost all reported unpenetrated cracks propagate with a distance very close to the upper surface, i.e., $b \approx t_c$. Eqs. (3·8) and (3·9) become identical. Also, the critical crack area A_c can be expressed by

$$A_c = t_c \, c_e \qquad\qquad (3\cdot10)$$

where c_e is the effective crack length which can be treated as the length of the torsional prism. Then, the angle of twist in one-half of the DT specimen is

$$\theta = \frac{M_t c_e}{I_p \mu} \qquad (3\cdot 11)$$

Where I_p is the polar moment of inertia of one half of the DT specimen. The torsional compliance becomes

$$C_t = \frac{\theta}{M_t} = \frac{c_e}{I_p \mu}$$

From Eq. (3·8), the derivative of the compliance is of the form

$$\frac{dC_t}{dA_c} = \frac{1}{t_c} \frac{dC_t}{dc_e} = \frac{1}{t_c I_p \mu} \qquad (3\cdot 12)$$

When the DT specimen is loaded as shown in Figure 4, the torque is

$$M_t = \frac{P_c W_m}{4}$$

where P_c is the critical load, and $\frac{W_m}{2}$ is the distance between the closed bottom support and the load.

Substituting in Eq. (3·7) for M_t and $\frac{dC_t}{dA_c}$ yields

$$G_c = \frac{(P_c W_m)^2}{16 t_c I_p \mu} \qquad (3\cdot 13)$$

As shown in Fig. 4, the DT test involves a four-point bending type of loading, with theoretically no shear stress between the central loading points. Thus, it would appear to possess only a mode I type fracture. If a plane strain situation is assumed, using Eq. (2·8), it follows that:

$$K_{IC} = \left[\frac{EG_c}{1-\nu^2}\right]^{1/2} = P_c \ W_m \ [\frac{E}{16(1-\nu^2)t_c I_p \mu}]^{1/2}$$

Since $\mu = \frac{E}{2(1+\nu)}$, the above equation becomes,

$$K_{IC} = K_{cal} = P_c \ W_m \ [\frac{1}{8(1-\nu)t_c I_p}]^{1/2} \tag{3·14}$$

This is the form of the calibration equation, first, given by Outwater and Gerry [1] and discussed in depth by Outwater, Murphy, Kumble and Berry [10], although the approach taken above differs in several aspects. The calibration equation is, of course, only a rough approximation of the stress intensity factor. The numerical verification of this equation will be presented in Chapter VII.

The Interdependence of K_C and Specimen Geometry

It has been widely observed in fracture toughness testing generally that the magnitude of the critical SIF (K_C) depends strongly on the nature of the fracture growth surfaces involved. Surfaces are normal (flat) or are slanted at approximately 45° to

to the direction of loading or further are sometimes made up of both slant and flat fracture types. Fig. 6 schematically displays the various fracture surface appearances of a given metal. These different patterns may be obtained by either changing the temperature or the specimen thickness relative to the crack length [68,69]. When the predominantly slant fracture pattern (Fig. 6·a) is observed, the material exhibits a maximum K_C. Alternately, as the thickness increase (keeping temperature constant), the predominantly flat fracture surface (Fig. 6·c) is developed and the K_C drops sharply to a level that may be one-third (or less) than that of the maximum value [69]. One very important aspect of this lower level of K_C is that it does not decrease further with increasing thickness. Therefore, this minimum K_C value can be considered as a material property, K_{IC}, and depends only on metallurgical factors. The usual dependence of K_C upon the fracture surface appearance and specimen thickness in fracture toughness tests is given diagrammatically in Fig. 6·d.

Since LEFM can only be used with good accuracy when the crack size is a multiple of the plastic zone size, the standard ASTM (American Society for Testing and Materials) procedure requires that the crack size c must be [70, 71]

$$c \geq 2.5 \left(\frac{K_{IC}}{\sigma_y}\right)^2 \qquad\qquad (3\cdot15)$$

where $\left(\frac{K_{IC}}{\sigma_y}\right)^2$ is proportional to the plastic zone size radius. A

similar ASTM requirement holds for the thickness (t):

$$t \geq 2.5 \left(\frac{K_{IC}}{\sigma_y}\right)^2 \qquad\qquad (3 \cdot 16)$$

Nevertheless, there is still no satisfactory explanation for the fracture appearance or thickness dependence of K_C, although some models for the thickness effect have been proposed [69,72]. The shape of the curve in Fig. 6·d or the ASTM thickness requirement Eq. (3·16) was explained plausibly by a concept of crack tip plastic zone under plane stress or plane strain conditions [72]. However in small scale yielding fracture mechanics, plane stress elastic-plastic solutions should not be used to analyze the state of affairs near crack front. This can be envisaged from Eqs. (2·5) and (2·6), and also can be deduced using treatments which are shown in Appendices A and B in detail. Additionally, misleading and sometimes incorrect attempts have been made to quantify the actual 3-D nature of the crack growth pattern on the basis of 2-D plasticity models. A detailed discussion of such misleading attempts using 2-D analysis to describe fracture appearance in ASTM approved fracture toughness tests is presented in Appendix B.

It also needs to be pointed out that in addition to being influenced by a change of thickness or temperature, slant fracture can be prevented by providing the specimen with side grooves as illustrated in Fig. 4 for a DT specimen and in Fig. 7·b for a compact specimen.

Recently, based on a 3-D finite element analysis, the ASTM 2-D calibration (see Appendix B) has been modified by Shih [73] for the side-grooved compact specimen. Using this modified calibration, Shih et al. [73,74] examined ASTM A533-B steel. They found experimentally that a side grooved specimen of only 4 inches in thickness (t) provided a valid K_{IC} value. The yield strength, σ_y, and the fracture toughness, K_{IC}, of A533-B steel are about 50 ksi and 180 ksi$\sqrt{in.}$, respectively. If the ungrooved ASTM specimen is used, according to Eq. (3·16), a specimen thickness greater than 33 inches is required for a valid K_{IC} test [72]. It should be borne in mind that the net specimen thickness at the groove (t_c) is less than the specimen thickness (t) for grooved specimens (see Fig. 7·b). In addition to the compact specimen, the use of the side-grooves has been frequently included with other specimens, especially, the DCB type specimen. Mostovoy et al. [75] used this specimen to evaluate the fracture toughness of 7075-T651 aluminum alloy. This work showed that the minimum net specimen thickness (t_c) is less than 0.075 in. However, the corresponding specimen thickness for the ASTM fracture toughness tests should be about 0.35 in. Similar results can also be found in Reference [76] for determining the fracture toughness of beryllium and Reference [77] for mild steel.

Some consistent results have also been found in the DT test. Kumble et al. [9,10] compared valid ASTM and DT fracture toughness test values from wrought 2124-T851 aluminum alloy and found them to be in precise agreement, even though the grooved DT specimens were of

half the recommended ASTM thickness. Murphy, Kunble, Berry and Outwater [8] obtained reasonable double torsion fracture toughness values with a 1/3-in. specimen prepared from a 1.0-in. 357-T6 cast aluminum alloy, which would have required an ASTM type specimen of at least twice the size tested. Moreover, the experimental results of Ten Haagen and Berry [13,14,15] have shown that the minimum net specimen thicknesses are 0.15 in. for a ferritic ductile cast iron and 0.04 in. for the 2124-T851 wrought aluminum alloy. These values represent only 8% of a valid ASTM specimen thickness.

Thus, it may be concluded that, by the introduction of the side grooves, only a relatively thin specimen is needed for measuring K_{IC} compared with ASTM approved test specimens. This implies that in fracture toughness testing, the critical SIF will not vary with decreasing thickness as long as the crack forms an essentially flat fracture surface. Furthermore, it follows that the formation of the flat fracture growth surfaces may be obtained either with or without the aid of side grooves. This conclusion reinforces the urgent need for the development of some realistic criteria, which could lead to guidelines to regulate specimen geometry. These should adequately explain the dependence of K_C upon the surface appearance of fracture growth associated with the specimen thickness and side-grooving, or upon a plastic instability which will be discussed in the following paragraph.

Returning to the DT test, it should be noted that the specimen concerned is essentially a cracked plate in which localized

yielding and rupture need to occur before they are propagated on a general (large) scale. To fully achieve this condition, i.e. to avoid a plastic instability condition, a minimum specimen thickness may be required to satisfy a particular situation. As mentioned earlier, Ten Haagen and Berry observed that the minimum net specimen thickness is about 8% of the ASTM requirement and the same of order of magnitude of the commonly recognized crack front plastic zone size.* They also observed a distinct drop in K_c value as the specimen thickness fell below the minimum size. The drop of K_c values is apparently due to the plastic instability effect. Therefore, based on the experimental results of Ten Haagen and Berry, a requirement of the net specimen thickness of the DT test may be specified as:

$$t_c \geq 0.25 \; (\frac{K_{IC}}{\sigma_y})^2 \qquad\qquad (3 \cdot 17)$$

A safety factor of approximate 1.3 has been incorporated into the above requirement. This requirement still represents a 90% saving in this dimension when compared with a valid ASTM specimen.

Comments on the K_{IC} Criterion

The concept of the stress intensity factor has been introduced in Chapter II. K_{IC} is measured in terms of the opening mode stress intensity factor K_I. The important distinction between the mathe-

---

*It will be shown that this estimated crack front plastic zone size is adequate. This analysis is presented in Chapter IX.

matical quantity K_I and the material property K_{IC} is similar to the distinction between the elastic stress and the yield strength of a material. According to the Griffith criterion, the fracture toughness is characterized by the amount of crack growth surface and the surface energy generated. As shown in Fig. 6, the slant fracture is a mixed mode fracture growth. Also, in most structural components, cracks are seldom aligned perpendicularly to the direction of loading. Since the K_{IC} fracture criterion is based on the assumption that the crack must always be oriented normally to the applied tensile stress (Mode I fracture), the K_{IC} criterion is thus not applicable to such structures. Therefore, to explain the above stated dependence of K_c and to analyze the mixed mode fracture problem, a general fracture criterion, $\bar{K}_c$, which combines K_I, K_{II}, and K_{III} is required. The general criterion may be expressed by the following mathematical statement

$$\bar{K}_c = \bar{K} (K_I, K_{II}, K_{III}) \qquad (3 \cdot 18)$$

The general criterion in fracture analysis may be seen to be analogous to the von Mises criterion in yielding analysis. The von Mises stress can be directly related to the principal stresses or stress components. The material is yielded when effective stress* reaches some critical value. Similarly, the material is fractured when the effective stress intensity factor $\bar{K}$ reaches the critical value $\bar{K}_c$.

---

*See Eq. (6·2) for definition.

Sih [78] defined a factor, the strain-energy-density factor, which involves all three stress intensity factors. This strain-energy-density factor criterion has been applied to several fracture problems in a mathematical sense [35]. However, the hypotheses made in this criterion still requires a physical verification.

In principle, the energy release rate (G_c) concept can be applied to the mixed mode situation. In pure Mode I fracture situation, Eq. (2·8) can be reduced as

$$G = \begin{cases} \dfrac{(1-\nu^2)}{E} \; K_I^{\,2} & \text{for plane strain} \\[2mm] \dfrac{1}{E} \; K_I^{\,2} & \text{for plane stress} \end{cases} \qquad (3\cdot19)$$

K_I may be solved from this equation,

$$K_I = \begin{cases} \left(\dfrac{G\,E}{1-\nu^2}\right)^{1/2} & \text{for plane strain} \\[2mm] (GE)^{1/2} & \text{for plane stress} \end{cases} \qquad (3\cdot20)$$

Also, for a pure Mode I fracture Eq. (3·18) may becomes

$$\bar{K}_c = K_{IC} \text{ or } \bar{K} = K_I \qquad (3\cdot21)$$

On using Eq. (3·20) this becomes

$$\bar{K} = K_I = \begin{cases} \left(\dfrac{G\,E}{1-\nu^2}\right)^{1/2} & \text{for plane strain} \\[2mm] (GE)^{1/2} & \text{for plane stress} \end{cases} \qquad (3\cdot22)$$

Applying Eq. (2·8) for G, the effective stress intensity factor can be expressed

$$\bar{K} = (K_I^2 + K_{II}^2 + \nu^* K_{III}^2)^{1/2} \tag{3·23}$$

where

$$\nu^* = \begin{cases} \dfrac{1}{(1-\nu)} & \text{for plane strain} \\ (1+\nu) & \text{for plane stress} \end{cases}$$

More generally, Eq. (3·23) becomes

$$\bar{K} = (K_I^2 + A_2 K_{II}^2 + A_3 \nu^* K_{III})^{1/2} \tag{3·24}$$

where A_2 and A_3 are constants and may depend on the appropriate structure geometries.

The merit of this energy release rate concept is that the critical effective stress intensity factor $\bar{K}_c$ directly equals the fracture toughness K_{IC} as shown in Eq. (3·21). By simply assuming $A_2 = A_3 = 1$, the energy release rate criterion (Eq. 3·24) has been applied to predict the structure failure for a mixed mode condition [79]. As with the strain-energy-density criterion, Eq. (3·24) awaits physical and experimental verification. However, the objective of the current study does not attempt to investigate this criterion further but rather to propose an idea here. Also, the writer wishes

emphasize that a great deal of research remains to be done in the general area of fracture mechanics.

CHAPTER IV

FINITE ELEMENT FORMULATION FOR ELASTIC CRACK ANALYSIS

Finite element methods can be formulated from the variational principles of solid mechanics by relaxing the continuity requirements along inter-element boundaries. The combination of different variational principles and different boundary continuity conditions yields numerous types of approximate methods. An approach based on the principle of minimum potential energy as appropriate in conjunction with the Rayleigh-Ritz procedure has been the most successful and versatile method for structural analysis and was employed to formulate the finite elements in the present analysis. The following sections contain the relevant derivations used in the development of the computer program. A more detailed description may be found in Reference [80], for instance.

The Displacement Approach as a Minimization of
Total Potential Energy

The principle of minimum potential energy is the basis for derivation of the displacement element. If the displacement shape functions are chosen such that internal continuity and compatibility between elements across common boundaries is insured, neither internal nor external equilibrium need be considered. Application of the principle of minimum potential energy then furnishes external equilibrium

in terms of the generalized forces and the element stiffness equation. Equilibrium need not exist on the boundaries except at the nodal points. The potential energy (π_p) of a structure is given by the strain energy (W_s) plus the potential energy for surface traction (W_t), surface point loads (W_p), and body forces (W_b), respectively; i.e.,

$$\pi_p = W_s + W_t + W_p + W_b \qquad (4 \cdot 1)$$

The strain energy, W_s, can be written as the sum of the strain energy in each element, $w_s^{(m)}$; i.e.,

$$W_s = \sum_{m=1}^{M} \int_{V_m} w_s^{(m)} \, dV \qquad (4 \cdot 2)$$

where M is the number of elements, and V_m is the volume of the mth element. For an elastic body, the strain energy becomes*

$$W_s = \sum_{m=1}^{M} \int_{V_m} \frac{1}{2} \{\varepsilon\}^T [E] \{\varepsilon\} \, dV \qquad (4 \cdot 3)$$

where $\{\varepsilon\}$ is the strain column vector

   $\{\varepsilon\}^T$ is the transpose of the strain vector

   $[E]$ is the symmetric matrix of elastic constants

---

*Initial strains are left out for simplicity.

In the present Rayleigh-Ritz displacement approach, displacements are the unknown function to be assumed. The assumed displacement function should be kinematically admissible in using the Rayleigh-Ritz method. This means that the displacement function should be selected so that it satisfies the displacement boundary conditions prescribed for the problem itself. However, except for relatively simple problems, it is generally difficult to construct a function that will satisfy these conditions and still be simple enough to permit the necessary mathematical calculations to be carried out. At this point, the advantages of the finite element method become apparent. The key to the finite element method lies in relating the primary unknown function to the individual element, rather than to the total problem. Hence, the geometry of the overall body and the system boundary conditions are of no concern when choosing the unknown function.

Let the displacement $\{f\}$, of an arbitrary point within the element, m, be given by

$$\{f\} = [\bar{N}] \{d\}_m \tag{4·4}$$

where $\{d\}_m$ is the array of nodal displacements of the element m and $[\bar{N}]$ is the shape function matrix which defines the nature of the assumed displacement. The detailed discussion of the shape functions for both the regular and singular element is presented in the next two sections.

Using the small deformation strain-displacement relations, the strain may be gathered into matrix form and symbolized as

$$\{\varepsilon\} = [D] \; \{d\}_m \qquad (4\cdot5)$$

where [D] is obtained from derivatives of $[\bar{N}]$ and will be discussed later.

Substituting of Eq. (4·5) into Eq. (4·3) yields the strain energy:

$$W_s = \sum_{m=1}^{M} \{d\}_m^T \; [k]_m \; \{d\}_m \qquad (4\cdot6)$$

where $[k]_m$, the stiffness matrix of element m, equals

$$\int_{V_m} [D]^T \; [E] \; [D] \; dV$$

The work done (potential lost) by the element surface traction (force per unit area) is equivalent to a generalized traction vector {T} acting on the surface nodes of the element. The potential of the surface tractions can be expressed as

$$W_t = -\sum_{m=1}^{M} \int_{S'} \{f\}^T \; \{T\} \; dS \qquad (4\cdot7)$$

where S' is the portion of the surface on which tractions are prescribed.

Substituting Eq. (4·4) into Eq. (4·7), W_t becomes

$$W_t = -\sum_{m=1}^{M} \{d\}_m^T \int_{S'} [\bar{N}]^T \{T\} \, dS = -\sum_{m=1}^{M} \{d\}_m^T \{r_t\}_m \qquad (4·8)$$

where

$$\{r_t\}_m = \int_{S'} [\bar{N}]^T \{T\} \, dS.$$

The vector $\{r_t\}$ is the force vector associated with the nodal displacement, $\{d\}_m$, of nodes on the surface of loaded elements. It is understood that the equivalent traction vector $\{T\}$ is zero for the element not in contact with S'. In the same manner, the potential of the body force can be expressed as

$$W_b = -\sum_{m=1}^{M} \{d\}_m^T \int_{V_m} [\bar{N}]^T \{B\} \, dV$$

or

$$W_b = -\sum_{m=1}^{M} \{d\}_m^T \{r_b\}_m \qquad (4·9)$$

where $\{r_b\}_m = \int_{V_m} [\bar{N}]^T \{B\} \, dV.$

Here the vector {B} is the equivalent body force vector acting through all the nodes of the element m. If surface point loads $\{P\}_m$ are applied to nodes of the element m by some external agency, the potential of point load is

$$W = -\sum_{m=1}^{M} \{d\}_m^T \{P\}_m$$

or

$$W = -\sum_{m=1}^{M} \{d\}_m^T \{r_p\}_m \qquad (4 \cdot 10)$$

where the nodal load vector $\{r_p\}_m$ equals the applied load vector $\{P\}_m$ and the component of $\{r_p\}_m$ is taken as positive when acting in the same direction as the corresponding nodal displacement. If the point loads $\{P\}_m$ act on the element but not at nodal points, the equivalent nodal loads $\{r_p\}_m$ may be found by viewing the integral of Eq. (4·8) as a summation of forces $\{T\}$ ΔS, where large tractions $\{T\}$ act on small separated area ΔS.

Substituting Eqs. (4·6), (4·8), (4·9), and (4·10) into Eq. (4·1), the total potential energy, π_p, becomes

$$\pi_p = \sum_{m=1}^{M} \{d\}_m^T (1/2[k]_m \{d\}_m - \{r_t\}_m - \{r_p\}_m - \{r_b\}_m)$$

or, more usually

$$\pi_p = \sum_{m=1}^{M} \{d\}_m^T (1/2[k]_m \{d\}_m - \{r\}_m)$$ (4·11)

where

$$\{r\}_m = \{r_t\}_m + \{r_p\}_m + \{r_b\}_m .$$

A global numbering system is introduced for the nodal displacement components. In other words, the summation of Eq. (4·11) implies the expansion of element matrices to "structure size", followed by summation of overlapping terms. Thus, the total potential energy of the structure, as approximated by the finite element procedure, is expressed in terms of the nodal displacement components of the global system as

$$\pi_p = \frac{1}{2} \{U\}^T [K] \{U\} - \{U\}^T \{R\}$$ (4·12)

The potential energy π_p is then minimized with respect to the unknown nodal displacement components thereby obtaining a set of linear algebraic equations as follows form:

$$\frac{\partial \pi_p}{\partial \{U\}} = \left\{ \begin{array}{c} \dfrac{\partial \pi_p}{\partial U_1} \\ \vdots \\ \dfrac{\partial \pi_p}{\partial U_n} \end{array} \right\} = 0$$ (4·13)

where U_i is the nodal displacement component, i refers to the global system, varying from 1 to n, the total number of nodal displacement components (or degrees of freedom). Substituting Eq. (4·13) into the expression for potential energy, Eq. (4·12), yields

$$[K] \ \{U\} \ = \ \{R\} \tag{4·14}$$

where [K] is the total stiffness matrix of the structure and {R} is the generalized load vector. The solution of Eq. (4·14) gives the nodal displacement values. Stresses and strains within an element can be determined directly from the corresponding displacement shape functions.

Mondkar and Powell [81] have employed a Crout reduction procedure to develop a computer program for solving a set of simultaneous algebraic equations. This program is able to solve a large system of equations with reasonable in-core storage and is used for solving the simultaneous equations Eq. (4·14), in the present finite element analysis. The details of the Crout reduction procedure and the computer program listing can be found in the reference cited.

Note, the above derivation is based on the total potential energy without constraints imposed. Because the constrained nodal displacement components in the current research are all specified as zero, the potential energy contributed from the constrained nodal displacement components can be neglected. Only unconstrained (unknown) nodal displacement components need to be determined. The

above derivation can then be used in the present analysis. However, using a Lagrange multiplier concept, the above procedure can be modified to treat generalized constraint conditions. A detail discussion of this modification as well as the Lagrange multiplier concept can be found in Reference [82], for instance.

The Three-Dimensional Regular Isoparametric Element

In the preceding section, the basic formulation for the displacement finite element method was presented. The interpolation functions for the regular isoparametric element are discussed in this section.

The name of "isoparametric" is derived from use of the same interpolation functions to define the element shape as are used to define displacements within the element. Isoparametric element construction represents the "mapping" of a nondimensionalized rectangular element into the actual curved-boundary element geometry. The mapping applies generally, providing some one-to-one correspondence between Cartesian and curvilinear coordinates can be established. Once such coordinate relationships are known, shape functions can be specified in local coordinates, and, by suitable transformations, the element properties established.

The basic element used in the present 3-D elastic analysis is the twenty-node isoparametric brick element. This sixty degree of freedom element is defined in the three-dimensional space coordinates (ξ, η, ζ) associated with twenty shape functions N_i. If x, y, and z are the global Cartesian coordinates, the relation used to define the

mapping as shown in Fig. 8

$$x = \lfloor \bar{N}(\xi, \eta, \zeta) \rfloor \{\bar{x}\}$$

$$y = \lfloor \bar{N}(\xi, \eta, \zeta) \rfloor \{\bar{y}\} \qquad (4 \cdot 15)$$

$$z = \lfloor \bar{N}(\xi, \eta, \zeta) \rfloor \{\bar{z}\}$$

with

$$\{\bar{x}\} = \lfloor x_1 \ x_2 \ \text{-----} \ x_{20} \rfloor^T$$

$$\{\bar{y}\} = \lfloor y_1 \ y_2 \ \text{-----} \ y_{20} \rfloor^T$$

$$\{\bar{z}\} = \lfloor z_1 \ z_2 \ \text{-----} \ z_{20} \rfloor^T$$

$$\lfloor \bar{N} \rfloor = \lfloor N_1 \ N_2 \ \text{-----} \ N_{20} \rfloor$$

where N_1, N_2 ----- are shape functions given in terms of the local coordinates, x_i, y_i, z_i are the Cartesian coordinates of the ith node of the element. The displacement of any point within the element can also be expressed by the same shape functions as used to define the element shape:

$$u = \lfloor \bar{N} \rfloor \{\bar{u}\}$$

$$v = \lfloor \bar{N} \rfloor \{\bar{v}\} \qquad (4 \cdot 16)$$

$$w = \lfloor \bar{N} \rfloor \{\bar{w}\}$$

with

$$\{u\} = \lfloor u_1 \ u_2 \ ----- \ u_{20} \rfloor^T$$

$$\{v\} = \lfloor v_1 \ v_2 \ ----- \ v_{20} \rfloor^T$$

$$\{w\} = \lfloor w_1 \ w_2 \ ----- \ w_{20} \rfloor^T$$

where u_i, v_i, and w_i are the nodal displacements of the element.
Using matrix representation, the above equations yield Eq. (4·4).
From the same above equations, the matrices $\{f\}$, $[\bar{N}]$, and $\{d\}$ defined
in Eq. (4·4) can be expressed as

$$\{f\} = \begin{Bmatrix} u \\ v \\ w \end{Bmatrix}$$

$$[\bar{N}] = \begin{bmatrix} \lfloor\bar{N}\rfloor & 0 & 0 \\ 0 & \lfloor\bar{N}\rfloor & 0 \\ 0 & 0 & \lfloor\bar{N}\rfloor \end{bmatrix} \qquad\qquad (4\cdot17)$$

and

$$\{d\} = \begin{Bmatrix} \{u\} \\ \{v\} \\ \{w\} \end{Bmatrix}$$

The three-dimensional mapping for the 20-node regular iso-
parametric element is schematically shown in Fig. 8. In $\xi\eta\zeta$ space
the element is a cube and bounded by planes ξ, η, $\zeta = \pm 1$. The

corresponding shape functions can be found from Reference [80]:

Corner nodes

$$N_i = \frac{1}{8} (1+\xi\xi_i)(1+\eta\eta_i)(1+\zeta\zeta_i)(\xi\xi_i+\eta\eta_i+\zeta\zeta_i-2)$$

$$\text{for } i = 1, \text{-----}, 8$$

Mid-side node where $\xi_i = 0$

$$N_i = \frac{1}{4} (1-\xi^2)(1+\eta\eta_i)(1+\zeta\zeta_i)$$

$$\text{for } i = 9, \text{-----}, 12$$

(4·18)

Mid-side node where $\eta_i = 0$

$$N_i = \frac{1}{4} (1-\eta^2)(1+\xi\xi_i)(1+\zeta\zeta_i)$$

$$\text{for } i = 13, \text{-----}, 16$$

Mid-side node where $\zeta_i = 0$

$$N_i = \frac{1}{4} (1-\zeta^2)(1+\xi\xi_i)(1+\eta\eta_i)$$

$$\text{for } i = 17, \text{-----}, 20$$

where ξ_i, η_i, and ζ_i are the coordinates at node i in $\xi\eta\zeta$ space, i.e., +1 or -1 (see Fig. 8). The shape functions have the property that N_i is unity at node i and zero at all other nodes.

As shown in the previous section, to construct an element stiffness matrix, the strains which are derivatives of the displacements with respect to x, y, and z axes must be found. The displacements, however, are now functions of the ξ, η, and ζ coordinates. Hence, a relationship between the derivatives with respect to x, y, and z and the derivatives with respect to ξ, η, and ζ should be obtained. By the chain rule of differentiation, the relation is

$$
\begin{Bmatrix} (\ )_{,\xi} \\ (\ )_{,\eta} \\ (\ )_{,\zeta} \end{Bmatrix} = \begin{bmatrix} x_{,\xi} & y_{,\xi} & z_{,\xi} \\ x_{,\eta} & y_{,\eta} & z_{,\eta} \\ x_{,\zeta} & y_{,\zeta} & z_{,\zeta} \end{bmatrix} \begin{Bmatrix} (\ )_{,x} \\ (\ )_{,y} \\ (\ )_{,z} \end{Bmatrix} = [J] \begin{Bmatrix} (\ )_{,x} \\ (\ )_{,y} \\ (\ )_{,z} \end{Bmatrix} \tag{4·19}
$$

where the parentheses represent any differentiable function (displacement, for instance), the subscript "," denotes partial differentiation, and [J] is the Jacobian matrix. Taking derivations appropriately in Eq. (4·15) and arranging the terms in the form of the Jacobian leads to:

$$
[J] = \begin{bmatrix} x_{,\xi} & y_{,\xi} & z_{,\xi} \\ x_{,\eta} & y_{,\eta} & z_{,\eta} \\ x_{,\zeta} & y_{,\zeta} & z_{,\zeta} \end{bmatrix} = \begin{Bmatrix} \lfloor \bar{N} \rfloor_{,\xi} \\ \lfloor \bar{N} \rfloor_{,\eta} \\ \lfloor \bar{N} \rfloor_{,\zeta} \end{Bmatrix} \begin{bmatrix} \{\bar{x}\} & \{\bar{y}\} & \{\bar{z}\} \end{bmatrix} \tag{4·20}
$$

Thus, using the inverse relation from Eq. (4·19), we may write

$$
\begin{Bmatrix} u,_x \\ u,_y \\ u,_z \\ v,_x \\ v,_y \\ v,_z \\ w,_x \\ w,_y \\ w,_z \end{Bmatrix} = \begin{bmatrix} [J]^{-1} & 0 & 0 \\ 0 & [J]^{-1} & 0 \\ 0 & 0 & [J]^{-1} \end{bmatrix} \begin{Bmatrix} u,_\xi \\ u,_\eta \\ u,_\zeta \\ v,_\xi \\ v,_\eta \\ v,_\zeta \\ w,_\xi \\ w,_\eta \\ w,_\zeta \end{Bmatrix} \qquad (4 \cdot 21)
$$

where $[J]^{-1}$ is the inverse of matrix $[J]$.

All three displacements u, v, w are variables in the 3-D element, as are the six strains

$$
\{\varepsilon\} = \lfloor \varepsilon_{xx} \quad \varepsilon_{yy} \quad \varepsilon_{xx} \quad \varepsilon_{xy} \quad \varepsilon_{yz} \quad \varepsilon_{zx} \rfloor^T \qquad (4 \cdot 22)
$$

Linear strain-displacement relations $\varepsilon_{xx} = u,_x, \text{-----}, \varepsilon_{zx} = u,_z + w,_x$ are

$$
\{\varepsilon\} = [SD] \lfloor u,_x \quad u,_y \quad u,_z \quad v,_x \quad v,_y \quad v,_z \quad w,_x \quad w,_y \quad w,_z \rfloor^T \qquad (4 \cdot 23)
$$

where

$$[SD] = \begin{Bmatrix} 1 & 0 & 0 & 0 & 0 & 0 & 0 & 0 & 0 \\ 0 & 0 & 0 & 0 & 1 & 0 & 0 & 0 & 0 \\ 0 & 0 & 0 & 0 & 0 & 0 & 0 & 0 & 1 \\ 0 & 1 & 0 & 1 & 0 & 0 & 0 & 0 & 0 \\ 0 & 0 & 0 & 0 & 0 & 1 & 0 & 1 & 0 \\ 0 & 0 & 1 & 0 & 0 & 0 & 1 & 0 & 0 \end{Bmatrix}$$

and, from Eq. (4·16),

$$\begin{Bmatrix} u,_{\xi} \\ u,_{\eta} \\ u,_{\zeta} \\ v,_{\xi} \\ v,_{\eta} \\ v,_{\zeta} \\ w,_{\xi} \\ w,_{\eta} \\ w,_{\zeta} \end{Bmatrix} = \begin{Bmatrix} \lfloor \bar{N} \rfloor,_{\xi} & 0 & 0 \\ \lfloor \bar{N} \rfloor,_{\eta} & 0 & 0 \\ \lfloor \bar{N} \rfloor,_{\zeta} & 0 & 0 \\ 0 & \lfloor \bar{N} \rfloor,_{\xi} & 0 \\ 0 & \lfloor \bar{N} \rfloor,_{\eta} & 0 \\ 0 & \lfloor \bar{N} \rfloor,_{\zeta} & 0 \\ 0 & 0 & \lfloor \bar{N} \rfloor,_{\xi} \\ 0 & 0 & \lfloor \bar{N} \rfloor,_{\eta} \\ 0 & 0 & \lfloor \bar{N} \rfloor,_{\zeta} \end{Bmatrix} \begin{Bmatrix} \{\bar{u}\} \\ \{\bar{v}\} \\ \{\bar{w}\} \end{Bmatrix} \tag{4·24}$$

Combination of Eqs. (4·21) through (4·24) yields the Eq. (4·5), i.e.,

$$\{\epsilon\} = [D] \{d\} \tag{4·25}$$

where

$$[D] = [SD] \begin{bmatrix} [J]^{-1} & 0 & 0 \\ 0 & [J]^{-1} & 0 \\ 0 & 0 & [J]^{-1} \end{bmatrix} \begin{bmatrix} \lfloor \bar{N} \rfloor,_\xi & 0 & 0 \\ \lfloor \bar{N} \rfloor,_\eta & 0 & 0 \\ \lfloor \bar{N} \rfloor,_\zeta & 0 & 0 \\ 0 & \lfloor \bar{N} \rfloor,_\xi & 0 \\ 0 & \lfloor \bar{N} \rfloor,_\eta & 0 \\ 0 & \lfloor \bar{N} \rfloor,_\zeta & 0 \\ 0 & 0 & \lfloor \bar{N} \rfloor,_\xi \\ 0 & 0 & \lfloor \bar{N} \rfloor,_\eta \\ 0 & 0 & \lfloor \bar{N} \rfloor,_\zeta \end{bmatrix}$$

Having established the matrix [D], the stiffness matrix for the element can be computed according to the relationship Eq. (4·6), i.e.,

$$[k] = \int [D]^T [E] [D] \, dV \tag{4·26}$$

where [E] is the elasticity matrix mentioned in Eq. (4·3). For isotropic material, matrix [E] has the form:

$$[E] = \frac{E}{(1+\nu)(1-2\nu)} \begin{bmatrix} (1-\nu) & \nu & \nu & 0 & 0 & 0 \\ \nu & (1-\nu) & \nu & 0 & 0 & 0 \\ \nu & \nu & (1-\nu) & 0 & 0 & 0 \\ 0 & 0 & 0 & \frac{(1-2\nu)}{2} & 0 & 0 \\ 0 & 0 & 0 & 0 & \frac{(1-2\nu)}{2} & 0 \\ 0 & 0 & 0 & 0 & 0 & \frac{(1-2\nu)}{2} \end{bmatrix} \tag{4·27}$$

The element region (volume) similar to the matrix [D] has to be transformed before integration using

$$dV = dxdydz = \det [J] \, d\xi d\eta d\zeta \qquad (4\cdot28)$$

Also, limits of integration become -1 and +1. More explicitly, we can write Eq. (4·26) as

$$[k] = \int_{-1}^{1} \int_{-1}^{1} \int_{-1}^{1} [D]^{T} [E][D] \det [J] \, d\xi d\eta d\zeta \qquad (4\cdot29)$$

where det [J] symbolizes the determinant of [J].

Clearly, exact integration of Eq. (4·29) will be in general a tedious if not impossible matter and numerical integration is a necessary part of the process. As shown in Eq. (4·29), the numerical integration is performed in every region in which each variance ranges from -1 to +1. The simplest performance of this is to use Gaussian points distributed on a regular basis, along the ξ, η, ζ directions. A three-point Gaussian quadrature formula is selected to evaluate the volume integration. The description of the Gaussian method appears in most finite element texts, Ref. [82], for instance.

The concept of using such element shape functions for establishing the isoparametric elements was first mentioned by Taig [83] and later generalized by Irons [84]. As shown in Reference [80], it has been proven that this well-defined 20-node isoparametric element satisfies the conformability requirements, i.e., requirements

for convergence and continuity.

The Three-Dimensional Special Isoparametric Element

A 3-D special element that embeds the appropriate stress singularity at the crack edge has been developed for the DT analysis. The special collapsed fifteen-node element which is modified from Tracey's [24] collapsed six node element enables a precise solution without requiring an extremely fine element mesh near the crack edge. The finite element model assembled is composed of these special wedge elements focused into crack front and regular isoparametric solid elements elsewhere. Fig. 9 demonstrates the modeling geometry. The elements nearest to the crack front have $r^{1/2}$ and r variations of displacement specified, while the adjacent elements allow the regularly linear and quadratic variations.

The special displacement element is formed by collapsing one face of a special twenty-node brick element (bounded by planes $\xi = 0,1$ and η, $\zeta = \pm 1$) and shown in Fig. 10. The interpolation parameters ξ, η, ζ are related to the physical coordinates x, y, z through a mapping of a brick in ζ, η, ξ space onto the physical triangular prism. The shape functions N_i of the special element are as follows:

$$N_i = \tfrac{1}{4}(1-\xi^{\frac{1}{2}})(1+\eta\eta_i)(1+\zeta\zeta_i)(-\sqrt{2}\xi^{\frac{1}{2}} + \eta\eta_i + \zeta\zeta_i - 1) \text{ for } i=1,\ldots,4$$

$$N_i = \tfrac{1}{4}\xi^{\frac{1}{2}}(1+\eta\eta_i)(1+\zeta\zeta_i) \, \{(2+\sqrt{2})\xi^{\frac{1}{2}} + \eta\eta_i + \zeta\zeta_i - 3 - \sqrt{2}\} \text{ for } i=5,\ldots,8$$

$$N_i = (\tfrac{\sqrt{2}}{2} + \tfrac{1}{2})\xi^{\frac{1}{2}}(1-\xi^{\frac{1}{2}})(1+\eta\eta_i)(1+\zeta\zeta_i) \text{ for } i=9,\ldots,12$$

$$N_i = \tfrac{1}{2}(1-\xi^{\frac{1}{2}})(1-\eta^2)(1+\zeta\zeta_i) \text{ for } i=13, 14$$

$$N_i = \tfrac{1}{2}\xi^{\frac{1}{2}}(1-\eta^2)(1+\zeta\zeta_i) \text{ for } i=15, 16$$

$$(4\cdot30)$$

$$N_i = \tfrac{1}{2}(1-\xi^{\frac{1}{2}})(1+\eta\eta_i)(1-\zeta^2) \text{ for } i=17, 18$$

$$N_i = \tfrac{1}{2}\xi^{\frac{1}{2}}(1+\eta\eta_i)(1-\zeta^2) \text{ for } i=19, 20$$

where N_i equals unity at node i and zero at all other nodes.

The special shape functions corresponding to that in the regular element are given in Eq. (4·18). The remaining development is quite similar to that in the previous section.

From Eqs. (4·30), it can be shown that

$$\sum_{i=1}^{20} N_i = 1$$

$$(4\cdot31)$$

Then the special elements satisfy the constant strain ahd rigid body motion conditions, i.e. the necessary conditions for convergence [80].

It will be seen that only the surface, where $\xi=1$, of the special element can be joined to a surface of the regular element (Fig. 9). The special shape functions on this surface, i.e. letting $\xi=1$ in Eq. (4·30), become

$$N_i = \tfrac{1}{4}(1+\eta\eta_i)(1+\zeta\zeta_i)(\eta\eta_i+\zeta\zeta_i-1), \text{ for } i=5,\ldots,8$$

$$N_i = \tfrac{1}{2}(1-\eta^2)(1+\zeta\zeta_i), \text{ for } i=15, 16,$$

$$N_i = \frac{1}{2}(1-\zeta^2)(1+\eta\eta_i), \text{ for } i=19, 20, \qquad (4\cdot32)$$

and

$$N_i = 0, \text{ for all remainder}$$

On the $\xi=1$ surface the regular shape functions, Eq. $(4\cdot18)$ also can be reduced to Eq. $(4\cdot32)$. This indicates both special and regular elements have the same shape functions on the surface at $\xi=1$. As mentioned previously, the well-defined regular shape functions satisfy the inter-element continuity requirements. Therefore, continuity exists between the $\xi=1$ surface of the special element and any adjacent surface of the regular element.

From Eq. $(4\cdot30)$, it is obvious that the same special shape functions exist either on the surfaces of $\eta=1$ and -1 or on the surfaces $\zeta=1$ and -1. If special isoparametric elements are assembled as shown in Fig. 9, it can be readily shown that continuity exists between any adjacent special elements [80].

As was stated above, the special element not only represents precisely the crack singularity, but also satisfies the conditions for convergence and inter-element continuity.

The Computation of the Stress Intensity Factor by Displacement Method

In Chapter II several methods have been introduced to evaluate the SIF in the finite element analysis. For a number of reasons,

only the displacement method may be considered in the 3-D elastic

analysis. First of all, the displacement method is applicable to a

3-D analysis. Secondly, the nodal displacements are the most accurate

quantities obtained from the displacement finite element scheme.

Finally, if it is necessary, the displacements can easily be checked

experimentally. This displacement method actually is only a form of

the crack opening displacement (COD) concept. As one of the fracture

criteria, the COD concept can be utilized to evaluate the stress in-

tensity factor K_I by considering the displacements at the nodes near

the crack tip. If the finite element solution for displacements

reflects the true nature of the singular behavior of stresses and

strains around the crack tip, then the COD would provide an accurate

estimation of the stress intensity factor. The finite element solu-

tion obtained by using a conventional model for crack problems

requires very small element sizes at the crack tip, relatively large

degrees of freedom and does not incorporate the correct displacement

behavior near the crack tip. Therefore, this method cannot be ex-

pected to provide an accurate estimation of the stress intensity

factor evaluated by the COD even at the nodal point closest to the

crack front. Thus, for a more meaningful and accurate estimation of

stress intensity factor through COD procedure, the singular nature of

the stresses and strains need to be incorporated or embedded in the

finite element procedure. All the methods using special singular

elements at the crack tip, including the special element developed in

this chapter, possess the true nature of the singular behavior of the

stresses and strains around the crack tip. Thus, the displacement procedure can be utilized very effectively to estimate the stress intensity factor from the present finite element displacement solution. From Equation (2·7) and using the displacement method, the stress intensity factors for two-dimensional problems can be expressed as

$$K_I = \frac{(2 + \sqrt{2})E}{4(1-\nu^2)} \sqrt{\frac{\pi}{r}} \ (2v_m - v_v) \tag{4·33}$$

where v_m and v_v are displacements at the mid-side and the vertex nodes, respectively. The mid-side and the vertex nodes locate at the distances $1/2\ r$ and r from the tip, respectively.

Kathiresan [48] has recently extended this procedure to three-dimensional problems. The stress intensity factor can be estimated by using the displacement of five nodes on the crack surface close to the crack front. It will vary, of course, quadratically within an element along the crack front. Details of this 3-D procedure, for convenience sake, is outlined in Appendix C. This procedure has been found to provide an accurate estimation of the SIF along a crack front [24, 48, 55].

CHAPTER V

VERIFICATION OF THE SPECIAL ISOPARAMETRIC ELEMENT

To demonstrate the superiority of the proposed special element, two fracture specimens were considered. In addition to using the special elements, the SIFs for these specimens were also calculated by a method of using distorted collapsed quadratic elements or by using distorted natural quadratic elements. A brief discussion of these distorted elements was given in Chapter II. Results based on different finite element schemes are presented for comparison.

Examination of the Idealized Compact Specimen

An idealized fracture toughness test specimen with uniform crack depth c was designed for the 3-D finite element analysis. As shown in Fig. 11.a, the thickness, half-width, and half-height were all taken equal to c. The loading condition was a uniformly distributed force of p per unit length through the thickness, applied at the crack ends and normal to them. Because of the double symmetry of the specimen and the loadings, only one quarter of the specimen was modelled as shown in Fig. 11. The global coordinates (x,y,z) are defined in this figure. The model consists of 499 nodes and 96 elements as shown in Fig. 11·b. Except in the internal region, the nodes were arranged at the following distance from the crack front,

$$r/c = 0.01, \ 0.02, \ 0.04, \ 0.1, \ 0.26, \ 0.30,$$

$$0.40, \ 0.60, \ 0.80, \ 1.00.$$

Away from the front, the nodal density across the half-thickness is decreased to four nodes along the crack end.

The stress intensity factors obtained from the finite element solutions are compared with the 2-D boundary collocation solution. For the 2-D version of the present model, Brown and Srawley [71] found that

$$K_{2D} = 7.20 \ pc^{-\frac{1}{2}} \tag{5.1}$$

The variation of SIF across the specimen is given in the plot K/K_{2D} vs. z/c as shown in Fig. 12. At the center ($z=0$) the SIF obtained from the method developed in Chapter IV is 4% over K_{2D}. At $z/c=0.5$, the free surface, K decreases to 0.75 K_{2D}. The present results have been compared with those obtained by Tracey [24] using his six-node special element. As shown in Fig. 12, the present results at the center are about 5% higher than those evaluated by Tracey, but 5% lower than at the free surface. The difference between these two results may be partially due to the fact that the present fifteen-node special element allows quadratic variations along the crack front, however, Tracey's element only permits linear variations along the crack front. It should be noted that the difference of mid-surface and planar K values in the present results is consistent with Kathiresan's [48] study. Based on a hybrid finite element analysis

of a center through-the-thickness crack plated, he found $^K/K_{2D}=1.05$ at the mid-surface. The center through-the-thickness cracked plate was also investigated by Ayres [85] and Sih et al. [86]. However, both Ayres' finite difference and Sih's finite element results suggest that the elevation of K over K_{2D} is about 10%. It is noteworthy that free surface effects remain a controversial issue with various investigators (for recent discussions, see Sih [102], Folias [87], and Beuthem and Koiter [88]). Therefore, results for the region near the free surface will not be discussed further.

In addition to using the special element, the SIF variation was also calculated by a method of using distorted natural quadratic elements. Fig. 12 shows that the SIFs estimated by the distorted elements are below those calculated from the present special element by about 1.5% over the entire specimen. Because of the absence of exact solutions to meaningful 3-D crack problems, at present it is very difficult to judge the accuracy of the numerical solutions mentioned here. To gage the possible error bound on the 3-D analysis, an artifical boundary constraint on all displacements in the z-direction equal to zero, is applied. The constrained 3-D model becomes, in point of fact, a plane strain model. The results are then 5% below K_{2D}. Hence, 5% is a candidate degree of error for the 3-D analysis using the present special element. A result some 6.5% below K_{2D} was found by using the distorted natural element. Tracey reported a result 6% below K_{2D} for a similarly constrained model.

As discussed in Chapter III, the specimen is neither vanishingly thin (plane stress) nor are the interior points far from the outer surfaces (plane strain), therefore the analysis has to consider the three-dimensional character of the stress field. The variation of the constraint factor $\alpha = \sigma_{zz}/\nu(\sigma_{xx}+\sigma_{yy})$ is considered in Fig. 13, where ν is Poisson's ratio and equals 0.3. For a plane strain state $\alpha=1$ and for plane stress $\alpha=0$. At $r/c=0.005$ from midplane to $z/c=0.4$, α is nearly constant at 0.90. Such proximity to the plane strain value is, of course, expected so near to the crack front [see, Eqs. (2.5) and (2.6) for details.]. From $z/c=0.4$ to the free surface, α drops rapidly. The midplane values of α at $r/c=0.04$, 0.02, 0.04, 0.1, and 0.26 are 0.86, 0.78, 0.69, 0.52, and 0.33, respectively. These data indicate the shift to a plane stress type field away from the front. The above stress state behavior is quite similar to those Tracey reported. However, in the region $0.4 \leq \frac{z}{c} \leq 0.5$, the constraint factor α of the present results is not like Tracey's results which converged to zero but disjointed randomly. Again, the free surface effect is not clear. No attempt will be made here to explain the difference between these two results at the region close to the free surface.

Test for Typical Double Torsion Specimen

To provide more information about the accuracy of the present special element, a DT specimen with a straight crack front was selected for the second model demonstration. The mesh design of the model is similar to the mesh shown in Figure 14, with the dimensions,

2t/W = 1, c/L = 1/2, and W/L = 1/5. The loading conditions are

shown in Figure 4, where an infinitesimal distance between the

applied loads ε is assumed in this 16 element model. In addition to

using the present special elements, the SIFs of this model were cal-

culated by a method using distorted collapsed quadratic elements, and

by a method of using distorted natural quadratic elements. Using the

form of the calibration equation determined in Chapter III, the

normalized SIF K* can be expressed conveniently in terms of

$$K^* = \frac{K_I}{K_{cal}} = \frac{K_I [8 t_c I_p (1-\nu)]^{1/2}}{P W_m} \tag{5.2}$$

where K_{cal} is the SIF directly calculated from the calibration equa-

tion (Eq. 3.14), and K_I is the SIF calculated from the finite element

method.

The finite elements results show that the SIF variation along

the straight crack front is almost linear. Only the maximum

normalized SIF's obtained from those three different finite elements

schemes are listed in Table 1.

The differences among the results listed in Table 1 are within

one half of one percent. The result using the presently developed

special elements is a little higher than others. The normalized SIF

results obtained from these three different schemes were also com-

pared with each other for the higher degree of freedom model (see

Figure 15). The results calculated using the special element scheme

Table 1. Maximum Normalized SIF for the
Idealized DT Specimen
(2t/W=1; c/L=1/2; W/L=1/5)

Type of Elements	K^*_{max}
Special elements (developed for the DT analysis)	1.657
Distorted collapsed quadratic elements	1.654
Distorted natural quadratic elements	1.648

are higher than the results obtained from using the distorted natural

quadratic element scheme by about 2% on the average.

CHAPTER VI

THE DOUBLE TORSION MODEL WITH A
QUARTER-ELLIPTICAL CRACK FRONT

A finite element analysis using the properties of 2124-T851 wrought aluminum alloy was selected to investigate the double torsion test numerically. The fracture toughness of this material had been studied by Outwater, Murphy, Kumble and Berry [10] using the double torsion test.

The previously cracked 2124-T851 specimens used in the above double torsion test have been examined to provide the information on the crack front geometry of double torsion specimens. The shape of the fatigue crack front is very close to a quarter-ellipse, only slightly different at the end region of major axis.

The quarter-elliptical or semi-elliptical models are commonly chosen models for the corner or surface cracks investigations [89, 90, 91]. It is reasonable and convenient therefore to use the quarter-elliptical corner models for the finite element double torsion test analysis.

Due to the symmetry of the DT test, only half of the DT specimen was considered in the finite element analysis. Five different specimen geometries have been selected to investigate the DT test. The dimensions of these five specimens are:

Specimen 1: $\frac{c}{L} = 1/6$, $\frac{2t}{W} = 1/3$, $\frac{b}{t} = 9/10$, $\frac{b}{c} = 0.45$

Specimen 2: $\frac{c}{L} = 1/3$, $\frac{2t}{W} = 1/3$, $\frac{b}{t} = 9/10$, $\frac{b}{c} = 0.225$

Specimen 3: $\frac{c}{L} = 1/2$, $\frac{2t}{W} = 1/3$, $\frac{b}{t} = 9/10$, $\frac{b}{c} = 0.15$

Specimen 4: $\frac{c}{L} = 1/6$, $\frac{2t}{W} = 1/3$, $\frac{b}{t} = 9/10$, $\frac{b}{c} = 0.225$

Specimen 5: $\frac{c}{L} = 1/3$, $\frac{2t}{W} = 1/6$, $\frac{b}{t} = 9/10$, $\frac{b}{c} = 0.1125$

where L is the length of the specimen, $\frac{W}{2}$ is the half width of the specimen, t is the thickness of the specimen, b is the minor axis of the quarter-elliptical crack, and c is the major axis of the crack.

As mentioned previously, along the surface of symmetry of the DT specimen, only Mode I fracture occurs. For convenience of the finite element analysis, an infinitesimally small distance between the applied loads ε was assumed (Fig. 4). The effect of the variation of the distance between the applied loads ε was considered separately. The effects of the side grooves have also been investigated and are discussed in a later chapter.

Five sets of the finite element mesh were designed to represent those five specimens as accurately as possible. The mesh was designed to represent to Specimen 2 as shown in Figure 15. Eight layers of quadratic elements make up the crack region. Each layer has four special wedge elements at the crack tip, the shortest being 1/9 of the minor axis of the quarter-elliptical crack. Ten layers of quadratic

elements comprise the remaining part of the specimen. This typical higher degree of freedom model consists of 195 elements and 1115 nodes. Figure 16 shows details of the crack area mesh.

The results calculated from Specimens 1, 2, and 3 with the loading conditions, $\varepsilon=0$, show the influence of the variation of the ellipse major axis c in Figure 17. Figure 17 shows a plot of the normalized SIF K* versus the elliptical angle ϕ for aspect ratios $(\frac{b}{c})$, 01.5, 0.225 and 0.45. The corresponding variation of the normalized SIF, due to increasing the distance between the applied loads ε, is shown in Figure 18 for $\frac{2\varepsilon}{W} = 0$, 0.0333, 0.1167 and 0.2 As seen in Figure 18, the loading location factor ε affects the SIF significantly in the region adjacent to the anchorage of the loads. Away from the location of the loads, the normalized SIF is almost independent of the variation of the loading location factor ε. As noted in Fig. 18, it is believedthat the high normalized SIF for the elliptical angle approaching $\frac{\pi}{2}$ decreases to a small value as long as the loading location factor ε greater than zero. Therefore, the maximum normalized SIF K_{max} for Specimens 1, 2, and 3 with the loading location factor $\varepsilon > 0$ is approximately equal to unity (see Figure 17). The local maxima at $\frac{\pi}{2}$ result from assuming $\varepsilon=0$ and should, therefore, be ignored.

The thickness effect may be examined in part from the results with Specimens 2 and 5, as shown in Figure 19. The maximum SIF results shown in Figure 19 are not sensitive to the thickness variation $(\frac{2t}{W})$, from 1/3 to 1/6 as well as b/c changes from 0.225 to

0.1125. Almost identical stress intensity factor results have been obtained from Specimens 2 and 4. Because of similarity, the results for Specimen 4 are not presented here. However, such findings suggest that the length effect (end effect) of the test specimen can be viewed as negligible as long as the specimen length is greater than triple the crack length along the major axis.

From the above finite element analyses, which have been performed for most typical currently utilized test specimen geometries as well as the crack geometries, the maximum normalized SIF's are seen to be almost equal to unity for a true four point bending ($\varepsilon > 0$) DT test. As mentioned before, the free surface effects are still a controversial issue with various investigators. However, Sih [102] predicted that the SIF approaches zero at the point where the crack intersects the free surface and that a thin boundary layer is expected at the free surface across which the SIF decreases rapidly. If Sih's prediction is true, the present results may be overestimated in regions which approach the free surface. This overestimation makes the maximum normalized SIF for Specimen 1 closer to 1. However, the DT crack aspect ratios for b/c used in those tests [10] are within the range from 0.1125 to 0.30. The results for Specimen 1 (b/c $\approx$ 0.45) should thus not be used in comparison with the experimental results.

It is reasonably assumed that fracture commences in the DT specimen whenever the maximum stress intensity factor reaches a critical value, i.e. critical stress intensity factor [72]. From the present finite element analysis, the critical stress intensity factor

(maximum stress intensity factor) was found to be almost equal to the measured critical stress intensity factor directly calculated from the calibration equation, Equation (3·14), i.e. $K^*_{max} \doteq 1$. It has also been noted from previous experimental investigations that perfectly flat fracture surfaces are invariably present in DT specimens. The appearance of the flat fracture surface further suggests that the maximum SIF becomes K_{IC} as a critical loading is applied. It should be noted that the SIF variations shown in Figs. 17, 18, and 19 are not only an essential part in providing an in-depth understanding of the double torsion K_{IC} test but also yield useful information in predicting the crack front profile and the crack velocity in the subcritical crack growth test {67}.

The corresponding elastic stress fields were also calculated for the quarter-elliptical cracked DT specimens. The normalized stress components along the lower line of symmetry (A-A') is shown in Figure 20 for Specimen 2. The normalized stress components σ^*_{ij} are defined as

$$\sigma_{ij}^* = \frac{\sigma_{ij}}{\tau_{max}} = \frac{\sigma_{ij}}{\dfrac{PW_m}{2\beta Wt^2}} \tag{6·1}$$

where σ_{ij} are the calculated stress components, τ_{max} is the maximum shear stress developed in the equivalent rectangular torsion bar with a thickness-to-width ratio $\frac{2t}{W}$ by a twisting moment (torque) $\frac{PW_m}{4}$, and β, a numerical factor, euqal to 0.267 for $\frac{2t}{W} = 1/3$ [92]. Fig. 20

also shows that the stress component σ_{zz} (in the thickness direction) converges very rapidly to zero, being negligible beyond a distance, $\frac{y}{L-c} = 0.1$, from the crack front. For an uncracked body, of course, this component is zero on free surfaces. Thus, the region of significant departure from the free surface condition is highly localized. In this localized region, it is also seen that σ_{zz} does not directly decrease to zero, but falls to a negative value and then increases to zero. This depressed behavior may be due to the effect of the free surface or curved crack front. However, such effects are not yet fully resolved.

The variation of the effective stress σ_e normalized as before [see Eq. (6·1)] is given in Fig. 21 for Specimen 1, 2, and 3. As shown in Appendix E, the effective stress is a measurement of the yield surface of material and defined as

$$\sigma_e = \frac{1}{\sqrt{2}} \, [(\sigma_{xx}-\sigma_{yy})^2 + (\sigma_{yy}-\sigma_{zz})^2 + (\sigma_{zz}-\sigma_{xx})^2 + \qquad (6·2)$$
$$6(\sigma_{xy}^2 + \sigma_{yz}^2 + \sigma_{zx}^2)]^{1/2}$$

From the information in Fig. 21, near the crack front A, the plastic zone size of Specimen 2 may be expected to be larger than that for Specimen 3 but smaller than that of Specimen 1. A detailed plastic zone analysis is presented in Chapter IX.

CHAPTER VII

VERIFICATION OF THE CALIBRATION EQUATION

The calibration equation of the DT test (Eq. 3·14) results from an approximate treatment involving the principle of conservation of energy* and based on the assumption of a straight crack front orthogonal to the plane of the specimen (Fig. 5). Discrepancies occur due to the fact that the DT test incurs a corner crack, and also due to the fact that the equivalent torsion bars are not rigidly fixed at their ends but supported by an elastic hinge. To verify the calibration equation, the DT specimen with a straight crack front has been studied by the same finite element technique used in the previous Chapter.

In the straight crack front DT analysis, no constraints were assumed on the crack surface. This assumption yields a negative SIF and material overlap in the upper half of the specimen. Although, this material overlap can never occur physically, the assumption was made mainly to be consistent with the conditions used in deriving the calibration equation.

Several results obtained from using this assumption was compared with the results obtained from using a non-material overlap condition.

---

*The elastic energy of the double torsion specimen which is beyond the crack front was assumed as zero for the calibration equation derivation.

The former results are higher than the latter results by approximately 3%.

The results evaluated from the straight crack front finite element models (hereafter this model will be called the idealized DT model to distinguish from the DT model with a corner crack) were also compared with the results of corner crack specimens. A generalized DT calibration equation was made for both the corner and the straight crack front specimens.

A finite element model with a relatively few degrees of freedom could be made of the idealized DT specimen due to the fact that the crack front was assumed straight. These relatively coarse mesh models can be handled by the computer without the aid of out-of-core storage accessories. A good deal of computer time is thus saved due to the use of these coarse mesh models.

Reliable accuracy of the relatively coarse mesh models was achieved by selecting an optimum size of special elements. A sixteen element idealized DT finite element model with the dimensions, $\frac{2t}{W} = 1$, $c/L = 1/2$, and $W/L = 1/5$ was studied by varying the special element size parameter, $\frac{2h}{W}$, from 0.1 to 0.4 (h is the characteristic length of the triangle cut from the special wedge elements, and c is the crack length, b becomes infinity). Proof that the optimum special element size is about 10% of the crack length has been provided by Tong and Pian [93], however this may not be applied to the idealized DT finite element analysis. In this idealized DT model ($\frac{2t}{W} = 1$, $\frac{c}{L} = 1/2$, and $\frac{W}{L} = 1/5$), 10% of the crack length ($\frac{h}{c} = 1/10$)

is equivalent to half of the thickness. This is obviously too large.

Using a refined mesh model that contains 68 elements, it was found that the maximum SIF values approximately equal 1.66 for various $\frac{2h}{W}$, from 0.05 to 0.15. This value is considered more accurate than results obtained from the 16-element models. Comparing this value with the results from the relatively coarse mesh models, it is found the $\frac{2h}{W} = 0.2$ is indeed the "optimum" special element size. This analysis is summarized in Table 2.

Four different finite element models, with $\varepsilon=0$, have been used to analyze the idealized DT specimens. The dimensions for these four models are:

(1) $\frac{2t}{W} = 1$, $\frac{W}{L} = 1/5$, $\frac{c}{L}$ varying from 1/10 to 9/10,

(2) $\frac{2t}{W} = 1$, $\frac{W}{L} = 1/3$, $\frac{c}{L}$ varying from 1/6 to 5/6,

(3) $\frac{2t}{W} = 1/2$, $\frac{W}{L} = 1/3$, $\frac{c}{L}$ varying from 1/6 to 5/6,

and

(4) $\frac{2t}{W} = 1/3$, $\frac{W}{L} = 1/2$, $\frac{c}{L}$ varying from 1/6 to 5/6

A typical idealized DT model is shown in Figure 14 with the dimensions, $\frac{2t}{W} = 1/3$, $\frac{W}{L} = 1/2$, and $\frac{c}{L} = 1/3$.

To verify the calibration equation, only the maximum SIF's are of interest, the K^*_{max} results for the four models are shown in Fig. 22. These K^*_{max} values are almost independent of the crack length over a substantial range. In Fig. 22, the solid lines represent a maximum

Table 2. The Maximum Normalized SIF for the
Optimum Special Element Size Analysis

Special Element Size $2h/W$	Max. Normalized SIF of 16 Element Model K^*_{max}
0.1	1.789
0.2	1.657
0.3	1.638
0.4	1.612
Normalized SIF K^*_{max} of Refined Mesh Model	1.66

of 5% variation in K^*_{max}. Comparing Model 2 with Model 3, it can be seen that the ranges which provide nearly constant K^*_{max} value for each model are nearly independent of the ratio $\frac{2t}{W}$. It also can be found that the range of $\frac{c}{L}$ is highly dependent on the ratio $\frac{W}{L}$. Based on the results shown in Fig. 22, for the K_{max} to be within 5% of the "crack length independent" K_{max} values, the following conditions need to be satisfied.

For crack length:

$$\frac{c}{L} \geq 0.35 \times \frac{W}{L} , \text{ or } c \geq 0.35W \tag{7·1}$$

and for ligament length:

$$1 - \frac{c}{L} \geq 0.65 \times \frac{W}{L} , \text{ or } L-c \geq 0.65W \tag{7·2}$$

The K^*_{max} is also shown to be increased as $\frac{2t}{W}$ is decreased. It is reasonble to surmise that this is due to the fact that the deformation energy of the elastic support increases as $\frac{2t}{W}$ decreases [94]. Then the calibration equation can be modified as

$$K_I = A \, P \, W_m \, [\frac{1}{8t_c I_p (1-\nu)}]^{1/2} \tag{7·3}$$

where A is the modification factor. A is seen to be approximately equal to $1.65+0.14 \ln(\frac{W}{2t})$ for a reasonable range of the width-to-thickness ratio, $\frac{W}{2t}$, for the idealized DT specimen and to 1.0 for the

corner crack DT specimen.

Equation (7·3) would appear to have sufficient flexibility and accuracy in form for describing the nature of the DT test. It is, of course, similar to the well known generalized form

$$K_I = B \sigma \sqrt{c} \qquad\qquad (7·4)$$

which represents the problem of an infinite solid containing a crack under unaxial tension. Where the crack is a central crack through the infinite solid with 2c crack length, the factor B equals $\sqrt{\pi}$. For an embedded elliptical crack, B becomes [72]

$$\frac{\sqrt{\pi\frac{b}{c}}}{\Phi} \quad \{\frac{b^2}{c^2} \cos^2\phi + \sin^2\phi\}^{1/4}$$

where c is the major axis and b is the minor axis of the ellipse, Φ is an elliptical integral, and ϕ is an elliptical angle.

It is worth noting that Srawley and Gross [39] have used boundary collocation analysis to modify the calibration equation of the double cantilever beam specimen which is also derived from the principle of conservation of energy. This is essentially similar to what has been done here for the DT specimen.

Recently, a finite element analysis which, in some respects, is similar to the present idealized DT analysis, was reported by Trantina [30]. In addition to consideration of the idealized DT model (the straight crack front is perpendicular to the specimen

surface), Trantina also considered several other configurations, for which the crack fronts were orientated 30° and 45° to the specimen surface. As quoted from Trantina, these orientated crack front models were tried to simulate the lower half of the penetrated specimen.* For the upper half of the penetrated specimens, the crack fronts are really too skew to simulate by using the finite element scheme. If the dissimilarity of the crack front in the upper part of the specimen can be ignored, Trantina provided very useful information on the penetrated specimen. Trantina found that if the straight crack fronts are orientated between 30° and 40°, the K^*_{max} values are approximately reduced to unity. This finding gives a theoretical explanation why the valid K_{IC} can be obtained from a penetrated specimen.

Trantina used 176 <u>regular</u> constant strain elements to build his models and the displacement method to estimate the SIFs. The dimensions used were $\frac{2t}{W} = \frac{1}{5}$, $\frac{W}{L} = \frac{1}{2}$, and $\frac{c}{L}$ varying from 0.2 to 0.8. For the idealized DT specimen with $\frac{W}{2t} = 5$, the K^*_{max} estimated by Trantina and by Eq. (7·3) are equal to 2.0 and 1.88, respectively. The difference between 2.0 and 1.88, about 6%, may be due to the use of different finite element schemes. Trantina also showed that the K^*_{max} is nearly independent of crack length over a certain range for the crack front orientated specimen. He concluded that for a valid K_{IC} calibration, the crack length, c, and ligament length, L-c, must

---

*For some ceramic materials, penetrated crack fronts are often observed in relatively thin specimens.

be greater than 0.55W and 0.65W, respectively. Comparing this with the present Eqs. (7·1) and (7·2), Trantina's solution is consistent with the ligament length requirement, however, it is too conservative for the crack length requirement. In general, there is good agreement between Trantina and the present results especially considering differences in the models, crack shapes, geometries, and the finite element schemes. It should again be noted that the use of regular elements at the crack front is not normally desirable if high accuracy information is sought on stress intensification patterns.

CHAPTER VIII

THE GROOVE EFFECT AND THE DOUBLE TORSION SPECIMEN

When using double torsion specimens, it often happens that the crack path deviates from the line of symmetry. It is also possible that shear lips might occur at the fracture surface. In order to ensure a symmetric cracking path and obtain a flat fracture surface, a side grooved specimen is normally used in the DT test. The effect of the side grooving on measurement of the stress intensity factor will be discussed in this chapter.

The straight crack front finite element model used in the previous chapter was modified to analyze the groove effect. In order to maintain a small number of elements to represent the high stress concentration at the groove edge and near to the crack region, special elements are also used in that part of groove region which is close to the interception point of the crack front. Regions of the groove away from the crack front use conventional elements to compensate for the overestimate of stress concentration by special elements.

The grooved DT specimens usually contain two side grooves, one along the upper face (upper groove) and the other along the lower face (lower groove) as shown in Figure 4. The effects of the upper and lower grooves were calculated separately. To minimize the end effect, the geometry used in this analysis is $\frac{2t}{W} = 1$, $\frac{c}{L} = 1/2$, $\frac{W}{L} = 1/5$, and $\frac{t_c}{t} = 9/10$ for each groove analysis. The effect of the variation of

the groove angle ψ was also considered. The calibration equation (Eq. 3·14) in which t_c is the only one parameter to account the groove effect, does not, of course, reflect the groove angle variation.

The numerical results using the above finite element model associated with a loading condition, $\varepsilon = 0$, are summarized in Table 3.

From Figure 22, the maximum normalized SIF for the present geometry without groove effects is 1.657. If the calibration equation takes the groove effect fully into account, the maximum normalized SIF still equals 1.657 for grooved specimens. Based on the present finite element results, the calibration equation precisely describes the groove effect for the upper grooved type specimens, but may provide an overestimate of about 10% for the lower grooved type specimens. In other words, the lower groove decreases the maximum stress intensity factor for a DT specimen with a straight crack front. For the specimens with a quarter-elliptical crack front, and the minor to major axis ratio b/c less than 0.3, the locations of these maximum stress intensity factors are away from the lower groove region there, thus the groove effect can be viewed as negligible (see Figs. 17, 18, and 19). As mentioned previously, a specimen with b/c greater than 0.3 is rarely observed with the DT test and is also not recommended from the present results.

Table 3 also shows that the maximum stress intensity factor increases as the groove angle ψ is increased. For a groove angle ψ variation from $30°$ to $90°$, the maximum stress intensity factors increase 0.6% and 2.0% for the upper grooved and lower grooved specimens,

Table 3. The Maximum Normalized SIF
for the Groove Effect Analysis

Groove Angle ψ°	Maximum Normalized SIF K_{max}* Values	
	Upper Grooved Specimen	Lower Grooved Specimen
30	1.650	1.415
45	1.654	1.423
60	1.655	1.431
90	1.660	1.448

NOTE: The normalized stress intensity factor
for ungrooved specimen is 1.657.

respectively.

It should be noted that the groove effect may depend upon the sharpness of the groove, the crack and the groove geometries, as well as the loading conditions. The present analysis only provides pre- liminary results for this problem. Furthermore, the present results only describe the groove effect on SIF evaluations. They may not directly explain the fact that with the aid of grooves, the flat fracture growth surface can be formed for a relatively thin specimen. As discussed in the second section of Chapter III, the formation of the flat fracture growth surface is a much more complex matter.

CHAPTER IX

CRACK FRONT PLASTIC ZONE ANALYSIS

The preceding finite element analysis is, of course, based on the LEFM. The SIF is a parameter which characterizes the singularity of stress field in the immediate vicinity of the crack tip. However, for real materials, the stress is frequently bounded by the plastic yielding in the region of elevated stress. If the zone of plastic flow is small, the stress distribution, by and large, will not be seriously disturbed. Irwin [33] pointed out that as long as this plastic zone is small compared with crack length, the linear elastic fracture mechanics can be used with reasonable accuracy. A DT plastic zone analysis as well as related topics will be presented in this chapter.

Crack Size Requirements

From the above discussions, it is evident that the crack size should be a multiple of the size of the plastic zone. If the von Mises criterion is used, the size of the plastic zone (r_p) of Mode I crack can be roughly determined from the elastic asymptotic solution, Eq. (2·1), thus [72]:

$$\text{Plane stress:} \quad r_p(\theta) = \frac{1}{4\pi}\left(\frac{K}{\sigma_y}\right)^2 [1 + \frac{3}{2}\sin^2\theta + \cos\theta] \quad (9\cdot1)$$

Plane strain: $r_p(\theta) = \frac{1}{4\pi} (\frac{K}{\sigma_y})^2 [\frac{3}{2} \sin^2 \theta + (1-2\nu)^2 (1+\cos\theta)]$ (9·2)

where θ is defined in Fig. 2. The plastic zone in plane strain is appreciably smaller than plane stress plastic zone. According to Eq. (9·2), the farthest point of plastic boundary is at $\theta=90^\circ$. For $\theta=90^\circ$ and $\nu=0.3125$, the plane strain plastic zone becomes

$$r_p = 0.13 (\frac{K}{\sigma_y})^2 \qquad\qquad (9·3)$$

Comparing the above equation with Eq. (3·15); it is seen that the recommended ASTM crack size requirement is about 19 times the plane strain plastic zone size. The requirement of Eq. (3·15) perhaps may hold for all specimens deduced from the LEFM concept. An analysis which shows this requirement is suitable to the DT test will be presented in the next section.

In order to apply Eq. (3·15) to the DT test, an effective (or equivalent) crack size which characterizes a crack with a curved front needs to be found. Following the idea revealed in Eq. (3·10), the effective crack length c_e may be expressed as

$$c_e = \frac{A_c}{t_c} \qquad\qquad (9·4)$$

where A_c is the crack surface and may be given as

$$A_c = \begin{cases} \dfrac{\pi}{4}\, bc & \text{for unpenetrated specimen} \\[2mm] at_c + \dfrac{\pi}{4}\,(c-a)\,t_c & \text{for penetrated specimen} \end{cases} \tag{9.5}$$

where a, b, c, and t_c are defined in Fig. 5. Substituting Eq. (9.5) into Eq. (9.4) the effective crack size becomes

$$c_e = \begin{cases} \dfrac{\pi bc}{4 t_c} & \text{for unpenetrated specimen} \\[2mm] \dfrac{\pi}{4}(c+0.27a) & \text{for penetrated specimen} \end{cases} \tag{9.6}$$

Similarly from Eq. (3.15), a requirement for the effective crack size is

$$c_e \geq 2.5 \left(\frac{K_{IC}}{\sigma_y}\right)^2 \tag{9.7}$$

Also, through the relation of implied in Eq. (9.6) the range of approximately constant K_{max} value which has been developed for the idealized DT specimen may be extended to the curved crack front specimen. Thus, Eqs. (7.1) and (7.2) become

$$c_e \geq 0.35W \tag{9.8}$$

and

$$L - c_e \geq 0.65\ W \tag{9.9}$$

Eqs. (9·8) and (9·9) imply that the range of approximately constant K_{max} depends on the ratio of width-to-length, $\frac{W}{L}$. For instance, if the range of near constant K_{max} is required over than 50% of the specimen length, the width-to-length ratio should be less than 1/2.

Compared with the rigorous ASTM requirements, the DT size requirements which were established in Eqs. (9·7) through (9·9) and Eq. (3·17) apparently are much more readily achievable. It should be noted that the crack size criterion for the DT test developed here has been based partly upon the profile of the K_{max} variation over the specimen length rather than solely upon plastic zone size.

An Equivalent 2-D Model Used in Plastic Zone Analysis

To assess the validity of the DT crack size requirement, i.e. Eq. (9·7), a crack front plastic zone analysis will be performed. Based on the following reasons, a 2–D finite element model may be used for the plastic zone analysis.

1. As has been noted earlier, the crack front plastic zone size is proportional to $(\frac{K}{\sigma_y})^2$. It is reasonably assumed, therefore, that for a particular material, the variation of plastic zone size along the curved crack front, will depend on the local SIF and the curvature of crack front. Furthermore, if the radius of curvature of the curved crack front is larger compared with the related specimen dimension, the local plastic zone size may only be considered dependent on the local magnitude of SIF.

2. From the earlier elastic analysis (Chapter VI), the maximum SIF occurs at the elliptical angle between $\frac{\pi}{4}$ and $\frac{\pi}{2}$ for a DT crack

aspect ratio, (^{b}/c), less than 0.225 (see, Fig. 17). For this small aspect ratio ($\frac{b}{c} \leq 0.225$), the radius of curvature of the elliptical angle between $^\pi/4$ and $^\pi/2$ is much larger than the effective crack size. In this region, the local plastic zone size then, can be assumed dependent on the local magnitude of SIF only.

3. Since only the maximum plastic zone need be estimated, the cross-section containing the maximum SIF need only be considered.

Thus, an equivalent plane strain model can be designed to represent a cross-section of the DT specimen which contains the elliptical angle of the crack between $^\pi/4$ and $^\pi/2$ (see Fig. 23).

The 2124-T851 wrought aluminum alloy was again selected for the plastic zone analysis. The material properties are listed as follows:

Fracture Toughness (K_{IC}): 28.4 ksi$\sqrt{in}$ (31.2 MPa$\sqrt{m}$)

Yield Stress (σ_y): 67.0 ksi (462.0 MPa)

Young's modulus (E): 10.5×10^3 ksi (72.4×10^3 MPa)

Poisson's ratio (ν): 0.3125

From the above data and the calibration equation of the DT test, a critical load (P_c) of 3,488.8 lbs. (15,518.2 Newtons) can be calculated for a specimen with a cross-section, $\frac{2t}{W} = \frac{1}{3}$ and $W = W_m = 3.0$ in. (7.62 cm.). This cross-section is consistent with the geometry of Specimens 1, 2, 3, and 4 in Chapter VI.

It is also to be noted that because of the linear nature of
the elastic results and the small variation of Poisson's ratio, with
same specimen dimensions, the deflections plotted in Fig. 23 can be
approximately converted to that of other elastic materials by
utilizing a factor of (^{E} $^{K_{IC}}/E_{A\ell}K_{A\ell}$), where the E and K_{IC} are the
Young's modulus and fracture toughness, respectively, of the material
to be converted, and $E_{A\ell}$ and $K_{A\ell}$ are for the 2124-T851 aluminum alloy.

Analytical Procedure and Results

Crack Tip Stress and Strain Field

In the case of small scale yielding, the asymptotic singularity
was found by Rice and Rosengren [95] and Hutchinson [96]. Their
analysis determined the crack tip stress and strain singularities for
materials having a power law relationship between effective stress
and effective strain. In this case, the near crack tip stress σ_{ij}
and strain ε_{ij} variations are given by

$$\sigma_{ij} \rightarrow r^{-n/(1+n)} \sigma_{ij}(\theta)$$

$$\varepsilon_{ij} \rightarrow r^{-1/(1+n)} \varepsilon_{ij}(\theta)$$

(9·10)

where n is the power hardening coefficient. For n=1, Eq. (9·10)
reduces to the linear elastic case and is in agreement with the
inverse-square-root singularity equations given in Chapter II. For
elastic-perfectly plastic materials, n equals zero and Eq. (9·10)
degenerates to

$$\sigma_{ij} \rightarrow r^0 \, \sigma_{ij}(\theta) \tag{9.11}$$

$$\epsilon_{ij} \rightarrow r^{-1} \, \epsilon_{ij}(\theta) \tag{9.12}$$

The functions $\sigma_{ij}(\theta)$ and $\epsilon_{ij}(\theta)$ are similar to the elastic solutions and are determined by the solution of equilibrium, compatibility and constitutive equations subject to a traction free boundary condition.

Finite Element Model

For a conservative and simplified approach of the plastic zone analysis, the 2124-T851 aluminum alloy was treated as an elastic-perfectly plastic material. The distorted collapsed quadratic elements were selected to model the near crack tip region.

If the collapsed nodes (at the crack tip) of the distorted collapsed element are constrained to have the same displacements, the element can be shown embodying the $(1/\sqrt{r})$ singularity of elastic fracture mechanics. However, if the collapsed nodes are left free (sliding node) to displace independently of each other, the inverse singularity of Eq. (9.12) can be obtained [28]. The finite element analysis concerned used these distorted elements adjacent to the crack tip and hence guarantees the results having reliable accuracy, given the previously stated assumptions.

The finite element mesh of the equivalent 2-D model is shown in Fig. 24. It contains 4 distorted collapsed quadratic elements around the crack front and 50 regular quadratic elements elsewhere.

The 3-D elastic results of 2124-T851 aluminum alloy were utilized to determine the loading condition for the equivalent 2-D model. Under the critical loading, deflections along the upper symmetric line (line B-B' in Fig. 23) of Specimens 1, 2, and 3 are plotted in Fig. 23. If Specimen 2 is chosen for the plastic zone analysis, as shown in Fig. 17, the maximum SIF occurs at $\phi = 55°$ or $y/L = 0.19$. Therefore, a 2-D model which represents the cross-section located at $y/L = 0.19$ can be constructed for this typical plastic zone analysis.

The relative deflection of the upper symmetric line to the outer edge locations (line C-C' in Fig. 23) may be superimposed on the equivalent 2-D model as the loading condition. In the cross-section considered ($y/L = 0.19$), the relative deflection, d, as shown in Fig. 23, equals 0.022 in. (0.056 cm) for Specimen 2. The dashed line shown in Fig. 23 represents the deflection along the outer edge locations for Specimen 2.

The 2-D model based on the above concept may now be formulated. The dimensions of the model are depicted in Fig. 24. The equivalent crack length equals 0.368 in. (0.935 cm) at the cross-section of $y/L = 0.19$. As discussed previously, the equivalent loading condition is a displacement (d) equal to 0.22 in. (0.56 cm) loaded at the upper symmetric line. The complexity of the above model formulation is due to the attempt of resolving a 3-D problem using 2-D viewpoints and is clearly unavoidable.

Elastic Verification of the Equivalent Model

The above model was first examined by a plane strain elastic analysis. The plane strain elastic results were compared with the 3-D results. This comparison provided essential data to evaluate the accuracy of using the equivalent plane strain model to simulating the 3-D DT problem.

The SIFs of the plane model were estimated by using the relationship of Eq. (4·33), the COD criterion, and by calculating the J-integral over several paths surrounding the crack tip. It is to be noted that the crack size of this equivalent 2-D model is somewhat deep and beyond the limit prescribed by the ASTM bend specimen calibration (see Fig. 7).

The J-integral as introduced in Chapter II can be utilized over range of conditions from essentially elastic to fully plastic. Begley and Landes [97] have been shown that the magnitude of J can be used as a fracture criterion for cracked bodies. The J-integral evaluated from the elastic solution is thus not only used for verification of the equivalent model, but also for providing a numerical measure of the plastic zone effect. The definition and computation procedure of J-integral is described in Appendix D.

The results are summarized in Table 4, where K_{3D} is the maximum SIF of Specimen 2 and equals 27.3 ksi$\sqrt{in}$ (30.0 MPa$\sqrt{m}$) for 2124-T851 aluminum alloy, and Paths 1, 2, and 3 are defined in Fig. 24. As shown in the table, the 2-D model is in good agreement with the simulated DT specimen, the extent of the agreement depending upon the

TABLE 4

STRESS INTENSITY FACTOR OF THE EQUIVALENT
PLANE STRAIN MODEL

K-estimated method		J_c, ft-lb$_f$/in^2 (J/m^2)	K_C^{**}, ksi $\sqrt{in}$ (MPa $\sqrt{m}$)	K_{C}/K_{3D}^{***}
COD		DNA*	27.08 (29.76)	0.99
J–Integral	Path 1	6.46 (5.65E-3)	30.04 (33.01)	1.10
	Path 2	6.34 (5.55E-3)	29.76 (32.71)	1.09
	Path 3	7.43 (6.50E-3)	32.22 (35.41)	1.18

*   Does Not Apply.

** $K_C = \left(\dfrac{JE}{1-\nu^2}\right)^{\frac{1}{2}}$

*** $K_{3D} = 27.3$ ksi $\sqrt{in}$ (30.0 MPa$\sqrt{m}$)

approach taken. The SIF calculated from the COD method is within

1% of the 3-D critical value. This 2-D SIF value is particularly

significant, since the 3-D critical value is also calculated from the

COD method. The J-integral values are reasonably path independent.

However, a significant variation in J occurs for Path 3. This path

is through the single loading point and partially on the outer boun-

dary of the specimen. The variation in J on this path may well

reflect the inability of the 2-D model to adequately represent the

$1/r$ stress and strain singularities at the loading point [92].

Furthermore, there will also be small error in calculating the stresses

on traction free boundaries. These errors are to be expected with

the displacement finite element model. From the above study, the 2-D

equivalent model may be considered to be accurate to within 10% in

simulating the DT test arrangement.

Results for Plastic Zone and J-Integral

In plastic zone analysis, the equivalent 2-D plane strain

model was examined by mean of a modified version of a finite element

computer program developed by Westinghouse Electric Corporation [29].

The elastic-plastic stress-strain relations used in this program are

based upon the small deformation incremental theory of plasticity,

using the von Mises yield criteria, and the associated flow rule, the

Prandtl-Reuss equations. The approach for the elastic-plastic finite

element analysis uses the method of successive elastic approximations,

or the initial strain method. A discussion of the theory and the

approach of the finite element analysis may be found in Appendix E or

Reference [98].

From the elastic-perfectly plastic finite element analysis, the calculated relative plastic zones are shown in Fig. 24 for deflection loadings equal to 0.011" (0.028 cm) and 0.022" (0.056 cm). As shown in the figure, the maximum plastic zone size near the crack front for the critical deflection loading condition is approximately 0.018" (0.46 cm) in radius. This plastic zone size equivalent to 0.10 $(\frac{K}{\sigma_y})^2$ which represents 80% of the value determined from Eq. (9.3). Compared with the refined estimates of Larsson and Carlsson [99] for the plastic zone size in corresponding standard ASTM specimens, the above results is indeed of a highly appropriate magnitude. They used a rigorous finite element analysis and show that the maximum plastic zone sizes of the ASTM specimens are between 0.11 $(^K/\sigma_y)^2$ and 0.14 $(^K/\sigma_y)^2$. From this comparison, it can be deduced that if Eq. (9.7), the crack size requirement for the small scale yielding criterion, is appropriate for the ASTM standard test, this equation is also suitable for the DT test to satisfy the small scale yielding criterion.

In order to present a numerical estimate of the scale of the plasticity effects in the small scale yielding condition, a J-integral evaluation based on the plane strain elastic-perfectly plastic results is also provided. The effect of the plasticity on the J-integral is shown in Table 5. The calculated values of J_p are normalized by the elastically calculated J_e values which were also reported in Table 4. The deviation from 1.0 of the ratio $^{J_p}/J_e$ is a measure of the effect of plasticity. The maximum deviation of

TABLE 5

J-INTEGRAL OF THE EQUIVALENT PLANE STRAIN MODEL

J-Integral, ft-lb/in^2 (J/m^2)		
Path	Elastic (J_e)	Elastic-Perfectly Plastic (J_p)	J_p/J_e
1	6.46 (5.65 E-3)	5.98 (5.23 E-3)	0.93
2	6.34 (5.55 E-3)	6.17 (5.40 E-3)	0.97
3	7.43 (6.50 E-3)	6.68 (5.85 E-3)	0.90

$(^J P/J_e)$ in Table 5 is 10% for Path 3. As mentioned in the previously subsection, the value calculated from Path 3 must be neglected. If only Paths 1 and 2 are considered, the average deviation is 5%. However, this 5% deviation in J-integral is equivalent to a 2.5% plasticity effect in the SIF. It should be noted that this 2.5% plasticity effect is evaluated in a cross-section where the crack front plastic zone size is considered to be the largest. In other words, the plastic effect should be much less than 2.5%, if the whole specimen is considered. It is also to be noted that the present finite element analysis is fairly conservative due to neglect of the strain hardening effect. An analysis similar to the above, but for the AISI M7 high speed steel, is presented in Ref. [100]. In this reference, it has also been concluded that the maximum plastic zone size for M7 high speed steel in the DT test genuinely satisfies the small scale yielding restriction.

CHAPTER

CONCLUSIONS

This dissertation examines a highly versatile and simplistic
fracture toughness test configuration using a specially developed
finite element technique. The finite element analysis involved shows
that excellent correlation between the numerical and experimental
results can be obtained for the DT test described in this dissertation.
The maximum stress intensity factor is shown to be <u>almost independent
of crack length</u> (c) over a considerable range. A generalized cali-
bration equation is provided for this test.

The variation of the stress intensity factor along the curved
or straight crack fronts of the DT specimen was also presented. The
complex stress field, groove effects, and plastic zone size were
similarly discussed. An elastic analysis procedure was instituted
for the accurate investigation of the 3-D aspects of the DT pre-
cracked specimen. The elastic-perfectly plastic crack front deforma-
tion was also investigated through a 2-D equivalent model which was
designed to allow the $^1/r$ shear singularity and through a J-integral
evaluation. In this plastic zone analysis, some additional insight
into the area of elastic-plastic fracture mechanics is also provided.

In the elastic analysis, a special 3-D wedge element was devel-
oped to represent the elastic crack front singularity. This special

element has been demonstrated to be highly effective and efficient through a 3-D compact specimen analysis. The comparison between the present results and other published results is also given. Consquently, a great deal of fundamental information was revealed from this comparison. This is, of course, important to interpretation of fracture test results which are typically obtained on this kind of specimen. It is also of interest for the information it sheds on the actual 3-D aspects of what is commonly treated as a 2-D problem.

From the finite element results, some conclusions can be made as follows regarding the DT test:

(1) The basic premise that K_{IC} values obtained using the test, following the admittedly approximate analysis of the calibration equation, are independent of crack length is essentially true, if the crack length is greater than 0.35 of the specimen width and ligament length is greater than 0.65 width.

(2) The above statements imply that if the range of near constant K_{IC} value is required for more than 50% of the specimen length, the width-to-length ratio should be less than 1/2.

(3) The normalized stress intensity factor can be seen to vary around the curved crack front, however for typically utilized geometries, SIF variation is such that no serious error should be incurred in using the calibration equation to determine K_{IC}.

(4) To form a flat crack growth surface for a relatively thin specimen and to maintain a crack path upon the line of symmetry, the use of both upper and lower grooves is recommended. From the present

analysis, the groove effect on the maximum SIF can be neglected for a specimen with quarter-elliptical crack front.

(5) Based on the experimental results of Ten Haagen and Berry, the minimum specimen thickness to avoid a plastic instability condition is specified in Eq. (3·17). This thickness requirement represents a 90% saving in this dimension when compared with a valid ASTM specimen. This is important since in testing tough materials of moderate yield strength, the required thickness of the ASTM specimen is, of course, a major limitation in determination of K_{IC}.

(6) To satisfy the small-scale yielding fracture criterion, it is recommended that the crack size requirement of the ASTM standards, Eq. (9·7) should be held for the DT testing. However, the corresponding crack size of the DT specimen can be defined from Eq. (9·6).

(7) Based on the elastic-perfectly plastic analysis, the ASTM crack size requirement is seen to be an extremely conservative requirement for the DT test, particularly as compared with the ASTM standard tests.

(8) A crack aspect ratio b/c smaller than 0.3 is desirable (This would not imply any practical difficulty). The crack aspect ratio b/c of cracked double torsion specimens of which the writer is aware is almost always smaller than 0.25.

(9) A four-point bending loading technique is recommended. For effective loading, the distance between the loads should be made as small as possible.

The above information may be applied to other cracked structure analyses or to fracture tests involving similar loadings and to specimens precracked in this way.

The present elasto-plastic technique can also be extended, with some modifications, to three-dimensional elasto-plastic analysis, which would provide a more realistic fracture criterion for real test materials, wherein the plastically yielded region near the crack front is no longer small.

The finite element results obtained for the idealized double torsion specimen and for the groove effects are still awaiting supportive experimental data. Experimental techniques for providing a crack front approximating a straight line and for measuring the groove effect are currently made development.

Finally, to explain the dependence of K_C upon fracture growth surface appearance and to analyze mixed mode fracture problems, a generalized fracture criterion is also proposed in this dissertation. However, this criterion also awaits physical and experimental verification, since the problems involved are still far from being completely understood.

APPENDIX A

BASIC CONCEPTS OF THE PLANE THEORY OF ELASTICITY

Using the Cartesian coordinates (x, y, z), the equations of elasticity reduce to a two-dimensional form in three special cases which are of interest:

1. Plane Strain: In this case, the displacement component in z-direction, w, is identically equal to zero, and none of the physical quantities depends on z.

2. Plane Stress: In a state of plane stress parallel to the xy-plane, the stress components σ_{xz}, σ_{yz}, σ_{zz} all vanish but the components of the displacement vector are not, in general, independent of z.

3. Generalized Plane Stress: This is a state of stress in a thin plate $-h \leq z \leq h$ when $\sigma_{zz} = 0$ throughout the plate but $\sigma_{xz} = \sigma_{yz} = 0$ only on the surfaces $z = \pm h$ of the plate.

In view of these definitions, the stress components for plane stress are

$$\sigma_{xx} = \sigma_{xx}(x,y),$$

$$\sigma_{yy} = \sigma_{yy}(x,y),$$

(A·1)

$$\sigma_{xy} = \sigma_{xy}(x,y),$$

$$\sigma_{zz} = \sigma_{xz} = \sigma_{yz} = 0,$$

and for plane strain are

$$\sigma_{xx} = \sigma_{xx}(x,y)$$

$$\sigma_{yy} = \sigma_{yy}(x,y)$$

$$\sigma_{xy} = \sigma_{xy}(x,y) \qquad\qquad\qquad (A \cdot 2)$$

$$\sigma_{zz} = \nu \, (\sigma_{xx} + \sigma_{yy})$$

$$\sigma_{xz} = \sigma_{yz} = 0$$

The equilibrium equations for plane strain and plane stress in the absence of body forces become

$$\frac{\partial \sigma_{xx}}{\partial x} + \frac{\partial \sigma_{xy}}{\partial y} = 0,$$

$$\qquad\qquad\qquad (A \cdot 3)$$

$$\frac{\partial \sigma_{xy}}{\partial x} + \frac{\partial \sigma_{yy}}{\partial y} = 0,$$

In the case of generalized plane stress, we treat the equilibrium equations in terms of mean values $\bar{\sigma}_{xx}$, $\bar{\sigma}_{yy}$, $\bar{\sigma}_{xy}$ of stress components (σ_{xx}, σ_{yy}, σ_{xy}) defined as follows

$$\bar{\sigma}_{xx}(x,y) = \frac{1}{2h} \int_{-h}^{h} \sigma_{xx}(x,y,z) \, dz$$

$$\bar{\sigma}_{yy}(x,y) = \frac{1}{2h} \int_{-h}^{h} \sigma_{yy}(x,y,z) \, dz \qquad (A\cdot 4)$$

$$\bar{\sigma}_{xy}(x,y) = \frac{1}{2h} \int_{-h}^{h} \sigma_{xy}(x,y,z) \, dz$$

where bars over the letters denote mean values. Since σ_{zz}, σ_{xz}, and σ_{yz} are zero on the ends, i.e. $z = \pm h$, in the absence of body forces, it can be shown that [101]

$$\bar{\sigma}_{zz} = 0$$

$$\frac{\partial}{\partial z}(\bar{\sigma}_{xz}) = 0 \qquad (A\cdot 5)$$

$$\frac{\partial}{\partial z}(\bar{\sigma}_{yz}) = 0$$

where $\bar{\sigma}_{xz}$ and $\bar{\sigma}_{yz}$ are similarly defined as Eq. (A·4). The equilibrium equations for generalized plane stress are

$$\frac{\partial \bar{\sigma}_{xx}}{\partial x} + \frac{\partial \bar{\sigma}_{xy}}{\partial y} = 0$$

$$\qquad (A\cdot 6)$$

$$\frac{\partial \bar{\sigma}_{xy}}{\partial x} \quad \frac{\partial \bar{\sigma}_{yy}}{\partial y} = 0$$

Comparison of Eq. (A·3) with Eq. (A·6) shows that the mean values of the stress components $(\bar{\sigma}_{xx}, \bar{\sigma}_{yy}, \bar{\sigma}_{xy})$ satisfy the same equations which govern the cases of plane strain and plane stress. We may write the equations of generalized plane stress without bars over the symbols and then Eq. (A·6) becomes Eq. (A·3). We merely keep in mind that components of stress are mean values. Often, when the term "plane stress" is used, "generalized plane stress" is actually implied. However, if the stress components, σ_{xz} and σ_{yz}, are considered, the "generalized plane stress" is to be distinguished from the "plane stress".

If only the stresses (or forces) are specified in the boundary surface, the boundary condition can be expressed as

$$T_x(x,y) = \ell_x \sigma_{xx} + \ell_y \sigma_{xy}$$

$$T_y(x,y) = \ell_x \sigma_{xy} + \ell_y \sigma_{yy}$$

$$(A·7)$$

where T_x and T_y are the components along the axes of the applied stresses. ℓ_x and ℓ_y are the direction cosines of the exterior unit normal to the surface. Considering the elastic deformation of the plane body, the mathematical formulation of the condition for compatibility of stress distribution with the deformation may be found as

$$\left(\frac{\partial^2}{\partial x^2} + \frac{\partial^2}{\partial y^2}\right) (\sigma_{xx} + \sigma_{yy}) = 0 \qquad\qquad\qquad (A\cdot8)$$

The equations of equilibrium (A·3) or (A·6) together with the boundary conditions (A·7) and the above compatibility equation give one a system of equations that is usually sufficient for the complete determination of the stress distribution. The solution subject to the stress boundary conditions (A·7) is usually referred to as the stress boundary value problem. In the stress boundary value problem, the equations determining stress distribution do not contain the elastic constant of material. Hence, the stress distribution is same for all isotropic materials.*

It should also be noted that the compatibility equations (A·8) and equilibrium equations (A·3) hold for all the three cases, i.e. plane strain, plane stress, and generalized plane stress. The stress distribution is hence the same in these three cases, provided the stress boundary conditions (A·7) are the same. Mathematically, the existence of single-valued stress components σ_{xx}, σ_{yy} and σ_{xy} can be proved for both the simply and the multiply connected regions [101].

---

*For a multiply-connected body, if the resultant of the forces (stresses) applied to each boundary is zero, this conclusion still holds. Nevertheless, if the resultant of the applied forces does not vanish on each boundary, quantitatively, the effect of the moduli on the maximum stress is usually very small, and in practice it can be neglected [92].

APPENDIX B

SOME COMMENTS ON ASTM FRACTURE
TOUGHNESS TESTS AND RELATED SPECIMEN DIMENSIONS

The test procedure for fracture toughness testing is standard-
ized by the ASTM [70]. The recommended ASTM specimens are three-
point bend specimen and compact (tension) specimen. Because of the
difficulty of undertaking a complete 3-D stress analysis, the cali-
bration equations of these specimens were derived by a 2-D boundary
collocation method [70,71]. The planar calibration equations which,
of course, hold the same forms for both the plane strain and plane
stress cases*, are for the bend specimen:

$$K_I = \frac{PS}{tW^{3/2}} [2.9(\frac{c}{W})^{1/2} - 4.6(\frac{c}{W})^{3/2} + 21.8(\frac{c}{W})^{5/2}$$
$$- 37.6(\frac{c}{W})^{7/2} + 38.7(\frac{c}{W})^{9/2}] \tag{B·1}$$

and for the compact (tension) specimen

$$K_I = \frac{P}{tW^{1/2}} [29.6(\frac{c}{W})^{1/2} - 185.5(\frac{c}{W})^{3/2} + 655.7(\frac{c}{W})^{5/2}$$
$$- 1017.0(\frac{c}{W})^{7/2} + 638.9(\frac{c}{W})^{9/2}] \tag{B·2}$$

---

*See some discussions in the first section of Chapter II.

where the symbols are defined in Fig. 7. Physically, without sub-
stantial error, the above calibration equations are confined to
specimens whose thicknesses, as compared with the crack length and
other specimen dimensions, are relatively either large (plane strain)
or small (plane stress). However, it is specified by the ASTM that
the specimen thickness, t, the specimen width, W, and the crack
length, c, be of the same order of magnitude [70]. Naturally, to
develop a valid plane strain test, a specimen whose thickness is
relatively large as compared with the crack length or specimen width
is required. This is frequently quite impracticable. It should be
noted that near the crack edge in a plate (except on the surfaces of
the plate per se), the stress is always in a state of plane strain
[102]. The conditions for plane stress, therefore, would seem to be
violated for any cracked plate. To ensure high accuracy testing
results, any such test relies strongly on the availability of a 3-D
analysis. It is noteworthy that an effective and efficient 3-D
analysis has been developed in this research.

To describe a state of stress, a term "semi-plane" will be
used here for convenience. This state of stress will be defined as
a condition for which loading and geometry are not variable in thick-
ness direction and therefore can be described mathematically as a
plane strain or plane stress condition.* However, it is associated
with a thickness too small to satisfy the plane strain condition, and

---

*A mathematical description of Plane Strain or Plane Stress
may be referred in Appendix A.

too large for the plane stress condition. As discussed above, the ASTM "plane strain" fracture toughness specimens are not genuinely plane strain specimens per se but are "semi-plane" specimens. In the ASTM standard testing procedure, we usually apply the 2-D calibrations to the semi-plane specimens, i.e. we ignore the specimen thickness effect. In other words, as long as the specimens provide straight crack fronts and flat crack surfaces, i.e. the semi-plane conditions, the 2-D calibrations can be applied. As will be gathered, the ASTM semi-plane specimens are designed for Mode I fracture toughness testing. From the fracture loads and the calibration equations, the critical stress intensity factors, K_{IC}, can be estimated. It is suggested here that the estimated critical stress intensity factors are independent of the specimen thicknesses as long as the testing specimens satisfy the semi-plane condition. The above condition is based on the fact that the variance due to using the 2-D calibrations are not considered here. Srawley [103] predicted that the SIF is underestimated, probably, 5%, from using the 2-D calibration. Based on the 3-D finite element results presented in Chapter V, it can be seen that the maximum SIF for an idealized compact specimen is 4% higher than that obtained from a 2-D analysis. Compared with the 3-D result, Srawley's prediction is adequate.

APPENDIX C

COMPUTATION OF K_I BY A 3-D CRACK OPENING DISPLACEMENT METHOD

A 3-D crack opening displacement method has been developed by Kathiresan [48]. This method can be utilized very effectively to estimate the stress intensity factor from the displacement solution of the finite element models where special elements with a correctly embedded singularity are used.

As shown in Chapter IV, the present 3-D special element allows for proportional to the distance from the crack edge and to the square root of the distance from the crack edge and allows for linear and quadratic variations along the edges. Referring to Fig. 9·a and assuming that the surface abcd ($\eta=1$) represents the crack surface, the binormal (y-direction) displacement v on the surface abcd can be expressed as

$$v = a_1 + a_2 r^{\frac{1}{2}} + a_3 \zeta + a_4 r + a_5 \zeta^2 + a_6 r^{\frac{1}{2}} \zeta + a_7 r \zeta + a_8 r^{\frac{1}{2}} \zeta^2 \quad (C \cdot 1)$$

where r is exactly the same as ξ in Fig. 9·a. The values of $a_1 \ldots \ldots, a_8$ can be calculated by substituting the nodal displacements of nodes a, b, c, d, e, f, g, and h. Now considering the displacements of the nodes relative to the displacements of the crack front, Eq. (C·1) may be reduced to

$$v = a_2 r^{\frac{1}{2}} + a_4 r + a_6 r^{\frac{1}{2}}\zeta + a_7 r\zeta + a_8 r^{\frac{1}{2}}\zeta^2 \qquad (C\cdot 2)$$

Here, the five constants a_2, a_4, a_6, a_7, and a_8 can be evaluated from the near crack front nodes c, d, f, g, and h.

From the asymptotic near field solution for displacements, i.e. Eq. (2·7), for the crack surface where $\theta=\pi$ (refer to Fig. 3), we get

$$v = \frac{K_I}{\mu} \left(\frac{r}{2\pi}\right)^{\frac{1}{2}} (2-2\nu) \qquad (C\cdot 3)$$

As defined in Eq. (2·4), mathematically, the stress intensity factors are meaningful only for r approaching zero. Equating Eq. (C·2) and (C·3) and letting $r \to 0$, it follows that

$$K_I = \frac{\mu}{(1-\nu)} \left(\frac{\pi}{2}\right)^{\frac{1}{2}} (a_2 + a_6\zeta + a_8\zeta^2) \qquad (C\cdot 4)$$

where ζ is the non-dimensional coordinate along the crack edge varying between −1 and +1. The COD method thus yields an equation in which the SIF varies quadratically along the crack front.

APPENDIX D

J-INTEGRAL AND THE COMPUTATIONAL PROCEDURE

Consider a 2-D cracked body with a Cartesian coordinate system (x.y) as shown in Fig. 25. Letting the x-axis parallel to the flat surface of the crack, the path integral J can be expressed as Eq. (2·11). This integral is evaluated in a counterclockwise sense starting from the lower flat notch surface and continuing along the path Γ to the upper flat surface. The strain energy density w_s is defined as

$$w_s = \int \sigma_{xx} \, d\varepsilon_{xx} + \sigma_{yy} \, d\varepsilon_{yy} + \sigma_{xy} \, d\varepsilon_{xy} \qquad (D·1)$$

For a 2-D linear or nonlinear elastic body free of body forces, Rice [66] have shown that J is path independent. In effect, this means that the line integral has the same value for all paths surrounding the crack tip. Therefore, by calculating J over a path remote from the crack tip, a number which characterizes conditions at the crack tip can be calculated.

Path independence has also been proven for paths passing through the plastic zone when a deformation plasticity theory is employed [66]. For the incremental theory of plasticity as used in the present plastic zone analysis, the path independence has never

been rigorously proven. It has been numerically demonstrated by a number of investigators [104,105] that for purposes of engineering application J can be assumed to be path independent for incremental plasticity.

Eq. (2·11) is evaluated numerically by assuming that the components of both the stress and displacement gradients and the strain energy vary linearly over each straight linear segment which joins two adjacent nodes i and j making up the selected path Γ, i.e.,

$$\sigma_{xx} = \sigma_{xx}\big|_i + (\sigma_{xx}\big|_j - \sigma_{xx}\big|_i)(\frac{y-y_i}{y_j-y_i}) \text{ etc.} \qquad (D·2)$$

and

$$\frac{\partial u}{\partial x} = \frac{\partial u}{\partial x}\bigg|_i + (\frac{\partial u}{\partial x}\bigg|_j - \frac{\partial u}{\partial x}\bigg|_i) (\frac{y-y_i}{y_j-y_i}) \text{ etc.} \qquad (D·3)$$

Once this assumption is made, the integral can be mathematically represented in closed form over each segment of the path. Therefore, the contribution of each segment to total path integral can be directly calculated and then summed to give the value of J over the path.

It should be noted that the J-integral expressions shown in Eqs. (2·11), (D·2), and (D·3) are valid only if the coordinate axis x is parallel to the flat surfaces of the crack. In the present J-

integral evaluations, the crack surface parallel to x-axis is always arranged.

For a linear elastic analysis, the strain energy density is computed from the current stress and strain result. Thus, Eq. (D·1) becomes

$$w_s = \frac{1}{2} (\sigma_{xx} \, \varepsilon_{xx} + \sigma_{yy} \, \varepsilon_{yy} + \sigma_{xy} \, \varepsilon_{xy}) \qquad (D·4)$$

For an elastic-plastic analysis, the strain energy density is computed by the expression of Eq. (D·1) throughout the history of the loading. It should be noted that the strains ε_{ij} used in the present plastic zone analysis include strains due to elastic and plastic deformations. The numerical procedure considering both the elastic and plastic strain components for J calculation is given in Ref. [106].

APPENDIX E

THEORETICAL BASIS OF THE ELASTIC-PLASTIC ANALYSIS

This appendix outlines the theory and solution procedure used
in the WECAN (Westinghouse Electric Computer ANalysis) computer
program which was utilized in the present DT plastic zone analysis.
Verification of the plastic capabilities of this program may be found
in Ref. [29].

Elements of the Theory of Plasticity

Three ingredients in addition to the elastic stress-strain
relation, are needed in order to describe elastic-plastic material
behavior. These are: (1) a yield surface, which plastic flow
begins, (2) a flow rule which relates the plastic strain increments
to the stresses and stress increments after initial yielding, and
(3) a hardening rule, which specifies the modification of the yield
surface during plastic flow. The theory outlined here applies only
to a 2-D problem with an isotropic non-hardening material.

Elastic Stress-Strain Relation

From the elasticity, the stress-strain relation can be found as

$$\{\sigma\} = [E] \{\varepsilon^e\} \tag{E·1}$$

where $\{\sigma\}$ is the stress vector, $\{\varepsilon^e\}$ the elastic strain vector,

as defined as $\{\varepsilon\}$ in Chapter IV and [E] the elasticity matrix which

is similar to Eq. (4·27).

Yield Surface

It is quite generally postulated, as an experimental fact, that

the yield surface is given by some function of the stress components,

$$f(\sigma_{ij}) = \text{constant} \tag{E·2}$$

According to the von Mises criterion, yield begins under any

state of stress when the effective stress σ_e equals the yield stress

(σ_y) measured in a uniaxial test. The yield surface becomes

$$f = \sigma_e = \frac{1}{\sqrt{2}} \left[(\sigma_{xx} - \sigma_{yy})^2 + (\sigma_{yy} - \sigma_{zz})^2 + (\sigma_{zz} - \sigma_{xx})^2 + 6(\sigma_{xy})^2 \right]^{1/2} \tag{E·3}$$

An effective plastic strain increment $d\varepsilon_e^P$ is defined as a

combination of the separate plastic strain increments:

$$d\varepsilon_e^P = \frac{\sqrt{2}}{3} \left[(d\varepsilon_{xx}^P - d\varepsilon_{yy}^P)^2 + (d\varepsilon_{yy}^P - d\varepsilon_{zz}^P)^2 \right.$$
$$\left. + (d\varepsilon_{zz}^P - d\varepsilon_{xx}^P)^2 + \frac{3}{2}(d\varepsilon_{xy}^P)^2 \right]^{1/2} \tag{E·4}$$

With this expression in mind, the effective plastic strain ε_e^P is

the integral of Eq. (E·4) taken along the loading path so that all

of the increments of plastic strain are included.

The Flow Rule

Prandtl and Reuss suggested the basic constitutive relation defining the plastic strain increments in relation to the yield surface. At the present time this relation is generally accepted and can be written as

$$d \{ \epsilon^P \} = d\lambda \frac{\partial \sigma_e}{\partial \{\sigma\}} \tag{E·5}$$

or for components

$$d \epsilon_{xx}^P = d\lambda \frac{\partial \sigma_e}{\partial \sigma_{xx}} , \quad d\epsilon_{yy}^P = d\lambda \frac{\partial \sigma_e}{\partial \sigma_{yy}} \quad \text{etc.} \tag{E·6}$$

where $d\lambda$ is a proportionality constant and a Poisson's ratio of 1/2 has been introduced. This equation states that the plastic strain increment vector is parallel to the normal to the yield surface at the current stress point on the yield surface. Using the relations established in Eqs. (E·3) and (E·4), $d\lambda$ can be written as

$$d\lambda = d\epsilon_e^P \tag{E·7}$$

If $H' = \frac{d\sigma_e}{d\epsilon_e^P}$ is the slope of the uniaxial stress-plastic strain curve at the current value of σ_e, $d\epsilon_e^P$ can be expressed as

$$d\varepsilon_e^P = \frac{d\sigma_e}{H'} = \frac{1}{H'} \frac{\partial\sigma_e}{\partial\{\sigma\}} \; d\{\sigma\} \qquad (E\cdot 8)$$

Using Eqs. (E·8) for $d\varepsilon_e^P$ and substituting Eq. (E·7) into Eq. (E·5), the increment of plastic strain components become

$$d\{\varepsilon^P\} = \frac{1}{H'} \; \frac{\partial\sigma_e}{\partial\{\sigma\}} \; d\{\sigma\} \; \frac{\partial\sigma_e}{\partial\{\sigma\}} \qquad (E\cdot 9)$$

During an infinitesimal increment of the stress, changes of strain are assumed to be divisible into elastic and plastic parts. Thus,

$$d\{\varepsilon\} = d\{\varepsilon^e\} + d\{\varepsilon^P\} \qquad (E\cdot 10)$$

The elastic strain increments are related to stress increments by a symmetric elasticity matrix [E] as defined in Eq. (E·1) and the plastic strain has been derived in Eq. (E·9). We can thus write Eq. (E·10) as

$$d\{\varepsilon\} = [E]^{-1} d\{\sigma\} + \frac{1}{H'} \; \frac{\partial\sigma_e}{\partial\{\sigma\}} \frac{\partial\sigma_e}{\partial\{\sigma\}} \; d\{\sigma\} \qquad (E\cdot 11)$$

This results in an explicit expansion which determines the stress changes in terms of imposed strain changes with

$$d\{\sigma\} = [E]^{ep} d\{\varepsilon\} \qquad (E\cdot 12)$$

where

$$[E]^{ep} = [E] - \frac{[E] \dfrac{\partial \sigma_e}{\partial \{\sigma\}} \left\{\dfrac{\partial \sigma_e}{\partial \{\sigma\}}\right\}^T [E]}{H' + \left\{\dfrac{\partial \sigma_e}{\partial \{\sigma\}}\right\}^T [E] \dfrac{\partial \sigma_e}{\partial \{\sigma\}}}$$

The elasto-plastic matrix $[E]^{ep}$ takes the place of the elasticity matrix $[E]$ in incremental analysis. It is symmetric and positive definite. Explicit formulation of plasticity in this form was first introduced by Yamada et al. [107]. For elastic-perfectly plastic material H' equals zero and $[E]^{ep}$ can be written as

$$[E]^{ep} = [E] - \frac{[E] \dfrac{\partial \sigma_e}{\partial \{\sigma\}} \left\{\dfrac{\partial \sigma_e}{\partial \{\sigma\}}\right\}^T [E]}{\left\{\dfrac{\partial \sigma_e}{\partial \{\sigma\}}\right\}^T [E] \dfrac{\partial \sigma_e}{\partial \{\sigma\}}} \qquad (E \cdot 13)$$

On differentiating Eq. (E·3), it can be found that

$$\frac{\partial \sigma_e}{\partial \sigma_{xx}} = \frac{3S_{xx}}{2\sigma_e} \ , \quad \frac{\partial \sigma_e}{\partial \sigma_{yy}} = \frac{3S_{yy}}{2\sigma_e}$$

$$\qquad (E \cdot 14)$$

$$\frac{\partial \sigma_e}{\partial \sigma_{zz}} = \frac{3S_{zz}}{2\sigma_e} \ , \quad \frac{\partial \sigma_e}{\partial \sigma_{xy}} = \frac{3\sigma_{xy}}{\sigma_e}$$

in which S_{ij} stands for so-called deviatoric stress

$$S_{xx} = \sigma_{xx} - \frac{(\sigma_{xx} + \sigma_{yy} + \sigma_{zz})}{3} \quad \text{etc.} \quad (E \cdot 15)$$

Hardening Rule

Several different types of hardening rules have been developed. However, only the elastic-perfectly plastic problem is considered in the present analysis. The hardening effect is not discussed in this appendix.

The Method of Successive Elastic Approximations

In recent years two principal approaches for the elastic-plastic analysis of complex structures by the finite element method have emerged. Both are widely used and generally accepted, and each has its advantages and disadvantages for specific problems, depending on such factors as the type of finite element used, the shape of the stress-strain curve, and the modeling of the structure involved. In the first approach, the "tangent modulus method", the stress-strain relations are modified for each plastic load increment. Since the stiffness of each element may change for every load increment, the total stiffness matrix must be assembled and triangularized for each of these increments. In the second approach, the "method of successive elastic approximations", or the "initial strain method", the stress-strain relations stay the same throughout the computations. The stiffness of the elements does not change and thus is is not necessary to repeatedly triangularize the total stiffness matrix; however, it is usually necessary to iterate on the solution in order

to obtain the correct results. The effect of plastic deformation during a load increment is taken into account by introducing a set of fictitious body forces into the equations. These body forces are the result of "initial" strains or "initial" stresses which arise due to the difference between elastic and elastic-plastic material behavior. Some discussions of the method may be found in Refs. [80,98]. The WECAN program uses the method of successive elastic approximations as the basis for an elastic-plastic analysis.

In small strain linear elastic problems formulated by the displacement approach one always arrives at the final solution by solving the assembled stiffness equation, Eq. (4·14)

$$[K] \ \{U\} \ = \ \{R\} \tag{E·16}$$

in which the vector $\{\overline{R}\}$ lists all the loads. In general, the material within the element boundaries may be subjected to initial strain, ε_0, such as may be due to temperature changes.

The internal work done by the initial strain can be similarly treated as the work done by the body force [80] shown in Eq. (4·9),

$$W_{\varepsilon_0} \ = \ - \sum_{m=1}^{M} \ \{d\}_m^T \ \{r_\varepsilon\}_m \tag{E·17}$$

where

$$\{r_\varepsilon\}_m \ = \ \int_{V_m} [D]^T \ [E] \ \{\varepsilon_0\} \ dV \tag{E·18}$$

Consequently, the vector $\{R\}$ in Eq. (E·16) needs to be supplemented by the load due to initial strain, i.e.

$$\{R^*\} = \{R\} + \sum_{m=1}^{M} \{r_\varepsilon\}_m \qquad\qquad (E·19)$$

Here $\{R^*\}$ is the vector including this force due to initial strain.

In an elastic plastic problem, the stress level may be determined in terms of strain. Thus, symbolically

$$\{\sigma\} = F(\{\varepsilon\}) \qquad\qquad (E·20)$$

For a linear elastic problem, the above equation can be reduced as

$$\{\sigma\} = [E](\{\varepsilon\} - \{\varepsilon_o\}) \qquad\qquad (E·21)$$

Now, the equality between Eq. (E·20) and the elastic relation Eq. (E·21) can be obtained by adjusting $\{\varepsilon_o\}$. As $\{\varepsilon_o\}$ affects the forces $\{R^*\}$ we are left with an iterative process of solving [Eq. (E·16)]

$$[K]_o \{U\} - R^* (\{U\}) = 0 \qquad\qquad (E·22)$$

in which we proceed as follows. One solves first

$$\{U\}_o = [K]_o^{-1} \{R^*\}_o \qquad (E \cdot 23)$$

in which $\{R^*\}_o$ corresponds to the actual loads applied ($\{R^*\}_o = \{R\}$).
One determines the level of $\{\varepsilon_o\}_1$ required to bring the elastic
solution into coincidence with the true strains corresponding to the
stresses reached. Using Eqs. (E·18) and (E·19), the corresponding
$\{R^*\}$ can then be calculated. Taking the new $\{R^*\}_1$ we obtain

$$\{U\}_1 = [K]_o^{-1} \{R^*\}_1 \qquad (E \cdot 24)$$

and repeat the process with

$$\{U\}_n = [K]_o^{-1} \{R^*\}_n \qquad (E \cdot 25)$$

until no further changes occur.

Adaptation of the initial strain method in plasticity problems,
through fairly straight forward, is complicated by two facts:

(a) The incremental stress-strain relation, Eq. [E·12] is
only valid from the instant when stresses reach the yield surface,
$\sigma_e = \sigma_y$. If $\sigma_e < \sigma_y$, purely elastic behavior continues.

(b) The incremental relation Eq. [E·12] is valid only for
infinitesimal strain increases. For finite steps it is possible for
stresses to depart somewhat from the yield surface. To guard against
this stresses should be reduced to the yield condition after each
iteration.

APPENDIX F

ILLUSTRATIONS

Figure 1. Basic Modes of Crack Extension
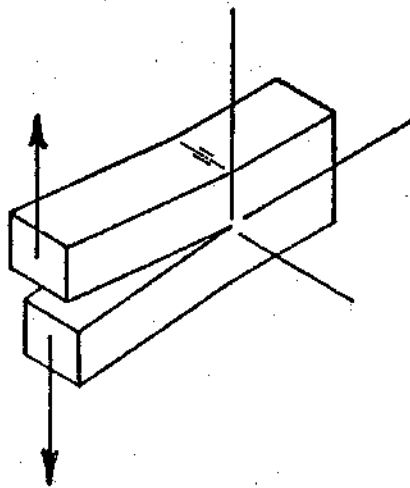
(a) Opening Mode
     (Mode I)
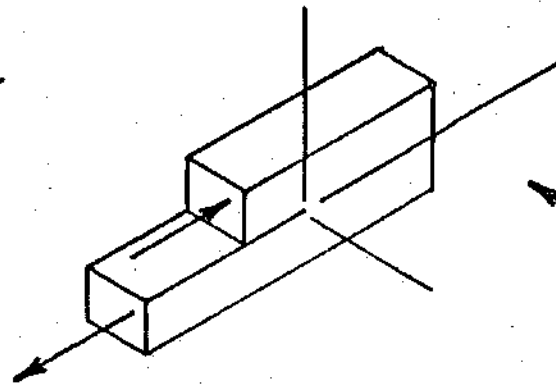
(b) Sliding Mode
     (Mode II)
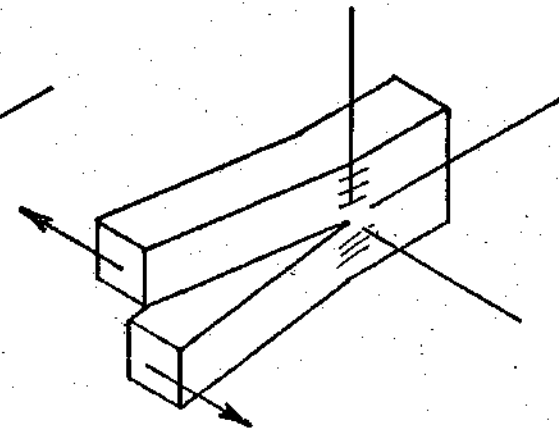
(c) Tearing Mode
     (Mode III)
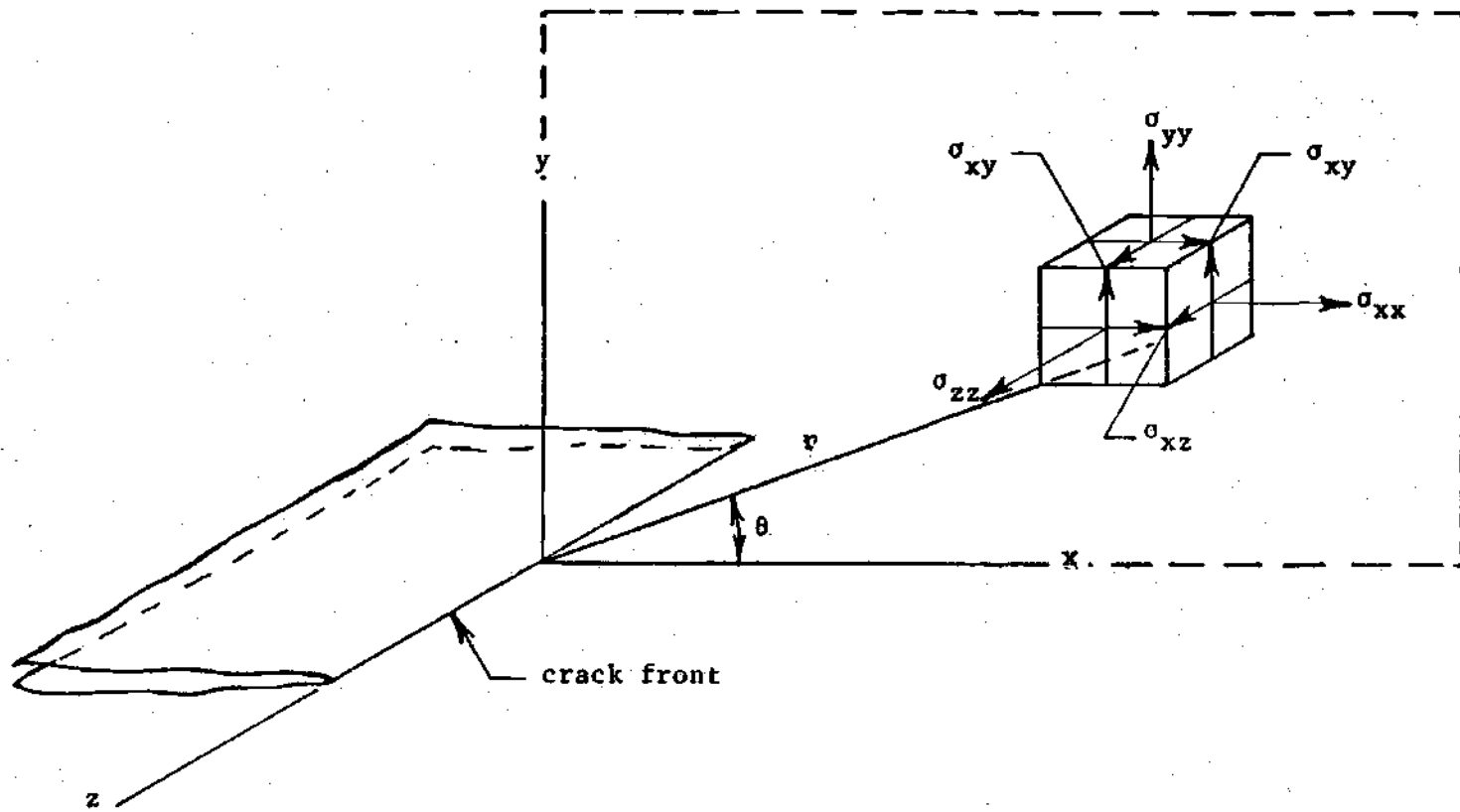
Figure 2.   Nomenclature of Plane Crack
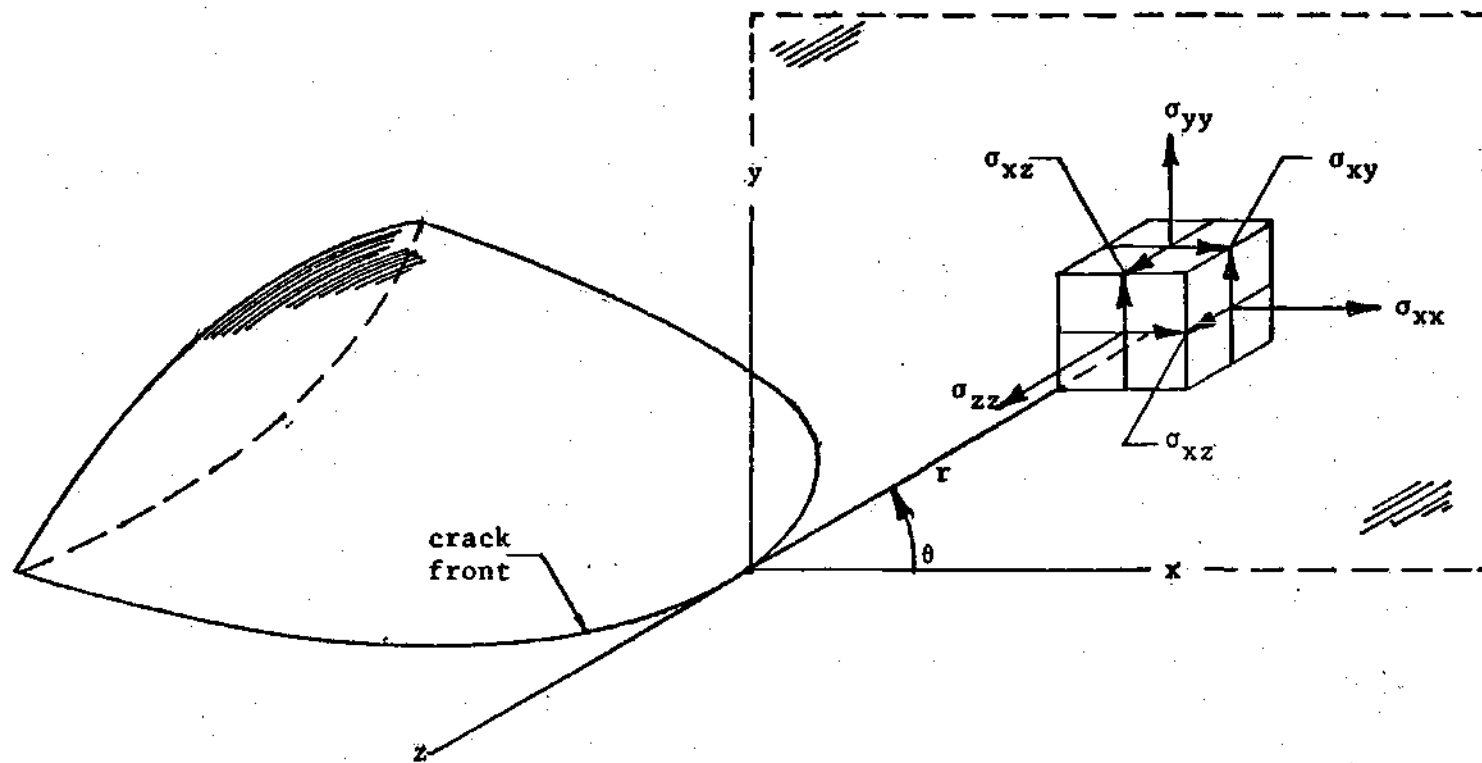
Figure 3.   Nomenclature of 3-D Crack

FATIGUE PRECRACK

P_C

E

t_c b ψ

W_O

$W_m = W_O - \varepsilon$

W

t

L

C
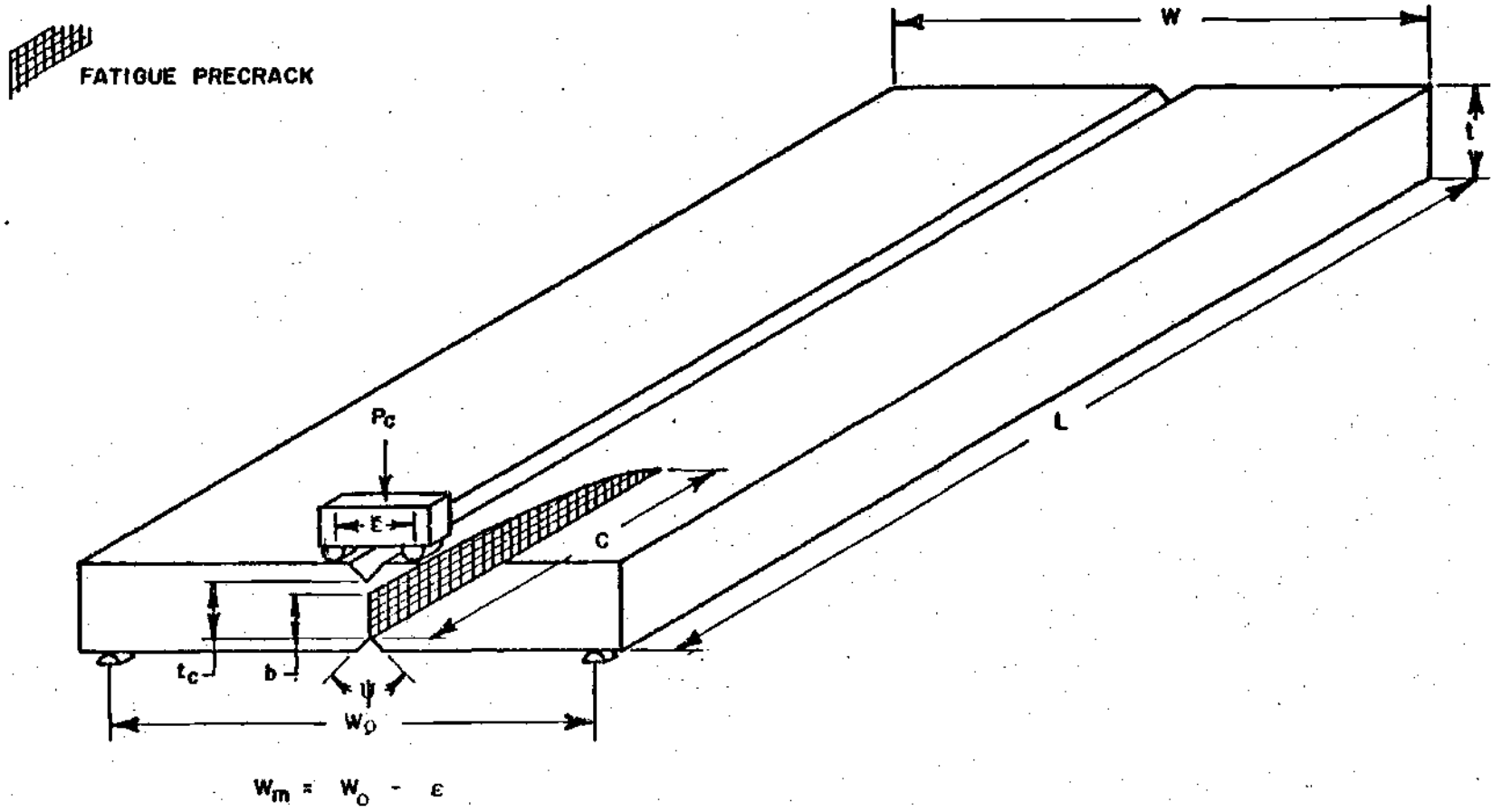
Figure 4. The Double Torsion Test Specimen Under Testing Conditions

128

(a) Penetrated Specimen

(b) Unpenetrated Specimen

Figure 5. Typical Double Torsion Crack Front Profiles

a) Slant Fracture   b) Mixed Mode   c) Flat Fracture

d) Effect of Specimen Thickness
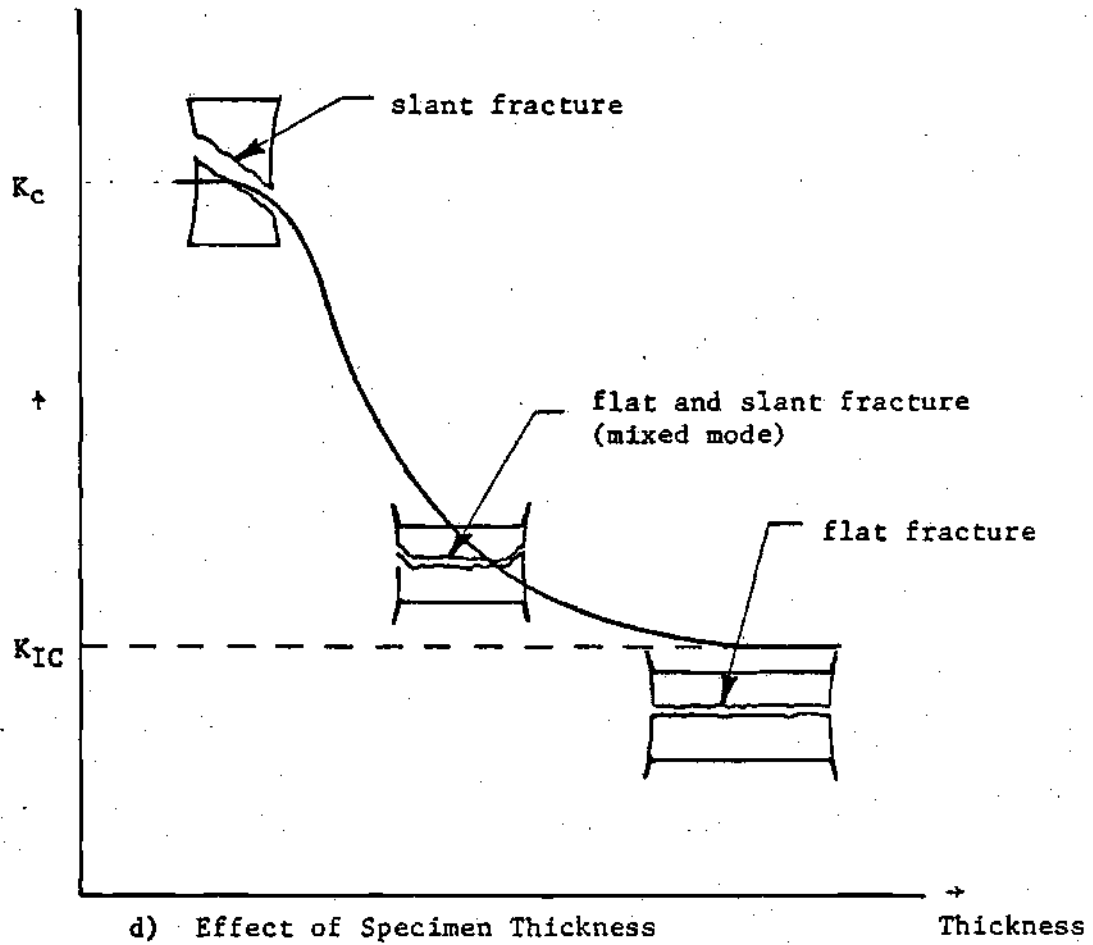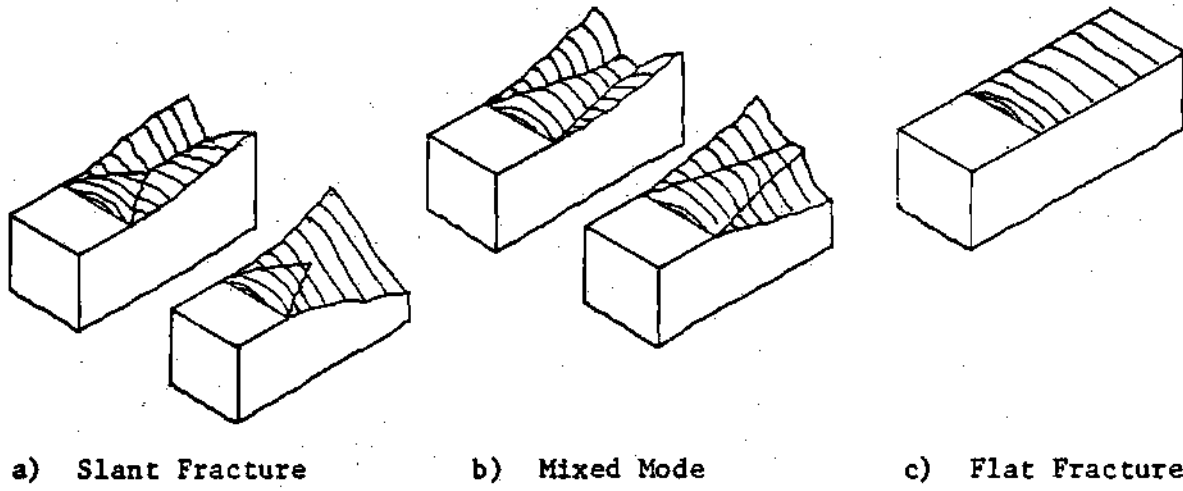
Figure 6. The Dependence of K_C Upon the
Surface Appearance of Fracture Growth
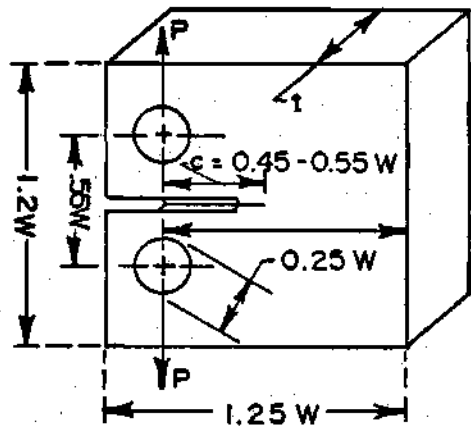
(a) ASTM Compact Specimen
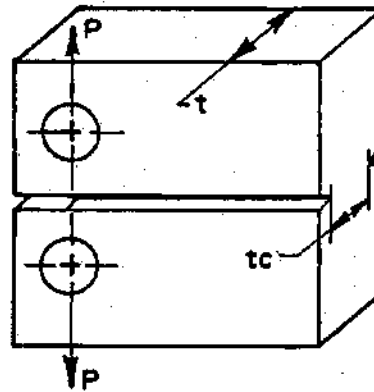
(b) Grooved Compact Specimen
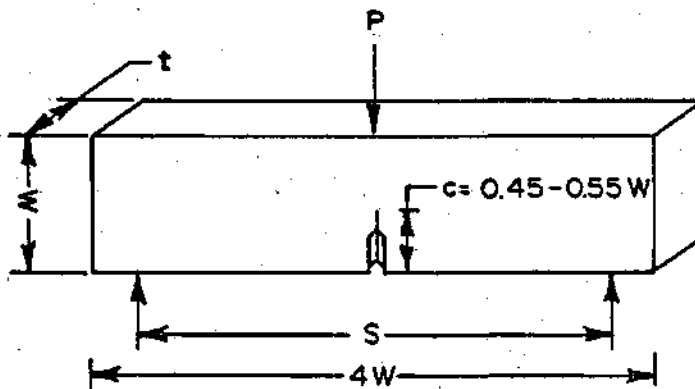
(c) ASTM Bend Specimen

Figure 7. Fracture Toughness Testing Specimens
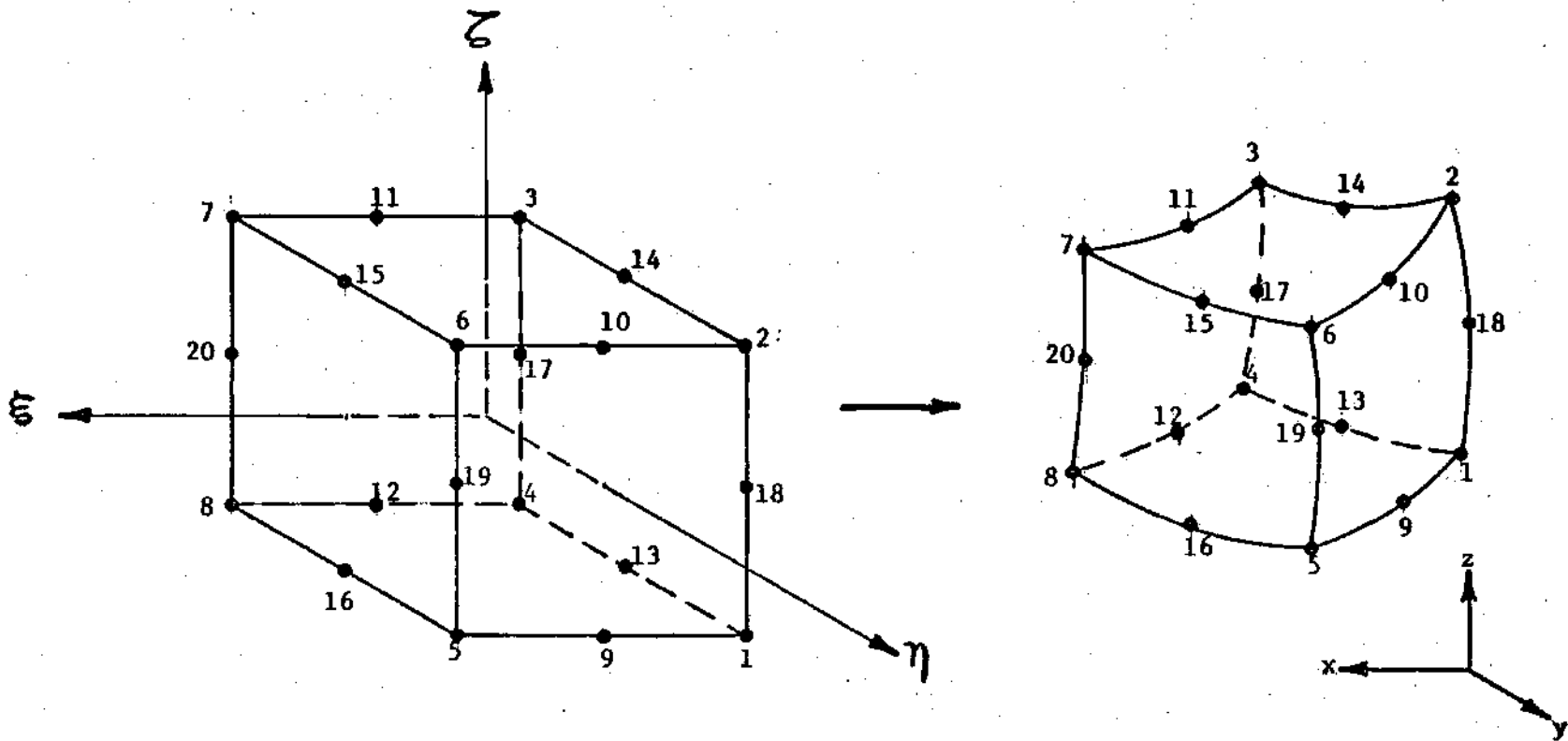
Figure 8. Three-Dimensional Regular Isoparametric Element Mapping
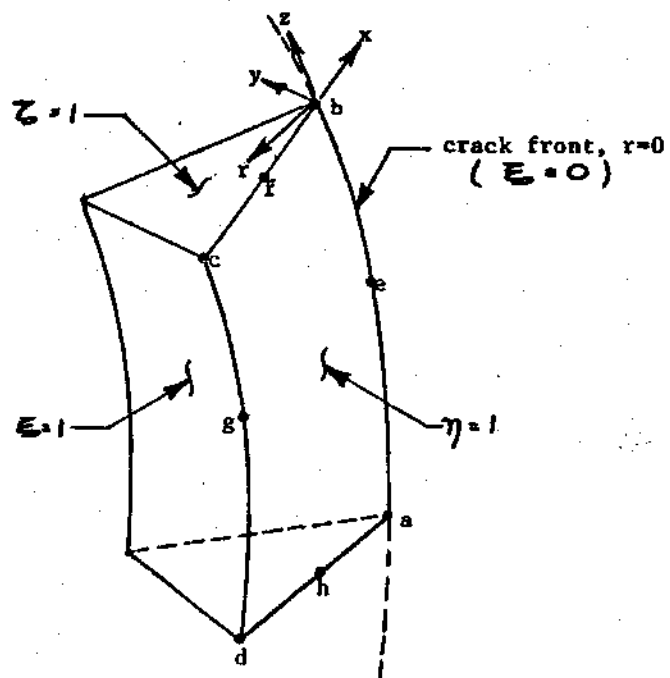
(a) Special Wedge Element
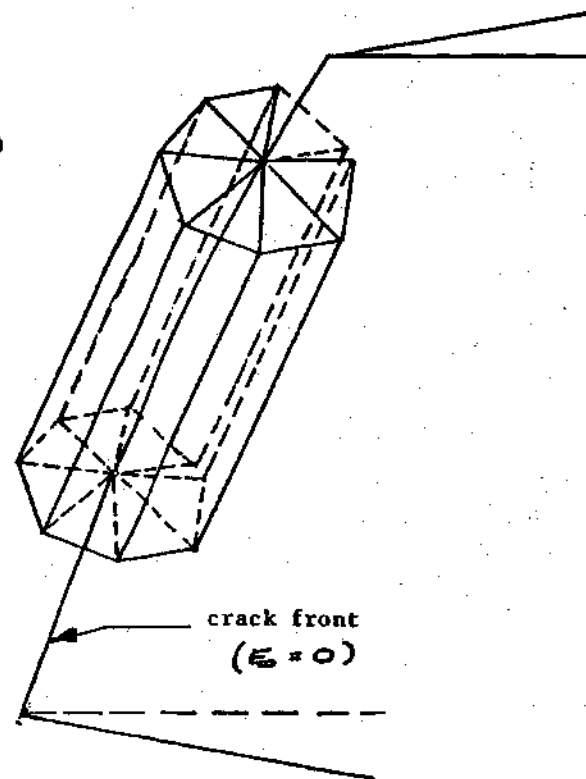
(b) Crack Front Mesh

Figure 9. Crack Front Mesh Geometry Using Special Wedge Elements
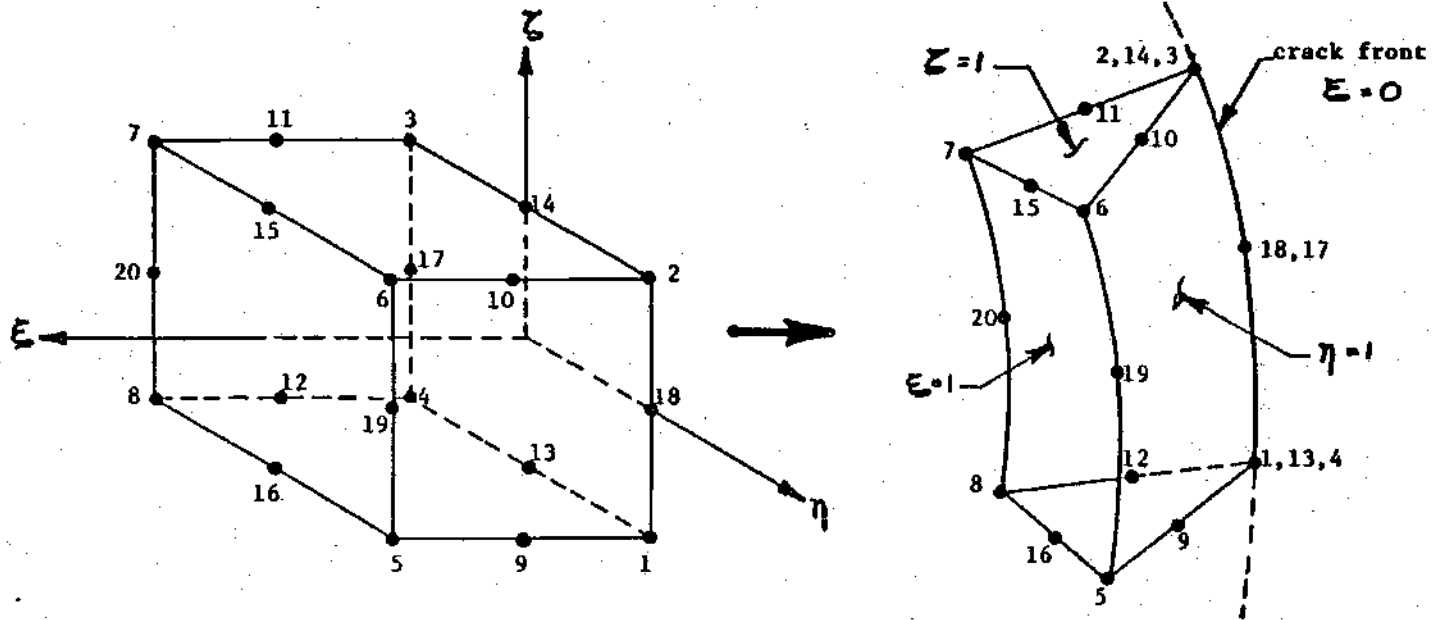
Figure 10. Special Wedge Element Mapping
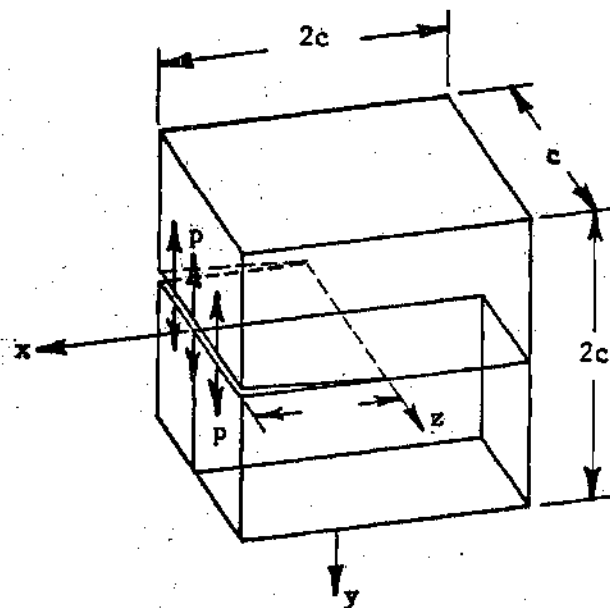
(a) Idealized Compact Specimen
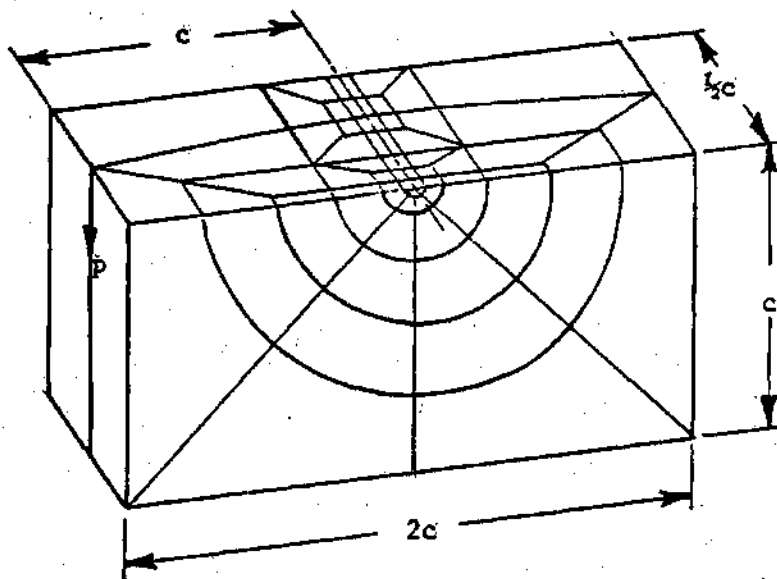
(b) Finite Element Mesh

Figure 11. Model Used in Idealized Compact Specimen Analysis
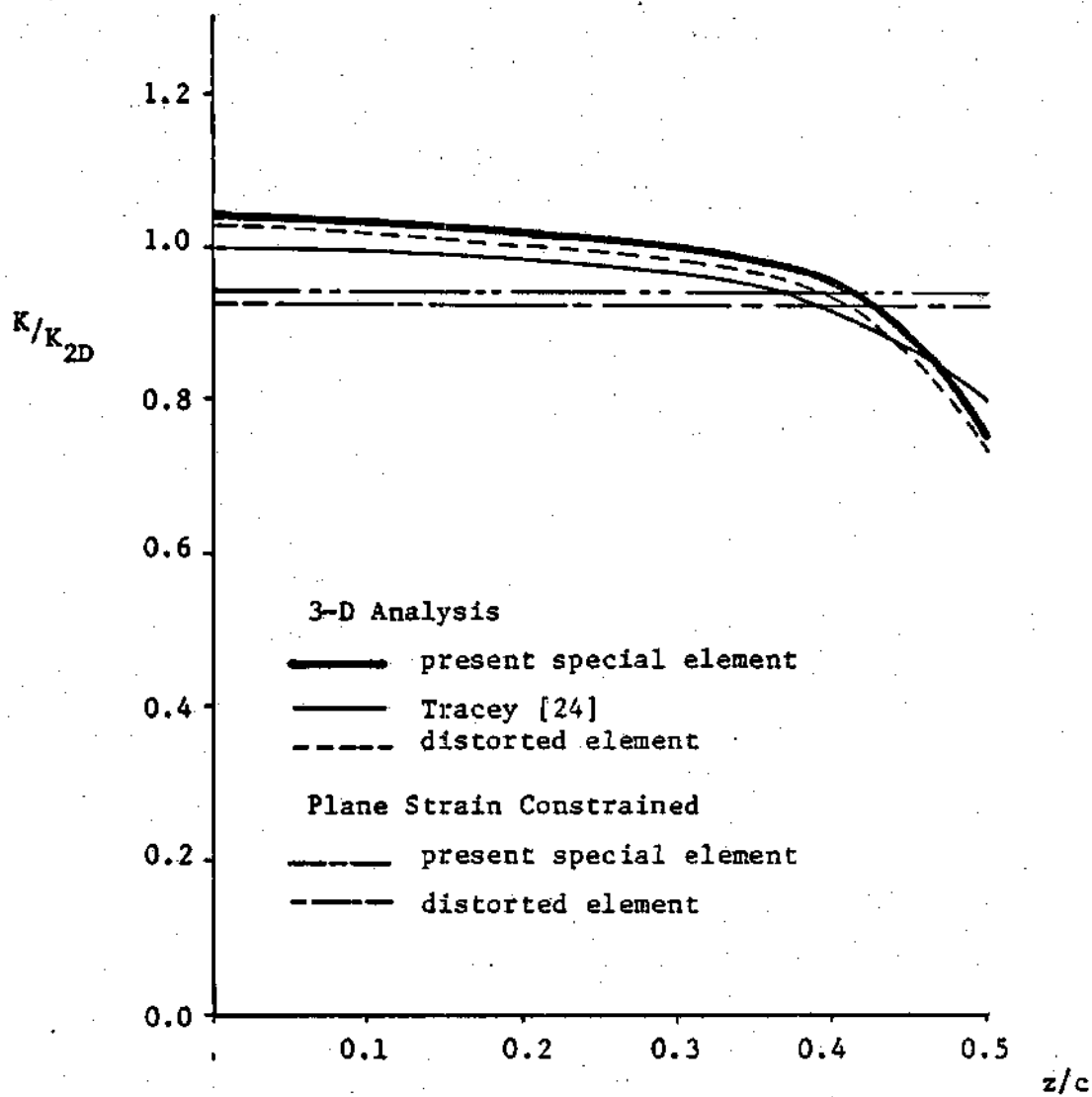
Figure 12.   Crack Front Variation of Normalized
Stress Intensity Factor for Idealized Compact
Specimen Analysis
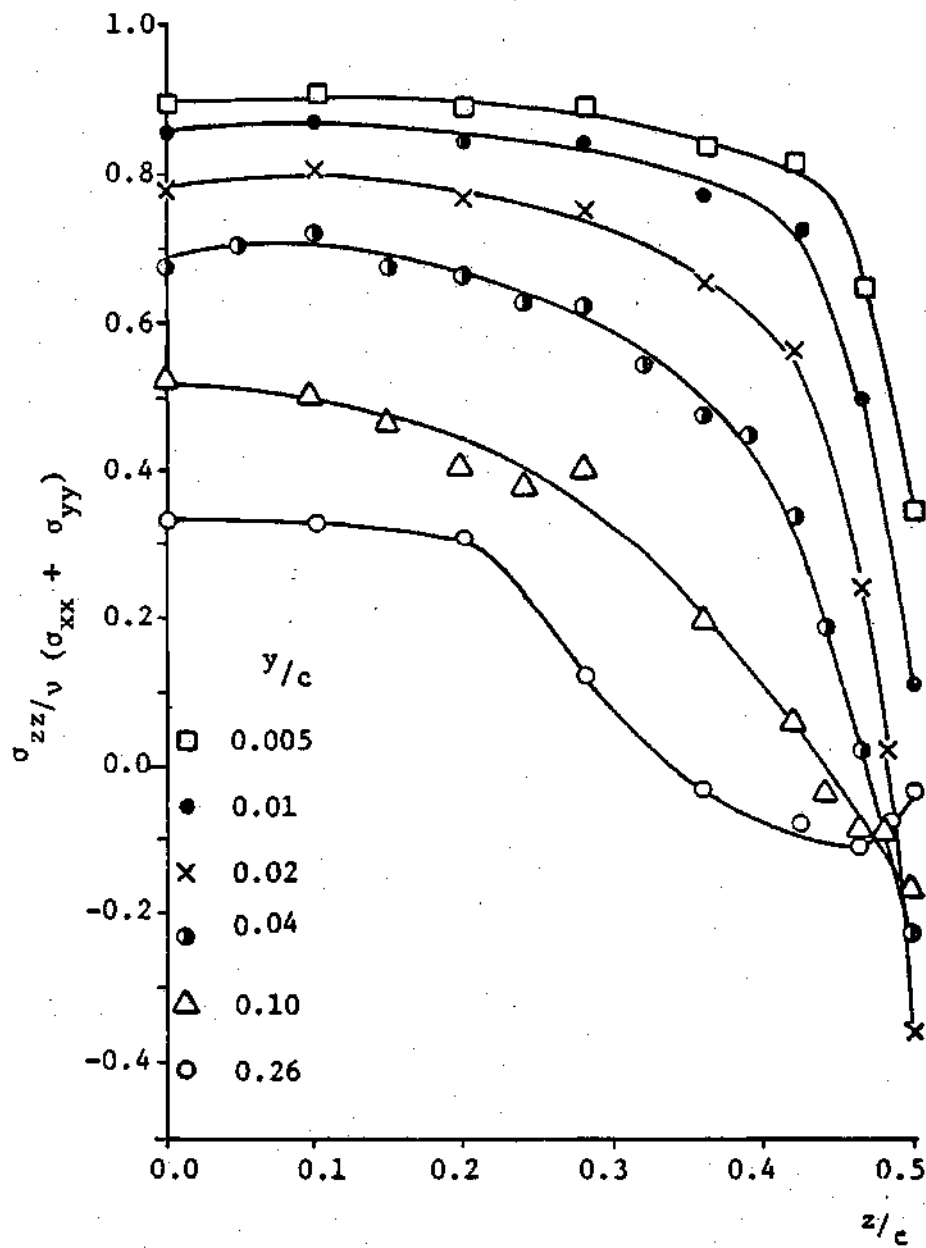
Figure 13. Variation of Constraint Parameter
Across the Idealized Compact Specimen
at Several Radial Positions from the
Crack Front
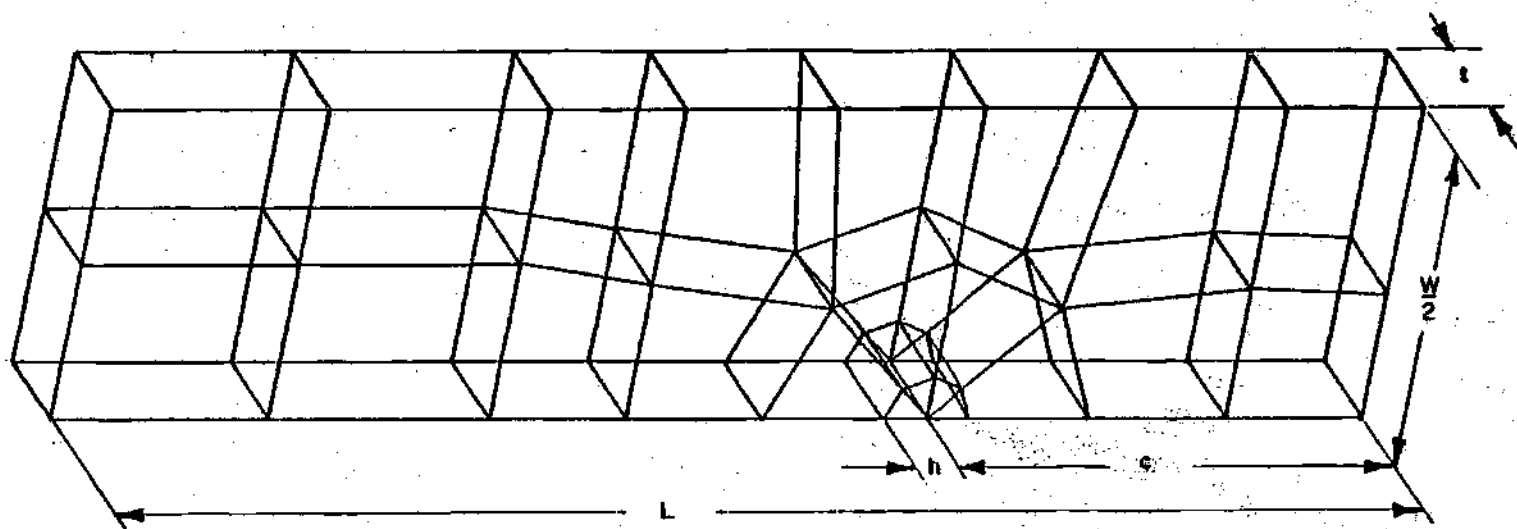
Figure 14. A Typical Coarse Mesh Utilized in Current Idealized Double Torsion Specimen
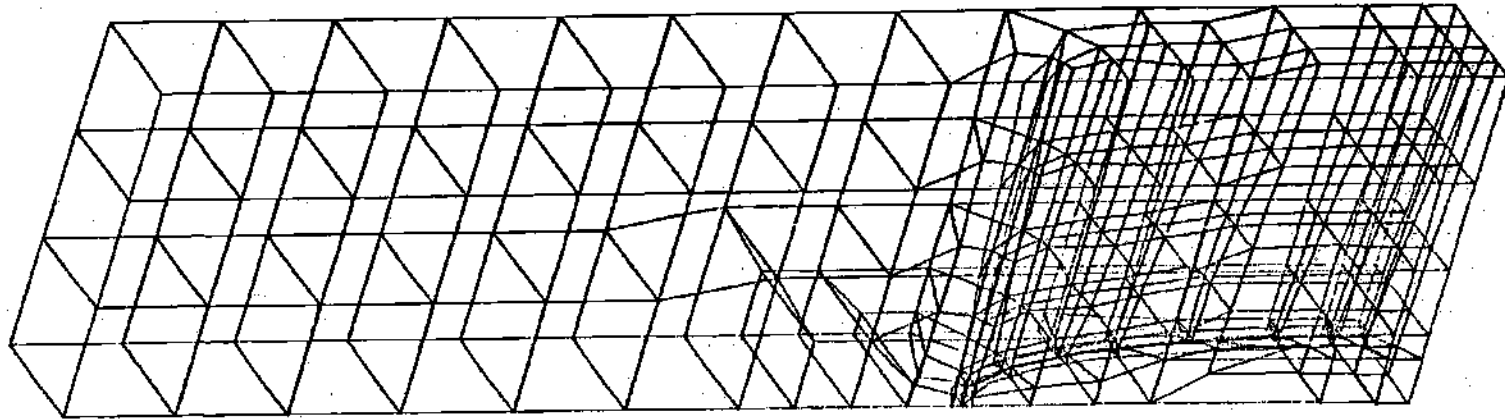
Figure 15. Basic Mesh Utilized for Double Torsion Analysis

(Specimens 2, $\frac{c}{L} = 1/3$, $\frac{2t}{W} = 1/3$, $\frac{b}{t} = 9/10$, $\frac{b}{c} = 0.225$)
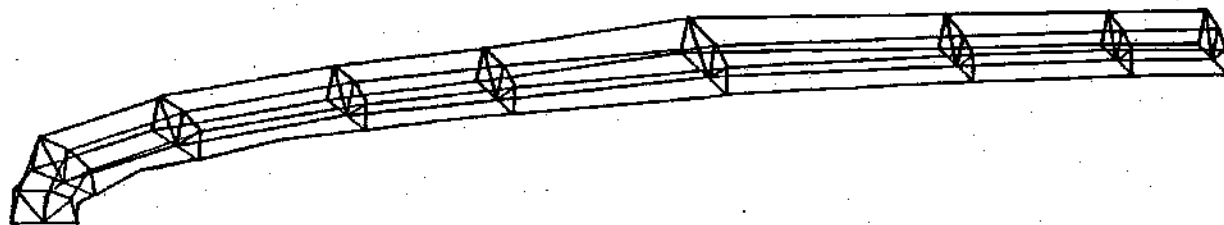
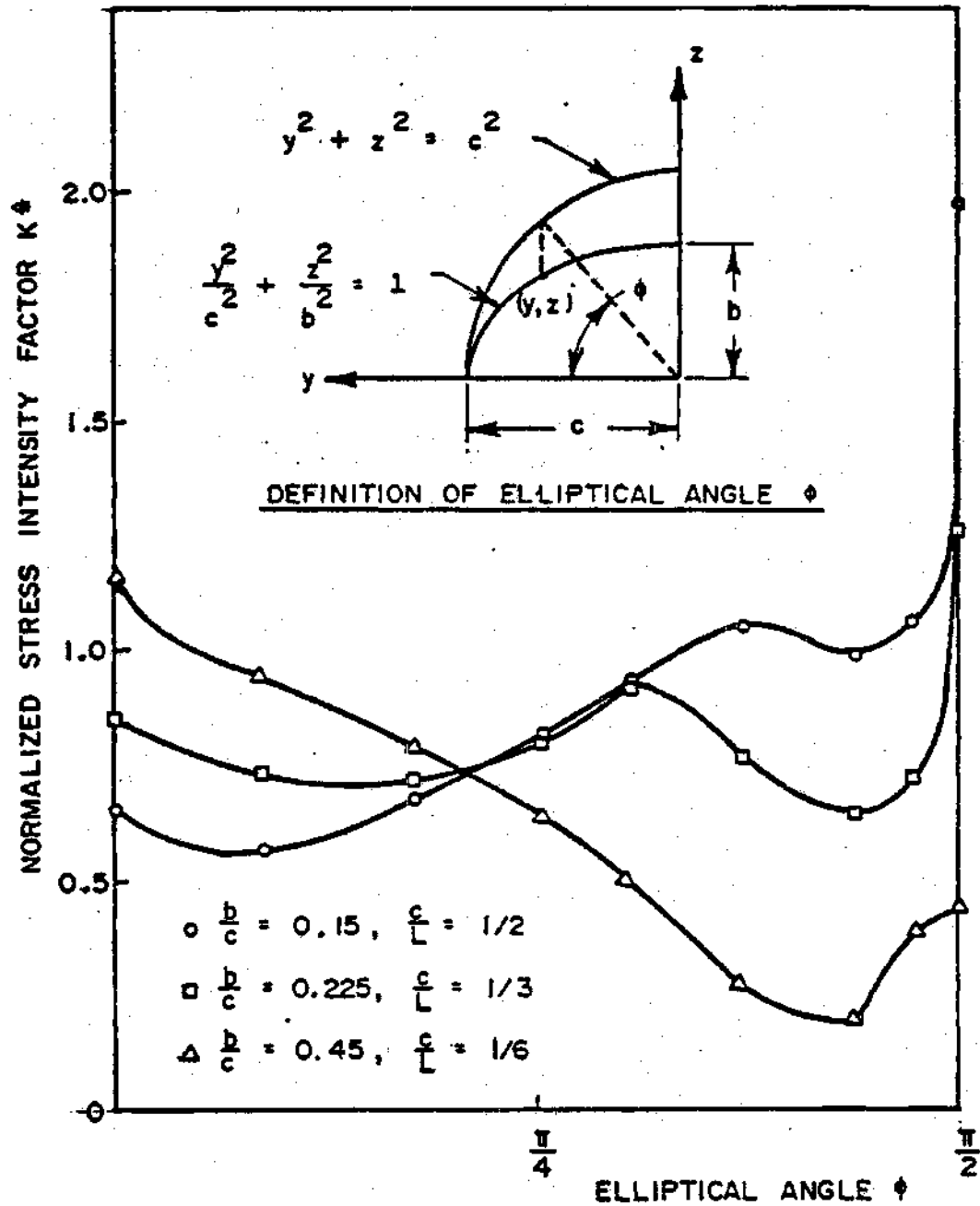Figure 16. Detail of Elements Around the Quarter-Elliptical Crack Profile

Figure 17. Variation of Normalized Stress Intensity Factor
Along the Quarter-Elliptical Crack Front
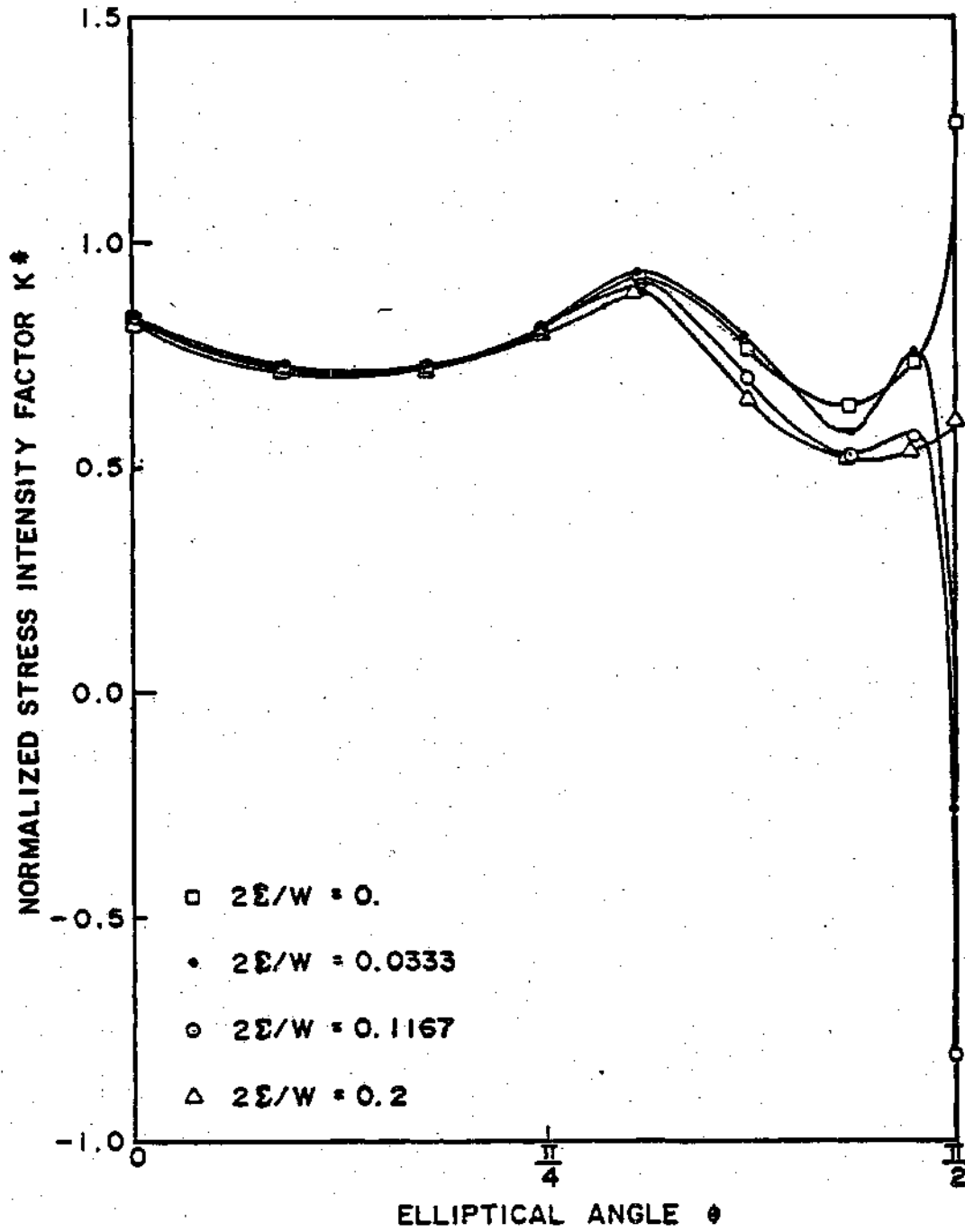($\varepsilon = 0$, $2t/W = 1/3$, $b/t = 9/10$)

Figure 18. Influence of the Distance Between the Applied Loads ε
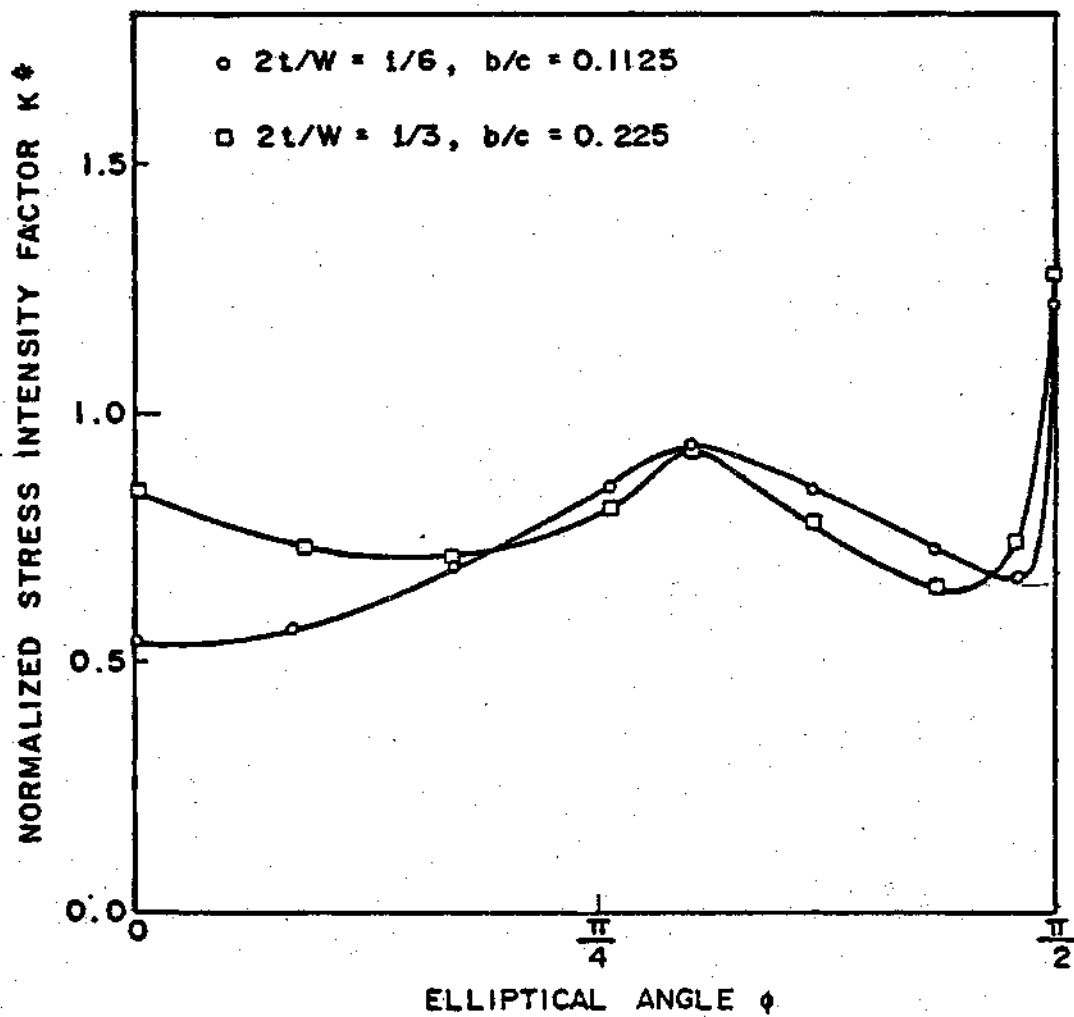(c/L = 1/3, 2t/W = 1/3, b/t = 9/10, b/c = 0.225)

Figure 19. Influence of the Specimen Thickness on the
Variation of the Normalized Stress Intensity
Factor Along the Quarter-Elliptical Crack
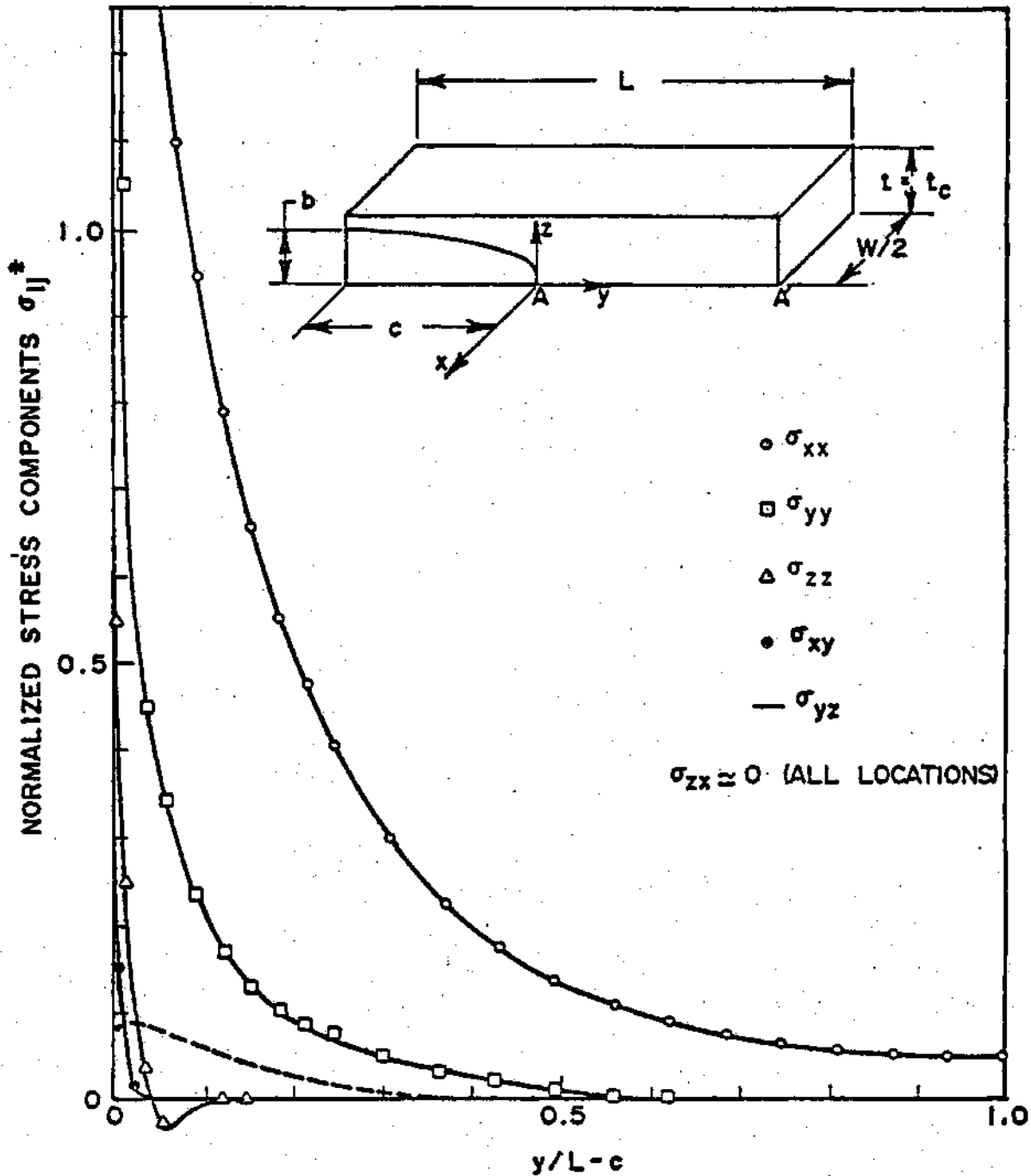Front ($\varepsilon = 0$, $c/L = 1/3$, $b/t = 9/10$)

Figure 20. Variation of Normalized Stress Components Along the Lower Line of Symmetry (A-A) from Crack Tip to the End of Specimen ($\varepsilon = 0$, $c/L = 1/3$, $2t/W = 1/3$, $b/t = 9/10$, $b/c = 0.225$)
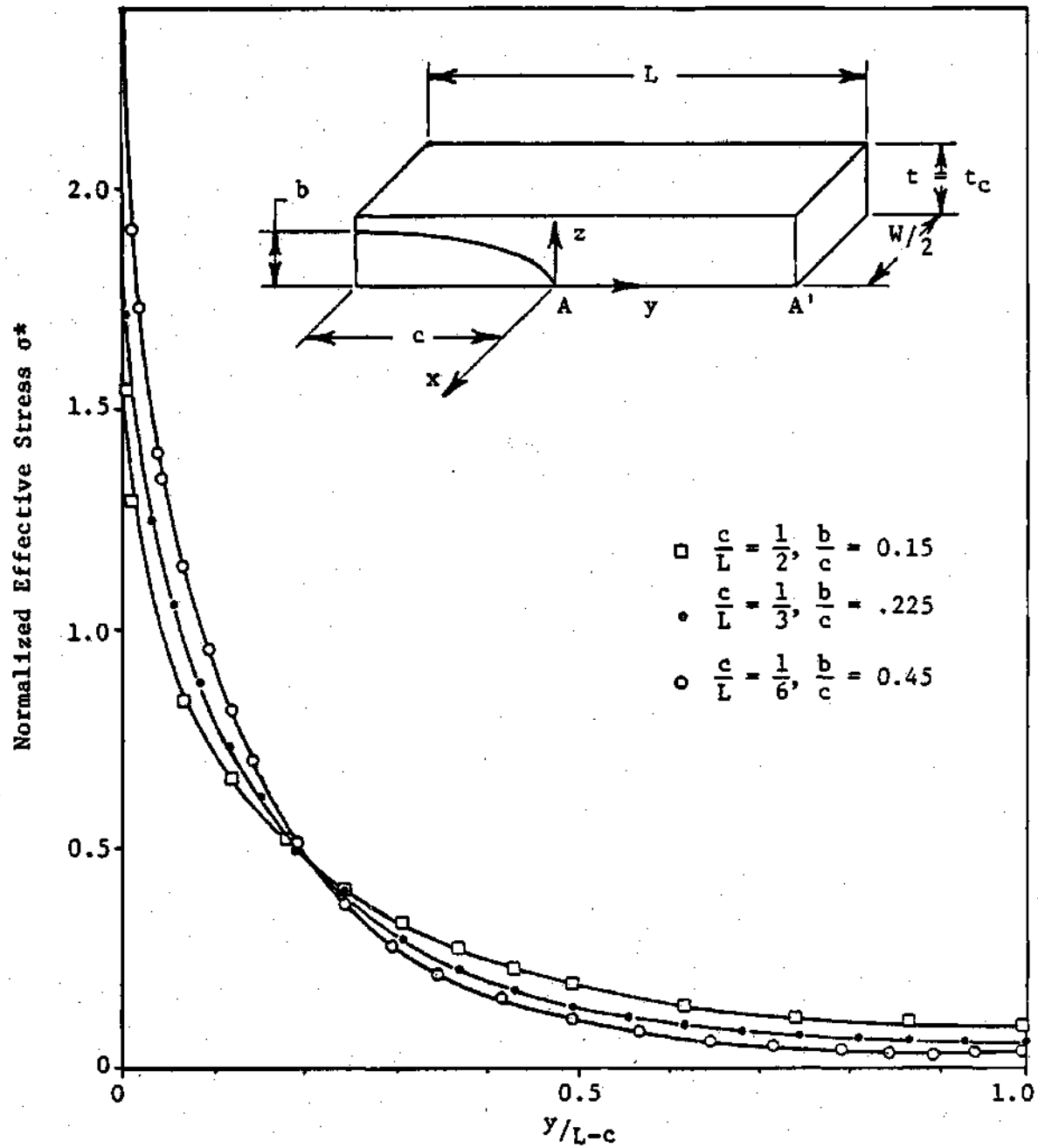
Figure 21. Variation of the Normalized Effective
Stress Along the Lower Line of Symmetry (A-A')
from Crack Tip to the End of Specimens
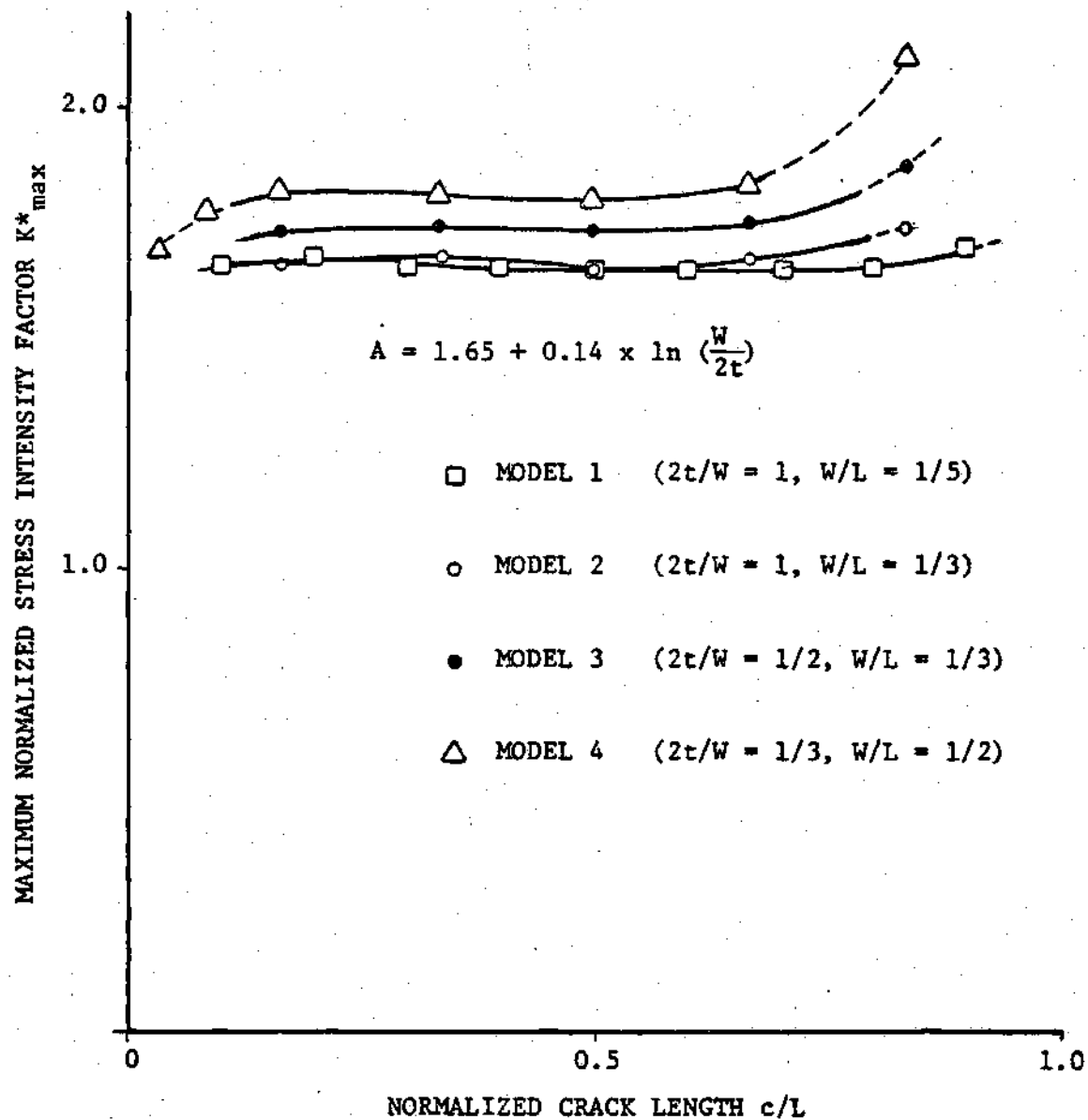($\varepsilon=0$, $2t/_W=1/3$, $b/_t=9/10$)

Figure 22. Maximum Normalized Stress Intensity Factor for
Four Different Sizes of Idealized Double Torsion Models ($\varepsilon=0$)

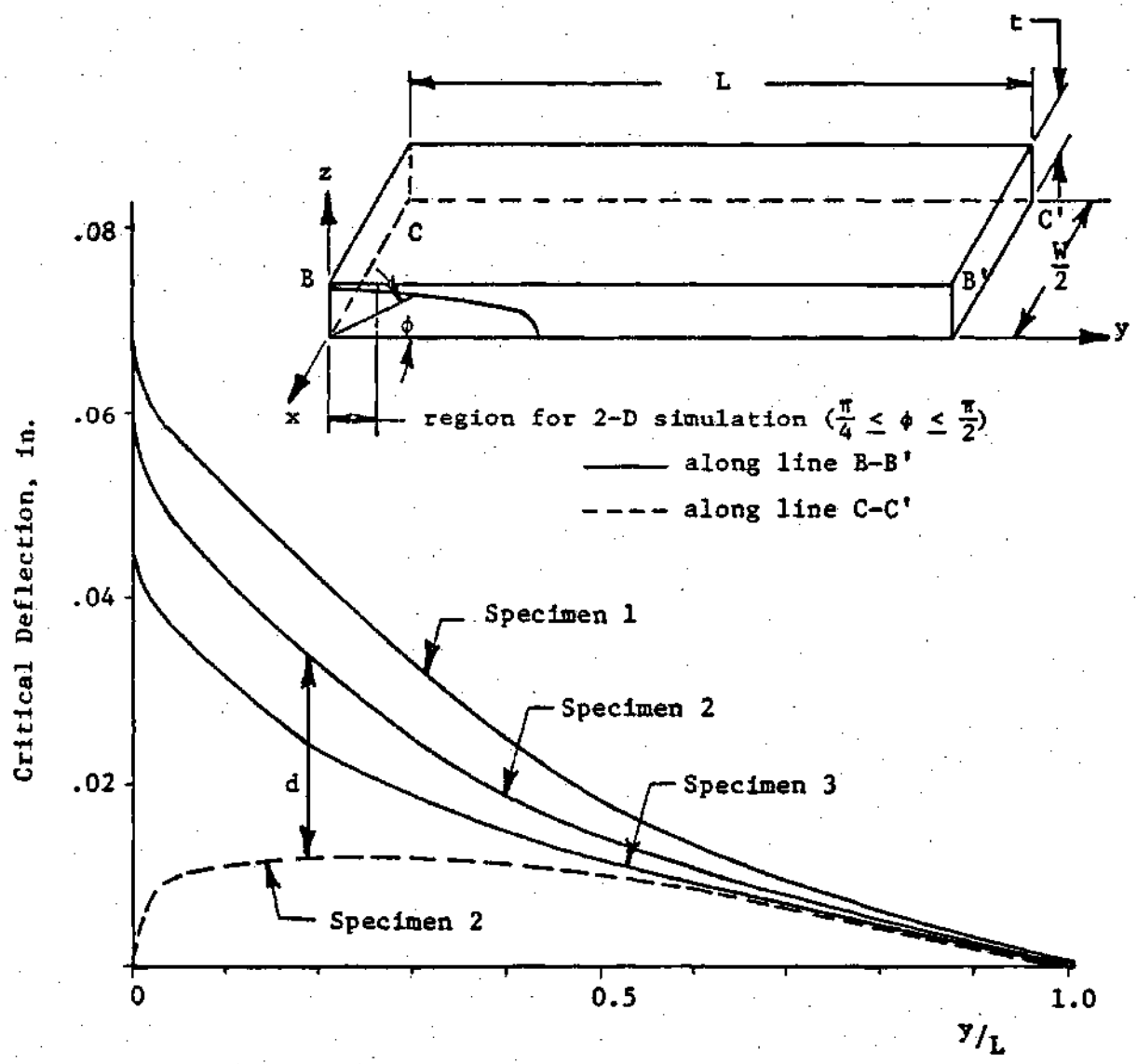Figure 23. The Critical Deflections Along the Upper Symmetric Line (B-B') and the Outer Edge Locations (C-C') ($W=W_m=3"$, $\frac{2t}{W} = \frac{1}{3}$)

d = 0.011"

d = 0.022"

d

path 1
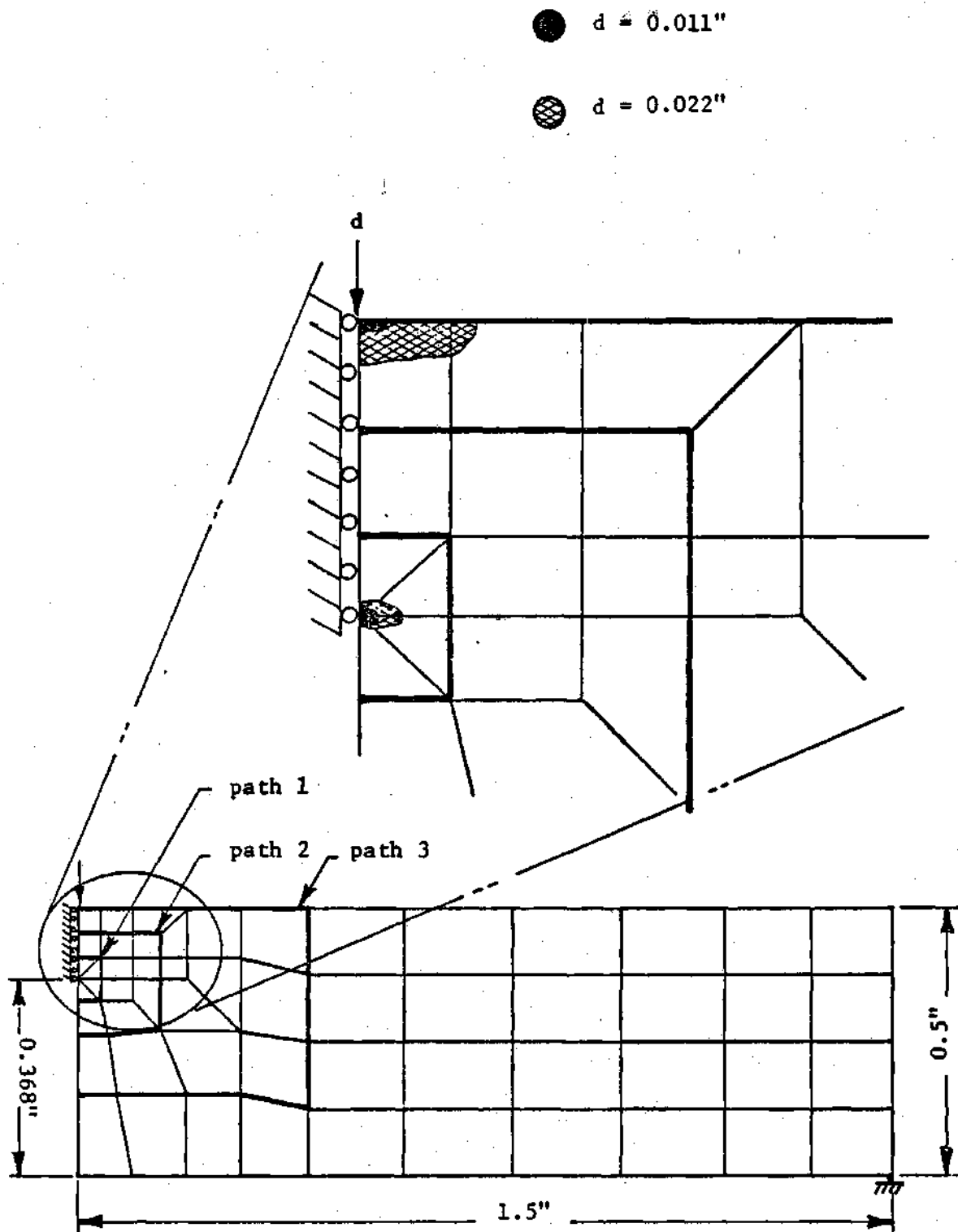
path 2   path 3

0.368"

0.5"

1.5"

Figure 24. Plastic Zones for the Equivalent Plane Strain
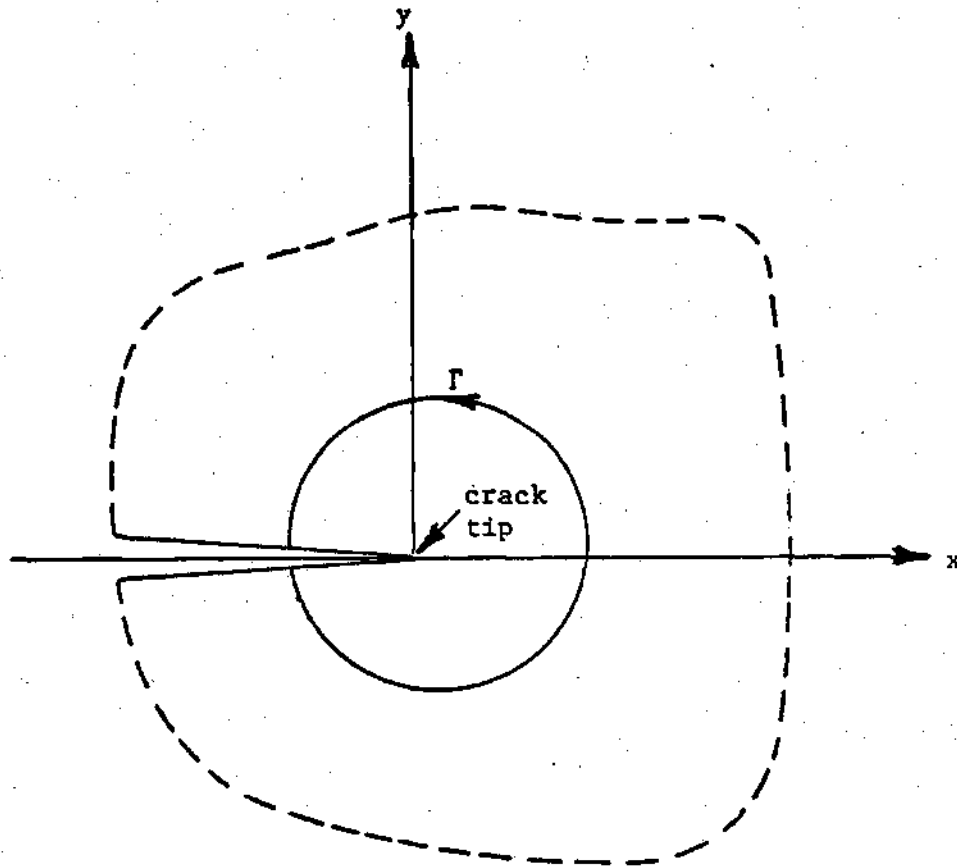Analysis of Double Torsion Specimen at Two Load Levels

Figure 25. A 2-D Cracked Body and a Contour for J-Integral

BIBLIOGRAPHY

1. Outwater, J. O., and Gerry, D. T., "On the Fracture Energy of Glass", U. S. Naval Research Lab. Report Contract NONR 3219(01) (XO), 1966, AD640848 - Dept. of Mech. Eng., Univ. of Vermont.

2. Nadeau, J. S., "Subcritical Crack Growth in Vitreous Carbon at Room Temperature", J. of the American Ceramic Society, Vol. 57, 1974, pp. 303-306.

3. Evans, A. G., "A Simple Method for Evaluating Slow Crack Growth in Brittle Materials", Int. J. of Fracture, Vol. 9, 1973, pp. 267-275.

4. Knauss, W. G., "Fracture of Solids Processing Deformation Rate Sensitive Material Properties", in The Mechanics of Fracture, ed. by F. Erdogan, The American Society of Mechanical Engineers, 1976, pp. 69-103.

5. Murphy, M. C., "Principles of Fracture Mechanics Applied to the Failure Modes of Fiber Reinforced Composition and to the Fatigue of Selected Brittle Resins and Glass", Ph.D. Thesis, Univ. of Vermont, 1972.

6. Outwater, J. O. and Carnes, W. O., "Fracture Mechanics of Composite Materials", Proceeding, U. S. Army, Solid Mechanics Symposium, 1968, Watervliet, Arsenal, Watervliet, N.Y.

7. Murray, M. T. and Robinson, P. M., "The Fracture Toughness Testing of Light Weight Zinc Diecastings", Soc. of Diecast. Eng., 9th International Congress, Milwaukee, 1977, Preprint.

8. Murphy, M. C., Kumble, R. G., Berry, J. T., and Outwater, J. O., "Fracture Toughness Determination in Cast Metals", American Foundrymen's Society Trans., Vol. 81, 1973, pp. 158-162.

9. Kumble, R. G., "Evaluation of Anisotropy and Plane Strain Properties of Cast and Wrought Materials", Ph.D. Thesis, Univ. of Vermont, Vermont, 1973.

10. Outwater, J. O., Murphy, M. C., Kumble, R. G., and Berry, J. T., "Double Torsion Technique as a Universal Fracture Toughness Test Method", in Fracture Toughness and Slow-Stable Cracking, ASTM STP 559, American Society for Testing and Materials, 1974, pp. 127-138.

11. Beachem, C. D., Kies, J. A., and Brown, B. F., "A Constant K Specimen for Stress Corrosion Cracking Tests", *Materials Research and Standards*, Vol. 11, No. 4, 1971, pp. 30.

12. William, D. P. and Evans, A. G., "A Simple Method for Studying Slow Crack Growth", *J. of Testing and Evaluation*, Vol. 1, No. 4, Aug. 1973, pp. 264-270.

13. Ten Haagen, C. W., "Advancement of the Double Torsion Fracture Toughness Test", M. S. Thesis, Univ. of Vermont, Vermont, 1976.

14. Ten Haagen, C. W., and Berry, J. T., "The Application of the Double Torsion Test to the Determination of Fracture Toughness of Gray and Ductile Iron", *American Foundrymen's Society Trans.*, Vol. 84, 1976, pp. 535-542.

15. Ten Haagen, C. W. and Berry, J. T., "Charting the Fracture Toughness Characteristics of Castings Using the Double Torsion Method", in *Fracture 1977*, Proceedings of Fourth International Conference on Fracture, Vol. III, 1977, pp. 565-572.

16. Murray, M. J., Murray, M. T., and Sare, I. R., "Fracture Toughness Testing of Metallic Materials", *J. of Australasian Institute of Metals*, Vol. 22, No. 2, June 1977, pp. 126-131.

17. Murray, M. J., "Fracture of WC-Co Alloys: An Example of Spatially Constrained Crack Tip Opening Displacement", *Proc. Royal Society*, London A 356, 1977, pp. 483-508.

18. Evans, A. G., "Thermal Fracture in Ceramic Materials", *Proc. Br. Ceram. Soc.*, No. 25, 1975, pp. 217-237.

19. Bruce, J. G., and Koepke, B. G., "Evaluation of K_{IC} by the Double-Torsion Technique", *J. of the American Ceramic Society*, Vol. 60, 1977, pp. 284-285.

20. Evans, A. G., "Fracture Mechanics Determinations", in *Fracture Mechanics of Ceramics*, Vol. 1, ed. by R. C. Bradt et al., Plenum, 1974, pp. 17-48.

21. Wachtman, J. B., Jr., "Highlights of Progress in the Science of Fracture of Ceramics and Glass", *J. of the American Ceramic Society*, Vol. 57, 1974, pp. 509-519.

22. Lenoe, E. M., and Neal, D. M., "Assessment of Strength-Probability-Time Relationship in Ceramics", in *Cracks and Fracture*, ASTM STP 601, American Society for Testing and Materials, 1976, pp. 63-85.

23. Lawn, B. R., and Wilshaw, T. R., Fracture of Brittle Solids, Cambridge University Press, London, 1975.

24. Tracey, D. M., "Finite Elements for Three-Dimensional Elastic Crack Analysis", Nuclear Engineering and Design, Vol. 26, 1974, pp. 282-290.

25. Barsoum, R. S., "On the Use of Isoparametric Finite Elements in Linear Fracture Mechanics", Int. J. for Numerical Method in Engineering, Vol. 10, 1976, pp. 25-37.

26. Freese, C. E. and Tracey, D. M., "The Natural Isoparametric Triangle Versus Collapsed Quadrilateral for Elastic Crack Analysis", Int. J. of Fracture, Vol. 12, 1976, pp. 767-770.

27. Henshell, R. D. and Shaw, K. G., "Crack Tip Finite Elements are Unnecessary", Int. J. for Numerical Methods in Engineering, Vol. 9, 1975, pp. 495-507.

28. Barsoum, R. S., "Triangular Quarter-Point Elements as Elastic and Perfectly-Plastic Crack Tip Elements", Int. J. for Numerical Methods in Engineering, Vol. 11, 1977, pp. 85-98.

29. Chan, S.-K., Fan, Y., Filstrup, A. W., and Gabrielse, S. E., "Verifying the Plastic Capabilities of a General Purpose Computer Code", in Pressure Vessels and Piping Computer Program Evaluation and Qualification, ed. by D. E. Dietrich, PVP-PB-024, The American Society of Mechanical Engineers, New York, 1977, pp. 51-66.

30. Trantina, G. G., "Stress Analysis of the Double-Torsion Specimen", J. of the American Ceramic Society, Vol. 60, Jul-Aug., 1977, pp. 338-341.

31. Griffith, A. A., "The Phenomena of Rupture and Flows in Solids", Phil. Trans. Roy. Soc., London, Ser.A 221, 1920, pp. 163-198.

32. Griffith, A. A., "Theory of Rupture", Proceedings of First International Congress for Applied Mechanics, Delft, 1924, pp. 55-63.

33. Irwin, G. R., "Analysis of Stresses and Strains Near the End of a Crack Traversing a Plate", Trans. ASME, J. of Applied Mechanics, Vol. 24, 1957, pp. 361-364.

34. Westergaard, H. M., "Bearing Pressures and Crack", Trans. ASME, J. of Applied Mechanics, Vol. 6, 1939, pp. A49-53.

35. Sih, G. C., Handbook of Stress Intensity Factors, Lehigh Univ. Pub., Bethlehem, Penn., 1973.

36. Sih, G. C. and Liebowitz, H., "Mathematical Theories of Brittle Fracture", in Fracture, Vol. II, ed. by H. Liebowitz, Academic, New York, 1968, pp. 67-190.

37. Kassir, M. K. and Sih, G. C., "Three-Dimensional Stress Distribution Around an Elliptical Crack Under Arbitrary Loadings", Trans. ASME, J. of Applied Mechanics, Vol. 33, 1966, pp. 601-611.

38. Gross, B. and Srawley, J. E., "Stress Intensity Factors for Three Point Bend Specimens by Boundary Collocation", NASA Tech., Note D-3092, 1965.

39. Srawley, J. E., and Gross, B., "Stress Intensity Factors for Crackline-Loaded Edge-Crack Specimens", NASA Report, TN D-3820, 1967.

40. Bowie, O. L., "Analysis of an Infinite Plate Containing Radial Crack Originating from the Boundary of an Internal Circular Hole", J. Math. Phys., Vol. 35, 1956, pp. 60-71.

41. Bowie, O. L., and Neal, D. M., "A Modified Mapping-Collocation Technique for Accurate Calculation of Stress Intensity Factors", Int. J. Fracture Mech., Vol. 6, 1970, pp. 199-206.

42. Cruse, T. A., and Buren Van, W., "Three-Dimensional Elastic Stress Analysis of a Fracture Specimen with an Edge Crack", Int. J. Fracture Mech., Vol. 7, 1970, pp. 1-17.

43. Cruse, T. A., "Numerical Evaluation of Elastic Stress Intensity Factors by the Boundary-Integral Equation Method", in The Surface Crack: Physical Problems and Computational Solutions, Swedlow, J. L., ed., ASME, New York, 1972, pp. 153-170.

44. Rice, J. R. and Tracey, D. M., "Computational Fracture Mechanics", in Numerical Computer Methods in Structural Mechanics, S. J. Fenves et. al. ed., Academic, New York, 1973, pp. 585-623.

45. Gallagher, R. H., "Survey and Evaluation of the Finite Element Method in Fracture Mechanics Analysis", Proc. of First Intl. Conf. on Struc. Mech. in Reactor Tech., Vol. 6, Part I, Berlin, 1971, pp. 637-653.

46. Hilton, P. D., and Sih, G. C., "Application of Finite Element Method to Calculation of Stress Intensity Factors", in Methods of Analysis and Solutions of Crack Problems, ed. by G. C. Sih, Walters-Noordhoff, The Netherlands, 1972, pp. 426-483.

47. Pian, T. H. H., "Crack Elements", Proc. of World Congress on Finite Element Methods in Structural Mechanics, Vol. 1, Bournemouth, England, 1975, pp. F.1-39.

48. Kathiresan, K., "Three-Dimensional Elastic Fracture Analysis by a Displacement Hybrid Finite Element Model", Ph.D. Thesis, Georgia Institute of Technology, 1976.

49. Wilson, W. K., "On Combined Mode Fracture Mechanics", Ph.D. Dissertation, University of Pittsburgh, 1969.

50. Hilton, P. D. and Hutchinson, J. W., "Plastic Intensity Factors for Cracked Plates", Eng. Frac. Mech., Vol. 3, 1971, pp. 435-451.

51. Wilson, W. K., "Finite Element Method for Elastic Bodies", in Methods of Analysis and Solutions of Crack Problems, ed. by G. C. Sih, Noordhoff, Holland, 1973, pp. 485-515.

52. Byskov, E., "The Calculation of Stress Intensity Factors Using the Finite Element Method with Cracked Elements", Int. J. Fract. Mech., Vol. 6, 1970, pp. 159-167.

53. Tracey, D. M., "Finite Elements for Determination of Crack Tip Elastic Stress Intensity Factors", Eng. Fracture Mechanics, Vol. 3, 1971, pp. 255-265.

54. Raju, I. S. and Newman, J. C., Jr., "Three-Dimensional Finite-Element Analysis of Finite-Thickness Specimens," NASA TN D-8414, 1977.

55. Blackburn, W. S., and Hellen, T. K., "Calculation of Stress Intensity Factors in Three Dimensions by Finite Element Methods", Int. J. for Num. Meth. in Eng., Vol. 11, 1977, pp. 211-219.

56. Pian, T. H. H., Tong, P., and Luk, C. H., "Elastic Crack Analysis by a Finite Element Method", Proc. of the 3rd Intl. Conf. on Matrix Method in Structural Mechanics, Wright-Patterson AFB, Oct. 1971.

57. Atluri, S. N., Kobayashi, A. S., and Nakagaki, M., "An Assumed Displacement Hybrid Finite Element Model for Linear Fracture Mechanics", Int. J. of Fracture, Vol. 11, 1975, pp. 257-271.

58. Atluri, S. N., Nakagaki, M., and Chen, W. H., "Fracture Analysis Under Large-Scale Plastic Yielding: A Finite Deformation, Embedded Singularity, Elasto-Plastic Incremental Finite Element Solution", in Flaw Growth and Fracture, ASTM STP 631, American Society for Testing and Materials, Aug. 1976, pp. 42-61.

59. Rhee, H. C., Atluri, S. N., Moriya, K., and Pian, T. H. H., "Hybrid Finite Element Procedures for Analyzing Through Flaws in Plates in Bending", Trans. of 4th Int. Conf. on Struc. Mech. in Reactor Tech., Vol. M, San Francisco, Aug. 1977, pp. M2/4.

60. Atluri, S. N., and Kathiresan, K., "On a 3-D 'Singularity Element' for Computation of Combined-Mode-Stress-Intensities", Proceeding of 13th SES Meeting, NASA Special Tech. Pub., 1976, pp. 257-264.

61. Kobayashi, A. S., Maiden, D. E., and Simon, B. J., "Application of the Method of Finite Element Analysis to Two-Dimensional Problems in Fracture Mechanics", ASME Paper No. 69-WA/PVP-12, 1969.

62. Chan, S. K., Tuba, I. S., and Wilson, W. K., "On the Finite Element Method in Linear Fracture Mechanics", Eng. Frac. Mech., Vol. 2, 1970, pp. 1-17.

63. Dixon, J. R., and L. P. Pook, "Stress Intensity Factors Calculated Generally by the Finite Element Technique", Nature, 224, 1969, pp. 166-167.

64. Parks, D. H., "A Stiffness Derivative Finite Element Technique for Determination of Elastic Crack Tip Stress Intensity Factors", Brown University Eng. Div. Tech. Rept. NASA NGL 40-002-080/13, May 1973.

65. Hellen, T. K., "On the Method of Virtual Crack Extension", Int. J. of Num. Meth. in Eng., 9, 1975, pp. 181-207.

66. Rice, J. R., "A Path Independent Integral and the Approximate Analysis of Strain Concentration by Notches and Crack", J. Appl. Mech., Vol. 35, 1968, pp. 379-386.

67. Virkar, A. V., and Gordon, R. S., "Crack Front Profiles in Double Torsion Specimens", J. of the American Ceramic Society, Vol. 58, 1975, pp. 536-537.

68. Sih, G. C., "Elastic-Plastic Fracture Mechanics" in Proceedings of an International Conference on Propsects of Fracture Mechanics, ed. by G. C. Sih et al. 1974, Noordhoff, pp. 613-621.

69. Hertzberg, R. W., Deformation and Fracture Mechanics of Engineering Materials, John Wiley & Sons, New York, 1976, pp. 279-282.

70. "Standard Method of Test for Plane-Strain Fracture Toughness of Metallic Materials", E399-74, ASTM Standards, American Society for Testing and Materials, Philadelphia, July, 1974.

71. Brown, W. F., Jr., and Srawley, J. E., Plane Strain Crack Toughness Testing of High Strength Metallic Materials, ASTM STP 410, American Society for Testing and Materials, 1966.

72. Broek, D., Elementary Engineering Fracture Mechanics, Noordhoff, Leyden, The Netherlands, 1974.

73. Shih, C. F., DeLorenzi, H. G., and Andrews, W. R., "Elastic Compliances and Stress Intensity Factors for Side-Grooved Compact Specimens", Int. J. of Fracture, Vol. 13, 1977, pp. 544-548.

74. Andrews, W. R., and Shih, C. F., "Thickness and Side-Groove Effects in Compact Specimens of A533-B Steel at 93 Deg C", presented at the ASTM Symposium on Elastic-Plastic Fracture, Atlanta, Ga., Nov. 1977.

75. Mostovoy, S., Crosley, P. B., and Ripling, E. J., "Use of Crack-Line-Loaded Specimens for Measuring Plane-Strain Fracture Toughness", J. of Materials, Vol. 2, 1967, pp. 661-681.

76. Prado, M. E., "Evaluation of Fracture Toughness of Beryllium", Report UCID-15970, Lawrence Livermore Lab., Livermore, Cal., 1970.

77. Gallagher, J. P., "Experimentally Determined Stress Intensity Factors for Several Contoured Double Cantilever Beam Specimens", Eng. Fracture Mech., Vol. 3, 1971, pp. 27-43.

78. Sih, G. C., "Some Basic Problems in Fracture Mechanics and New Concepts", Eng. Fracture Mech., Vol. 5, 1973, pp. 365-377.

79. Tseng, A. A., "Fracture Mechanics Assessment of NDE Rejection Criteria for the Tube-to-Tubesheet Weld", Report No. WTD-DVE-78-026, June 1978, Westinghouse Electric Corporation, Tampa, Florida.

80. Zienkiewciz, O. C., The Finite Element Method in Engineering Science, 2nd ed., McGraw-Hill, New York, 1971.

81. Mondkar, D. P., and Powell, G. H., "Large Capacity Equation Solver for Structural Analysis", Computers and Structures, Vol. 4, 1974, pp. 669-728.

82. Gallagher, R. H., Finite Element Analysis: Fundamentals, Prentice-Hall, New Jersey, 1975.

83. Taig, I. C., "Structural Analysis by the Matrix Displacement Method", Engl. Electric Aviation, Report No. S017, 1961.

84. Irons, B. M., "Engineering Application of Numerical Integration in Stiffness Method", *J. of American Institute of Aeronautics and Astronauts*, Vol. 14, 1966, pp. 2035-2037.

85. Ayres, D. J., "A Numerical Procedure for Calculating Stress and Deformation Near a Slit in a Three-Dimensional Elastic-Plastic Solid", *Eng. Fract. Mech.*, Vol. 12, 1970, pp. 87-106.

86. Sih, G. C., Hilton, P. D., Hartranft, R. J., and Kiefer, B. V., "Three-Dimensional Stress Analysis of a Finite Slab Containing a Transverse Center Crack", Tech. Report No. N0014-67-A-0370-0012, Office of Naval Research, Arlington, Virginia, 1975.

87. Folias, E. S., "On the Three-Dimensional Theory of Cracked Plates", Trans. ASME, *J. Appl. Mech.*, Vol. 42, Sept. 1975, pp. 663-674.

88. Benthem, J. P., and Koiter, W. T., "Discussion on the Three-Dimensional Theory of Cracked Plates", Trans. ASME *J. Appl. Mech.*, Vol. 43, June 1976, pp. 374-375.

89. Burck, L. H., "Fatigue Growth of Surface Cracks in Bending", *Engineering Fracture Mechanics*, Vol. 9, 1977, pp. 389-395.

90. Swedlow, J. L., ed., *The Surface Crack: Physical Problems and Computation Solutions*, American Society of Mechanical Engineers, New York, 1972.

91. Sih, G. C., and Hartranft, R. J., "Growth Characteristics of Surface Flaw in Pressure Vessels", *Trans. of 3rd Int. Conf. on Struc. Mech. in Reactor Tech.*, Vol. 3, London, Sept. 1975, pp. G4/2.

92. Timoshenko, S. P., and Goodier, J. N., *Theory of Elasticity*, 3rd ed., McGraw-Hill, New York, 1970.

93. Tong, P. and Pian, T. H. H., "On the Convergence of the Finite Element Method for Problems with Singularity", *Int. J. Solids Structures*, Vol. 9, 1972, pp. 313-321.

94. Seely, F. B. and Smith, J. O., *Advanced Mechanics of Materials*, John Wiley & Sons, New York, 1952.

95. Rice, J. R., and Rosengren, G. F., "Plane Strain Deformation Near a Crack Tip in a Power-Law Hardening Material", *J. Mech. Phys. Solids*, Vol. 16, 1968, pp. 1-12.

96. Hutchinson, J. W., "Singular Behavior at the End of a Tensile Crack in a Hardening Material", J. Mech. Phys. Solids, Vol. 16, 1968, pp. 13-31.

97. Begley, J. A., and Landes, J. D., "The J Integral as a Fracture Criterion", in Fracture Toughness, Part II, ASTM STP 514, American Society for Testing and Materials, 1972, pp. 1-20.

98. Mendelson, A., Plasticity: Theory and Application, MacMillan, New York, 1968.

99. Larsson, S. G., and Carlsson, A. J., "Influence of Non-Singular Stress Terms and Specimen Geometry on Small-Scale Yielding at Crack Tips in Elastic-Plastic Materials", J. Mech. Phys. Solids, Vol. 21, 1973, pp. 263-277.

100. Tseng, A. A., Ten Haagen, C., and Berry, J. T., "A Numerical Analysis of the Double Torsion Test and Its Relation to the Evaluation of Tool Steel", in Sixth North American Metalworking Research Conference Proceedings, Society of Manufacturing Engineers, April 1978, pp. 258-263.

101. Boresi, A. P., Elasticity in Engineering Mechanics, 1st ed., Prentice-Hall, Englewood Cliffs, New Jersey, 1965, pp. 133-143.

102. Sih, G. C., "A Review of the Three-Dimensional Problem for a Cracked Plate", Int. J. Fracture Mech., Vol. 7, 1971, pp. 39-61.

103. Srawley, J. E., "Plane Strain Fracture Toughness", Fracture, Vol. IV, ed. by H. Liebowitz, Academic, 1969, pp. 45-68.

104. Wilson, W. K., and Begley, J. A., "Variable Thickness Study of the Edge Cracked Bend Specimen", HSST Technical Report No. 25 USAEC, Oak Ridge National Laboratory, 1973.

105. Hayes, D. J., and Turner, C. E., "An Application of Finite Element Techniques to Post-Yield Analysis of Proposed Standard Three-Point Bend Fracture Test Pieces", Int. J. of Fracture, Vol. 10, No. 1, 1974, pp. 17-32.

106. Wilson, W. K., Chan, S. K., and Swamy, S., "Finite Element Computer Programs for Calculating the J-Line Integral", Research Report 75-1E7-FMPWR-R1, March, 1975, Westinghouse Research Laboratories, Pittsburgh, Pennsylvania.

107. Yamada, Y., Yoshimura, N., and Sakurai, "Plastic Stress-Strain Matrix and its Application for the Solution of Elastic-Plastic Problem by Finite Element Method", Int. J. Mech. Sci., Vol. 10, 1968, pp. 543-354.

VITA

Ampere A. Tseng was born in Kiangsi, China on January 21, 1946. He graduated from the Department of Mechanical Engineering, Taipei Institute of Technology, Taiwan, in July, 1966. He began his graduate study at the Tennessee Technological University in September, 1971 and obtained the degree of Master of Science in June, 1973. In August, 1974, he received a second master degree in Theoretical and Applied Mechanics from the University of Illinois at Champaign - Urbana. He joined the Georgia Institute of Technology as a doctoral student in September, 1974. In April, 1977, he became a part-time student and took up an appointment at Westinghouse Electric Corporation, Tampa Division as an engineer in the Breeder Reactor Development Program.